STUDY OF RUTHENIUM AND RUTHENIUM OXIDE'S ELECTROCHEMICAL PROPERTIES AND APPLICATION AS A COPPER DIFFUSION BARRIER

Yibin Zhang, B.Sc. (Honours), M.Sc.

Dissertation Prepared for the Degree of

DOCTOR OF PHILOSOPHY

UNIVERSITY OF NORTH TEXAS

August 2005

APPROVED:

Oliver M. R. Chyan, Major Professor
Michael G. Richmond, Committee Member
Teresa D. Golden, Committee Member
Angela Wilson, Committee Member
Ruthanne D. Thomas, Chair of the Department of Chemistry
Sandra L. Terrell, Dean of the Robert B. Toulouse School of Graduate Studies

Zhang, Yibin. *Study of Ruthenium and Ruthenium Oxide's Electrochemical Properties and Application as a Copper Diffusion Barrier.* Doctor of Philosophy (Analytical Chemistry), August 2005, 155 pp., 6 tables, 57 figures, references, 138 titles.

As a very promising material of copper diffusion barrier for next generation microelectronics, Ru has already obtained a considerable attention recently. In this dissertation, we investigated ruthenium and ruthenium oxide electrochemical properties and the application as a copper diffusion barrier.

Cu UPD on the RuO_x formed electrochemically was first observed. Strong binding interaction, manifesting by the observed Cu UPD process, exists between Cu and Ru as well as its conductive ruthenium oxide. Since UPD can be conformally formed on the electrode surface, which enable Ru and RuO_x has a potential application in the next generation anode. The [Cl^-] and pH dependent experiment were conducted, both of them will affect UPD Cu on Ru oxide. We also found the Cu deposition is thermodynamically favored on RuO_x formed electrochemically.

We have studied the Ru thin film (5nm) as a copper diffusion barrier. It can successfully block Cu diffusion annealed at 300^{o}C for 10min under vacuum, and fail at 450 ^{o}C. We think the silicidation process at the interface between Ru and Si. PVD Cu/Ru/Si and ECP Cu/Ru/Si were compared each other during cupper diffusion study. It was observed that ECP Cu is easy to diffuse through Ru barrier. The function of RuO_x in diffusion study on Cu/Ru/Si stack was discussed.

In pH 5 Cu^{2+} solution, Ru and Pt electrochemical behavior were investigated. A sharp difference was observed compared to low pH value. The mechanism in pH 5 Cu^{2+} solution was interpreted. An interesting compound (posnjakite) was obtained during the electrochemical process. An appropriate formation mechanism was proposed. Also Cu_2O was formed in the process. We found oxygen reduction reaction is a key factor to cause this phenomenon.

ACKNOWLEDGEMENTS

First, I gratefully render my thanks to my research advisor Dr. Oliver Chyan for his support, encouragement and guidance during the course of research. I appreciate Dr. Golden (my committee member) for her to help me collect and analyze XRD data. I would express my sincerely appreciation to my other committee members, Dr. Michael G. Richmond and Dr. Angela Wilson for their comments and critiques, which greatly helped me to finish this dissertation with better shape. I would also like to thank Dr. EL.Bouananni for giving access to XPS, RBS and PVD facility in his Laboratory for Electronic materials and devices. The financial support from the Welch Foundation, UNT Faculty Research Fund, Kodak, Texas Instrument and Texas Advanced Technology program in deeply appreciated.

I would thank Dr. Swarnagowri Addepalli for training XPS operation. Specially, I would gratefully give thanks to my two colleagues, Dr. Tiruchirapalli Natarajan Arunnagiri and Dr. Raymond Chan. They gave me a lot of help in finishing this dissertation. Also I would like to acknowledge my other colleague, Long Huang, Oscar Ojeda, Sarah Flores and Praveen Reddy Nalla for their help. I am glad to express thanks to Ann F. Hudgens, Mickey Richardson and Joshua Hudson for correction of my dissertation.

I wish to express my deepest thanks to my parents and parents-in-law for their long time support and love. At last, most importantly, I would thank my

wife Tianyu Feng for her love, and constant enthusiasm and confidence in my decision.

TABLE OF CONTENTS

LIST OF TABLES

LIST OF FIGURES

CHAPTER 1

INTRODUCTION

Since Jack Kilby made the first integrated circuit (IC) chip in Texas Instrument in 1958,[1] the integrated circuit concept has been developed as a commercial product. Almost 50 years has passed. Based on Moore's law, the size of chips continually shrinks down by about 30% annually. To satisfy the increasing performance and packing density required in microelectronic devices, copper (Cu) has been used as an interconnection metal to enhance operating speed and reliability since 1997,[2] and now most high-performance logic manufacturers are developing, piloting or producing Cu-based circuits. [3,4] Cu can easily drift into the ILD (interlayer deposition) and react with it.[3,5] This diffused Cu seriously debases the performance of device. Therefore, a Cu diffusion barrier is necessary for the use of Cu as the interconnect metal in semiconductor devices. Currently, IC industry is using Ta/TaN as the Cu diffusion barrier. As the devices continue scaling down, it demands that the thickness of a diffusion barrier should be reduced to 5nm for 45 nm half-pitch process.[6] To produce a 5nm Ta/TaN Cu diffusion barrier, there is an unsolvable difficulty to overcome. It cannot be scaled down to 5nm. Also, because the adhesion between Cu and Ta is not good and Ta is easily oxidized in atmosphere, it is impossible to use the attractive Cu deposition method, electrochemical deposition, to plate Cu directly on the diffusion barrier. Usually, a Cu seed layer is deposited on Ta/TaN, which makes the producing process more complex. The industry is now looking for a new Cu

diffusion barrier for the next generation microelectronics. Ruthenium (Ru) is a very promising material due to its excellent inherent properties, such as high thermal and chemical stability, high thermal and electrical conductivity and high melting point. Industry has already shifted their interests in ruthenium. [7] Little was studied for Ru in IC industry application. To let it to be a reality, much research needs to been done. This dissertation will touch on some areas about Ru that are seldom studied.

The objective of this introductory chapter will be to provide the reader with a broad foundation of understanding for experimental techniques and procedures while also providing a general review on the research undertaken. The dissertation may be broadly divided into two main interesting covering: 1) Electrochemical properties of ruthenium and ruthenium oxide. 2) The behavior of ultra-thin Ru films as Cu diffusion barrier. The first area will be covered by chapter 2 and chapter 4, which focus on the fundamental research to gain more understanding of Ru and RuO_x behavior in Cu^{2+} solution. Chapter 3 will cover the second topic- application of Ru as Cu diffusion barrier. Chapter 5 will summarize and give perspective of the research from chapter 2, 3 and 4. Also some future work will be discussed in chapter 5.

1.1 Ruthenium and RuO_2

1.1.1 Structure

Ruthenium is a transition metal discovered by Karl Karlovich Klaus in 1844, which has hexagonal crystal structure (as show Figure 1.1). Lattice constant: a (0.27056 nm) and c (0.42816 nm). RuO_2 is the only stable oxide of Ru with a rutile-type structure.

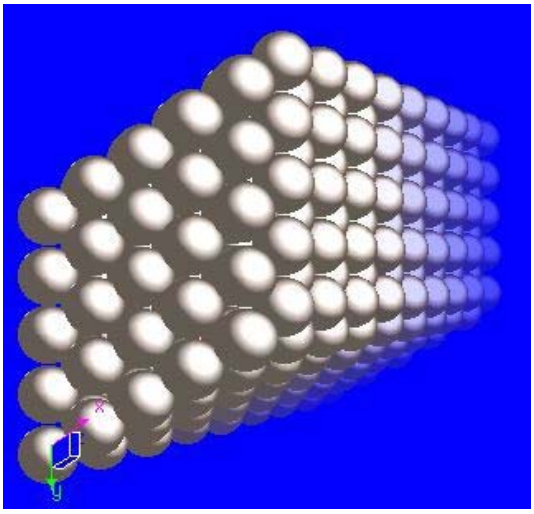

Figure 1.1: Crystal structure of ruthenium.

1.1.2 Properties

Ruthenium is the least expensive member of the platinum group of the metals, with a work function of 4.8eV by Schottky barrier measurements,[8] melting point of 2523 K and a very high resistance to chemical attack. Ruthenium is stable in atmosphere, and will not be oxidized by O_2 in air, but readily reacts on heating to give RuO_2. It is even insoluble in *aqua regia*. However, explosive oxidation will occur if potassium perchlorate is added in the acid. [9]

Table 1.1 lists some physical properties of Ru, which has high melting point and low resistivity (6.8 $\mu\Omega$. cm at 0 ^{o}C). Ruthenium is also attractive since its oxide is an intrinsic conductor. RuO_2 exhibits a metallic conductivity (35 $\mu\Omega$. cm at RT) arising from the partially filled Ru 4d states.[10]

Table 1.1: Physical properties of ruthenium.

	Crystal structure	Density /kg.m^{-3} 20 ^{o}C	Thermal conductivity (0-100 ^{o}C)	Hardness (annealed)	Work function	Metallic radius
Ru	hcp	12450	105 w.m^{-1}k^{-1}	200-350 Hv	>4.71 eV	0.134 nm

1.1.3 Application of Ruthenium and Ruthenium Oxide

Ruthenium is a transition metal, and its complex compounds have received attention in organic chemistry as catalysts in synthesis. Due to its high chemical resistivity, Ru is applied in the chloro-alkali industry as electrode. Also, it is a very promising material for the electrode of next generation power supply-fuel cell. For application in semiconductor, it is reported that it is a good candidate for the anode in complex metal-oxide semiconductor (CMOS). [11,12] RuO_2 is a good material for O_2 diffusion barrier;[13] and it is a material with supercapacitance.[14] Diffusion barrier (RuO_2) between Al and Si is reported on the application for ferroelectric thin film capacitors used in DRAMs and FeRAMs.[15,16] RuO_2 is

reported as a very promising material for direct methanol fuel cell application (DMFC).[17-20]

1.2 New development and Technology of Integrated Circuit (IC) chip

As mentioned above, with the continued dimensional scaling down in microelectronics devices, now it is clearly getting into the nano-scale node. According to the International Technology Roadmap for Semiconductors (ITRS) the device technology node in CMOS (as shown in Figure 1.2-a) will shrink down to ~40nm in 2011. In that size of node, the diffusion barrier needs to narrow to ~5 nm.

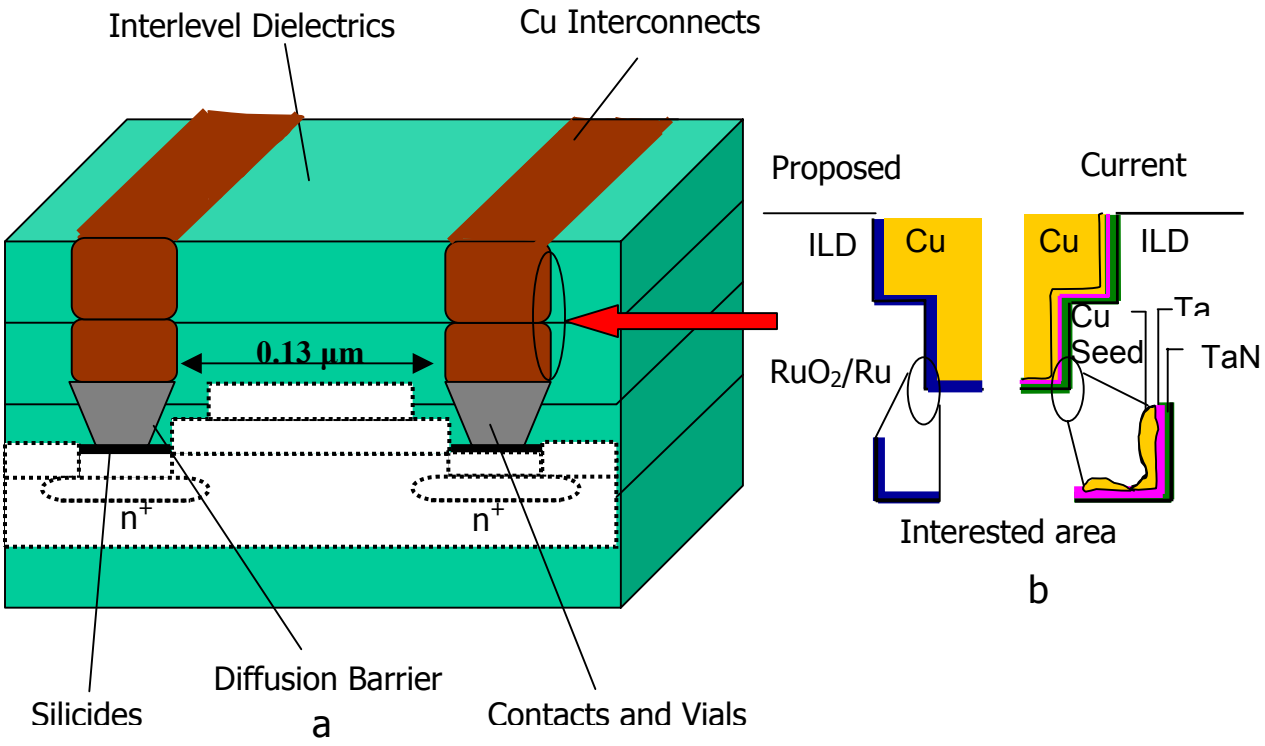

Figure 1.2: a) Cross section of 0.13 μm MOS device; b) The interested area.

The current material-Ta/TaN, which the IC industry is using, cannot be scaled down to that dimension. So there is a big drive for industry to overcome this challenge and to find new materials to solve this problem. Another drawback of Ta/TaN is that the surface conductivity is very bad since Ta is easily oxidized in air. Electrochemical plating of Cu cannot be done directly on the surface. A Cu-seed layer has been plated on the Ta/TaN to facilitate the Cu plating as shown in Figure 1.2-b. Cu-seed layer plating is not a cheap process, especially for nanoscale. This is another driving force to push industry to find a new material to replace the three sandwich layers (shown in Figure 1.2-b)

Ru is a very promising candidate as interconnect Cu diffusion barrier due to its excellent inherent property, chemical resistivity and compatibility for direct plating of Cu. In chapter 2, we will study electrochemical behaviors Ru and its oxide in Cu^{2+} solution, to get basic understanding of Cu plating and Ru's electrochemical behavior in different environment, such as pH effect, Cu concentration effect. et al.

1.3 Surface Analysis Techniques

Surface behavior of materials is crucial to our lives. Whether one considers a car body shell, a biological implant, a catalyst, a solid-state electronic device or a moving component in an engine, it is the surface, which interfaces with its environment. The surface reactivity will determine how well the material behaves in its intended function. It is therefore vital that the surface properties and behavior of materials used in our modern world are thoroughly understood.

Techniques are required which can enable us to analyze the surface chemical and physical state and clearly distinguish it from that of the underlying solid. [21] The general fundamentals of several techniques, which are used in this dissertation, will be introduced in the coming sections.

1.3.1 X-ray Photoelectron Spectroscopy

X-ray photoelectron spectroscopy (XPS), previously known as electron spectroscopy for chemical analysis (ESCA), is a widely used surface science technique. [22] The sample to be analyzed is irradiated by X-rays. Photoelectrons are emitted and separated by energy to be counted. The energy of the photoelectron is related to the atomic and molecular chemical environment from which it is ejected. So, XPS can provide qualitative and quantitative information on nearly all elements present on a sample (except H and He) within ~100 Å depth.

1.3.1.1 XPS Fundamentals

Since photoelectrons must travel a relatively long distance to the detector, XPS must be conducted in ultra high vacuum (UHV; < 10^{-9} torr) to avoid losing the photoelectron on its way to the detector. For XPS analysis an X-ray impinges on an atom and interacts with an electron with a total transfer of energy leading to the ejection of the electron. The ejected photoelectron will have an energy based on the energy of the X-ray:

$$E = h\nu$$

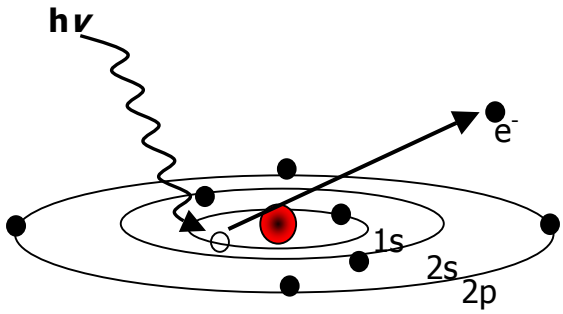

Figure 1.3: Photoelectron ejection of XPS.

.

The energy (E) is the product of Planck's constant (h = 6.623 x 10^{-34} Joules · Second) with the frequency of the X-ray radiation (ν). Thus as the X-ray strikes a core electron in an atom (as shown in Figure 1.3), there is photoemission if the core electron is able to overcome the binding energy (E_B).

Photoemission may be viewed such that:

$$E_B = h\nu - E_K$$

E_B is the binding energy of the electron needed to escape the vacuum energy level where the atom can still exert influence on the electron. E_K is the kinetic energy of the emitted electron.[23] It is this E_K of the emitted photoelectrons, which are channeled through an electrostatic hemispherical electron energy analyzer onto a large area detector that are measured. The hemispherical analyzer establishes an electrostatic field to allow only those electrons of a given pass energy to arrive onto the detector itself.[24]

Since the X-ray photon energy ($h\nu$) and E_k are known, E_B can be calculated. This is important because the binding energy of core level electrons is characteristic for each element. The binding energy also provides important information about the bonding characteristics of the atom from which the core electron photoemission is detected. This chemical shift in binding energy can be seen in particular for Ru. Ru $3d_{5/2}$ electron will give a binding energy of 280 eV,[25] but when it is in Ru oxide (RuO_2) the $3d_{5/2}$ electrons experience a shift towards higher binding energy of 281 eV because Ru becomes more electrophilic due to the proximity of the electron withdrawing oxygen species. A chemical shift towards lower binding energy would be seen if an element was to be in an electron-donating environment. The X-ray photoelectron spectroscopy was accomplished using a ESCALAB MKII spectrometer system (Thermo VG Scientific, West Sussex, England, http://www.noran.com/), using a standard Al-K_α X-ray source at 280 watts and electrostatic analysis in constant pass energy mode of 200 eV for survey scans and 20 eV for regional scans. Figure 1.4 shows the instrument that was used.

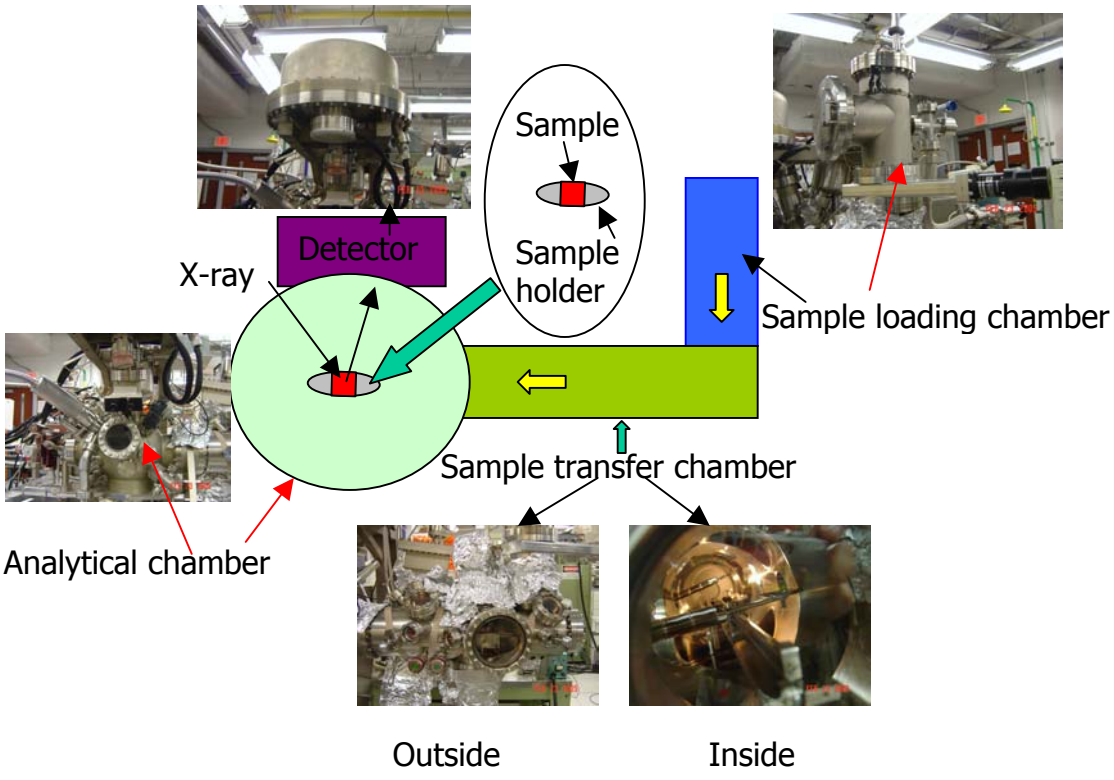

Figure 1.4: XPS instrument.

1.3.1.2 Ar^+ sputtering- Cleaning the Surface

The sample always has contamination from air such as O_2 absorption, or probably worse, forming oxide due to unstable material of the sample. So the sample requires pre-cleaning before collecting XPS data. Usually, *in situ* Ar^+ sputtering is a good method to clean the surface of the sample. Also this is a destructive depth profiling method. It uses Ar^+ bombardment to "etch" away the top layers and to explore layers underneath in which we are interested, as shown in Figure 1.5. In chapter 3, Ar^+ sputtering will be applied to characterize the quality of Ru thin films.

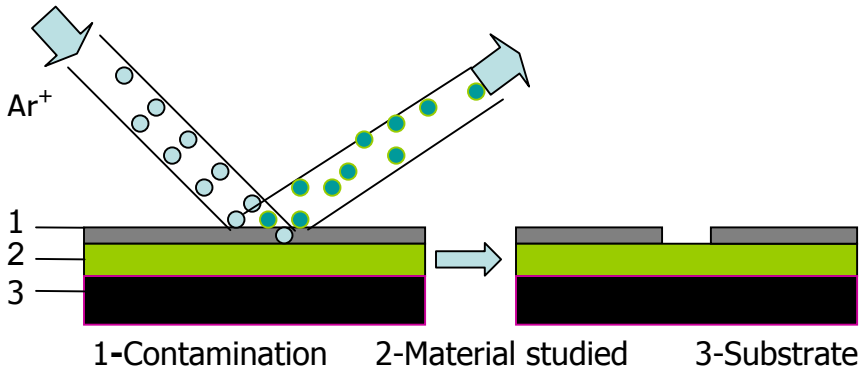

Figure 1.5: Ar^+ sputtering to clean the XPS sample.

1.3.1.3 Resolved Angle

This is a non-destructive depth profiling method. The depth of analysis in XPS varies with the kinetic energy of the electrons under consideration. It is determined by the attenuation length (λ) of electrons, which is related to the inelastic mean free path (IMFP), as shown in the following equation:

$$\lambda = 538 a_A / E_A^2 + 0.41 * a_A (a_A * E_A)^{0.5}$$

E_A is the energy of the electron in eV; a_A^3 is the volume of the atom in nm^3 and λ is in nm.

Usually, 95 per cent of the signal of the electron spectrum will emanate from a depth of $< 3\lambda$. As shown in Figure 1.6, the signal in d_1 depth can be collected in x-ray 1, but d_2 for x-ray 2. ($d_2 < d_1$, $\alpha < \beta$). The relation of effective depth and the incident angel of x-ray (between sample surface and x-ray) can be shown in the following equation:

$$d = 3\lambda.\sin\theta$$

Where 3λ is the maximum depth of XPS in which effective signals can be collected ($\theta = 90^{o}$). With changing the angle between incident x-ray and sample surface from 90^{o} to 0^{0} as shown in Figure 1.6, more signals from the top layers will be collected. Such information can provide a useful guide to relevant

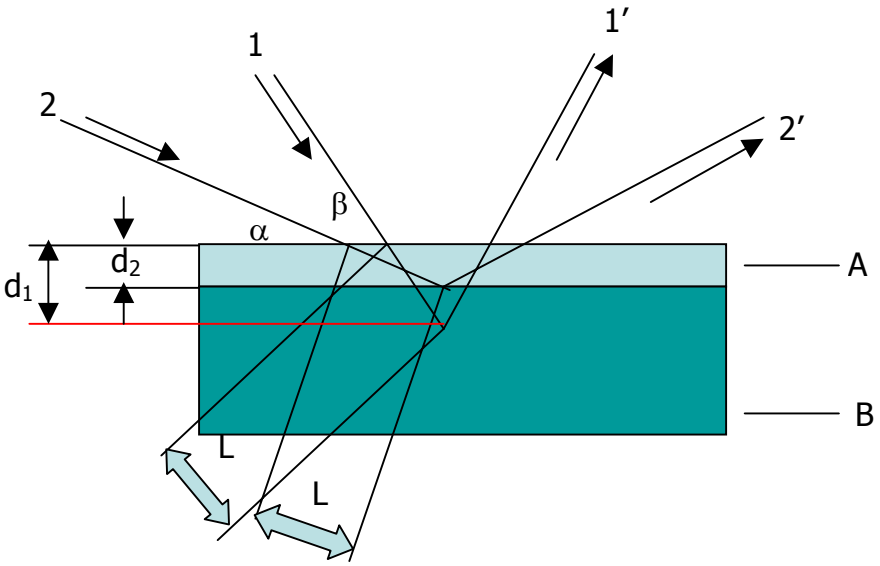

Figure 1.6: Resolved angle for XPS.

abundance of each element in the near surface layers if the thickness is known for an individual layer. The resolved angle XPS analysis will be used to characterize surface chemical change in chapter 3.

1.3.2 Rutherford Backscattering Spectroscopy

Rutherford backscattering spectroscopy (RBS) is based on collisions between atomic nuclei and derives its name from Lord Ernest Rutherford, who was the first to present the concept of atoms having nuclei in 1911. It involves measuring the number and energy of ions in a beam that backscatter after colliding with

atoms in the near-surface region of a sample at which the beam has been targeted. With this information, it is possible to determine atomic mass and elemental concentrations versus depth below the surface. RBS is ideally suited for determining the concentration of trace elements heavier than the major constituents of the substrate. Its sensitivity for light masses, and for the makeup of samples well below the surface, is poor.

When a sample is bombarded with a beam of high-energy particles, the vast majority of particles are implanted into the material and do not escape. This is because the diameter of an atomic nucleus is on the order of 1×10^{-15} m while the spacing between nuclei is on the order of 2×10^{-10} m. A small fraction of the incident particles do undergo a direct collision with a nucleus of one of the atoms in the upper few micrometers of the sample. This "collision" does not actually involve direct contact between the projectile ion and target atom. Energy exchange occurs because of coulombic forces between nuclei in close proximity to each other. However, the interaction can be modeled accurately as an elastic collision using classical physics.

The energy measured for a particle backscattering at a given angle depends upon two processes. Particles lose energy while they pass through the sample, both before and after a collision. The amount of energy lost is dependent on that material's stopping power. A particle will also lose energy as the result of the collision itself. The collisional lost depends on the masses of the projectile of the target atoms. The ratio of the energy of the projectile before and after collision is

called *the kinematic factor*. The number of backscattering events that occur from a given element in a sample depend upon two factors: the concentration of the element and the effective size of its nucleus. The probability that a material will cause a collision is called its *scattering cross section*.

As the projectile passes through the medium it suffers an average energy loss dE/dx and this leads to the concept of the stopping cross-section. Eventually, particles entering a solid with a given energy will not have identical energy after traveling the same distance because there are statistical fluctuations in the energy loss of projectiles as it goes through a solid. This phenomenon is called energy straggling. The above four basic physical concepts form the basis of RBS. The kinematic factor leads to the ability for mass analysis. The scattering cross-section provides RBS with a quantitative capability. The stopping cross-section results in the capability for depth analysis and energy straggling sets limits on mass and depth resolution. The spectrum is shown as Figure 1.7

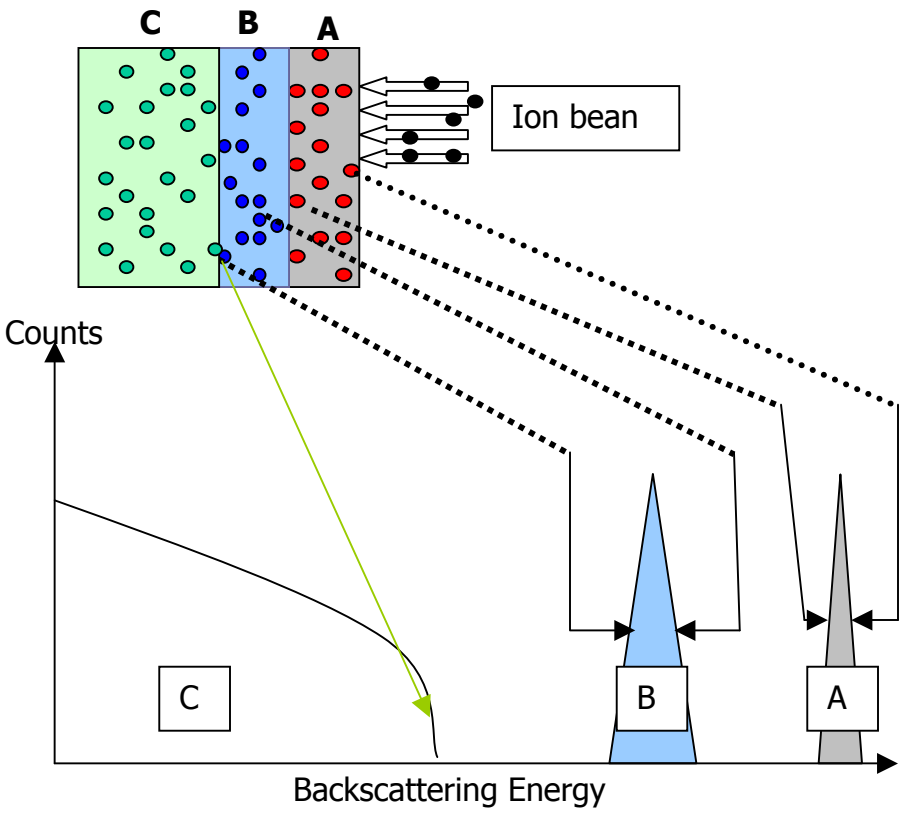

Figure 1.7: RBS spectrum.

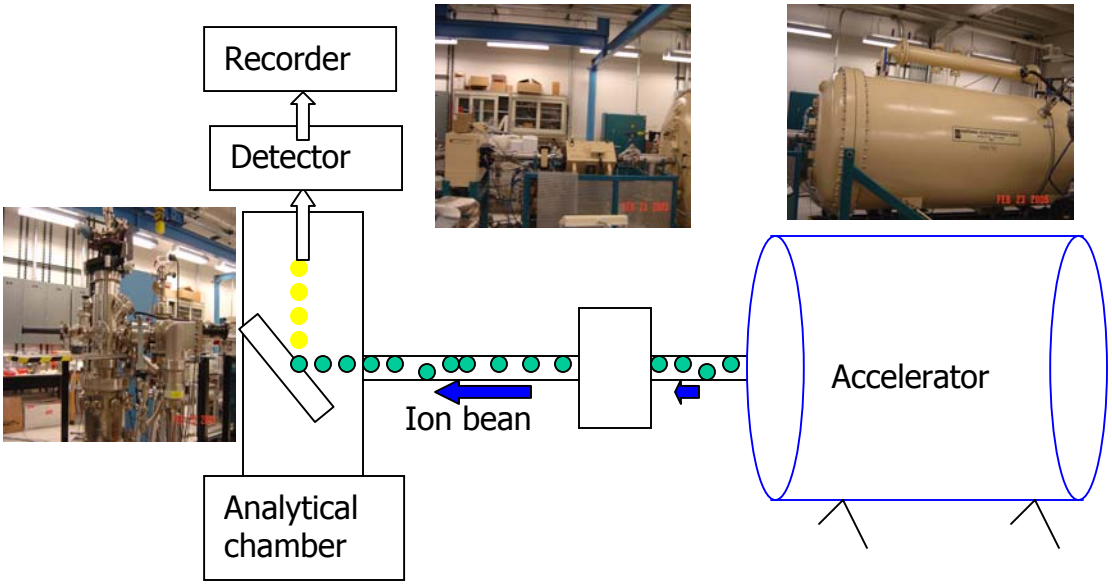

Figure 1.8: RBS instrument.

In chapter 3 of this dissertation, RBS will be used to investigate thermal stability of a Cu/Ru/Si stack. RBS analysis was performed using 2.3 MeV He^+ beam and a scattering detection angle of 160^o in a UHV end station of the 3 MeV NEC 9SH Pelletron accelerator as shown in Figure 1.8.

1.3.3 Secondary Ion Mass Spectrometry (SIMS)

SIMS is widely used for analysis of trace elements in solid materials, especially semiconductors and thin films. Bombardment of a sample surface with a primary ion beam followed by mass spectrometry of the emitted secondary ions constitutes (SIMS) as shown in Figure 1.9. The SIMS ion source is one of only a

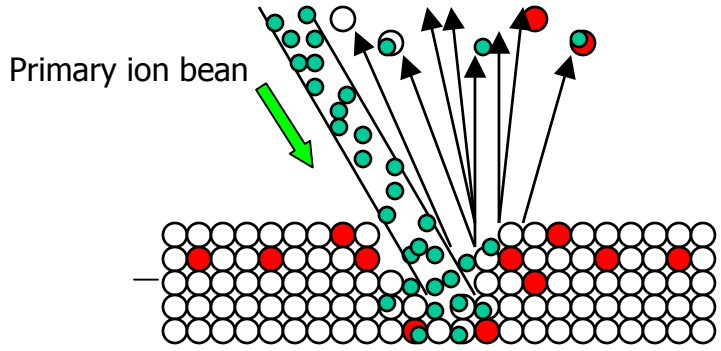

Figure 1.9: Schematic of SIMS.

few to produce ions from solid samples without prior vaporization. The SIMS primary ion beam can be focused to less than 1 um in diameter. Controlling where the primary ion beam strikes on the sample surface provides for microanalysis, the measurement of the lateral distribution of elements on a microscopic scale. During SIMS analysis, the sample surface is slowly sputtered away. Continuous analysis, while sputtering produces information as a function

of depth, is called a depth profile. When the sputtering rate is extremely slow, the entire analysis can be performed while consuming less than a tenth of an atomic monolayer. This slow sputtering mode is called static SIMS in contrast to dynamic SIMS used for depth profiles. Shallow sputtering minimizes the damage done to organic substances present on the sample surface. The resulting ion fragmentation patterns contain information useful for identifying molecular species. Only dynamic SIMS will be treated in this surface analysis computer aided instruction package because only dynamic SIMS yields quantitative information. SIMS will be used to characterize Cu/(5 nm Ru)/Si structures In chapter 3. Analyses were performed in a Cameca 6f spectrometer.

1.3.4 X-Ray Diffraction (XRD)

XRD is a very valuable technique to characterize materials. In this dissertation, it will be used in chapter 4 to help to understand the electrochemical reaction mechanism for Ru in pH 5 solutions.

1.3.4.1 Generation of X-ray

Since the X-ray was first discovered by W. C Roentgen in 1898,[26] his work followed by that of H. G. Mosely (1912), W. L. and W. H. Bragg (1913), and other pioneers led the way to the development of many techniques essential to characterize materials. The ability to do such a remarkable diagnostic work is the result of the continuing evolution of X-ray science and technology that is drawn heavily on advances in electronics, materials science, mechanical engineer and computer. How the X-ray was generated?

X-ray of XRD usually is generated in an x-ray tube (Figure 1.10), where a focused electron beam is accelerated across high voltage field between filament and a target. When the accelerated electrons collide with the atoms on the target, X-rays with energy characteristically particular to the target are eradiated towards a test sample. [27, 28] Table 1.2 lists some targets used in X-ray tubes and their characteristic wavelength.

Table1.2: Target elements of X-ray source of XRD.

Element of target	Cu	Ni	Ag	Mo	Co
Wavelength (Å)	1.54	1.66	0.559	0.71	1.79

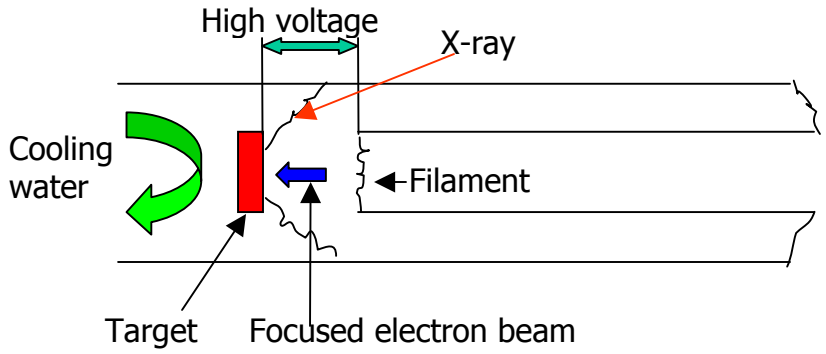

Figure 1.10: Schematic of an X-ray tube.

1.3.4.2 Bragg's Law

W.L. Bragg (1913) was first to show the scattering process which leads to diffraction can be equally visualized as if the X-ray were reflecting from the imaginary planes defined by Miller indices. In Figure 1.11, X-rays impinge on a set of atomic planes, with indices (hkl) from the left, making an angle θ with

them. The distance between the planes is d. And we can see that beam b must travel the distance ABC farther than beam a. Constructive interference or

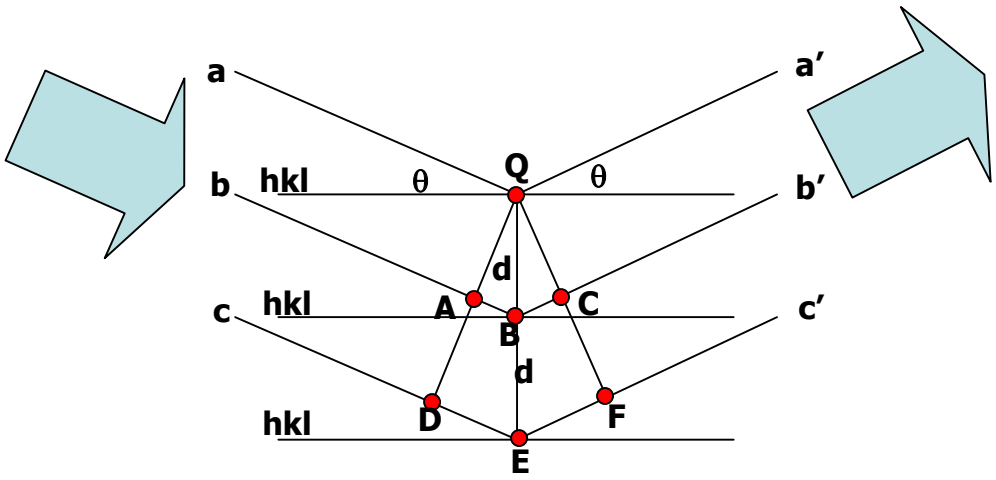

Figure 1.11: Diffraction of X-rays from the planes in a crystal.

diffraction will occur when the two waves (a and b) come out in phase (a' and b'). This, of course, will happen when the distance ABC=1λ or 2λ or 3λ, in general, when

$$n\lambda = ABC$$

Where n is an integer. If we look into the triangle OAB and notice that $d.\sin\theta = AB$, or $2\ d.\sin\theta = ABC$. So, the condition for diffraction to occur is

$$n\lambda = 2\ d\ \sin\theta$$

This is the famous equation first derived by W.L Bragg and called Bragg's law. This law allows us to relate the distance between a set of planes in a crystal and the angle at which will diffract X-ray of a particular wavelength.

1.3.4.3 XRD Application

As a sample is scanned in a certain range of θ, the X-ray diffraction pattern is recorded, peaks corresponding to the various d spacing in the crystal lattice are recorded and the positions and the intensities of the peaks are used for identifying the underlying structure (or phase) of a given material. For example, the diffraction lines of Si (100) would be different from Si (111) even though they both are made of Si atoms. This phase identification is important because the material properties are highly dependent on structure.

XRD is capable of probing samples of single crystals or polycrystalline form as either films or powders. The technique has been found to provide such useful information for powder analysis, thin film analysis, texture measurements, residual stress measurements and crystallography and is used extensively.

In this dissertation, X-ray diffraction studies were conducted using a Siemens D500 diffractometer (Siemens AG, Munich Germany, http://www.siemens.com/). The tube source was operated using Cu K_α radiation, which emits x-rays with wavelengths of 1.54 Å at 40kV and 30 mA. Scans of two theta (2θ) were run at 0.05^o steps and a 1 second dwell time.

1.3.5 The Transmission Electron Microscope (TEM)

1.3.5.1 TEM Fundamentals [29, 30]

A TEM works much like a slide projector. A projector shines a beam of light through (transmits) the slide, as the light passes through. It is affected by the structures and objects on the slide. These effects result in only certain parts of

the light beam being transmitted through certain parts of the slide. This transmitted beam is then projected onto the viewing screen, forming an enlarged image of the slide. TEMs work the same way except that they shine a beam of electrons (like the light) through the specimen (like the slide). The transmitted beam of electron will be affected by the material being transmitted, and bring the information of the materials to form an image on the screen. Thus, the TEM image can be interpreted to the information with which we are concerned.

Figure 1.12 shows the ray path of the TEM, electrons (60-150KeV) are emitted in the electron gun by thermionic emission filament. A two-stage

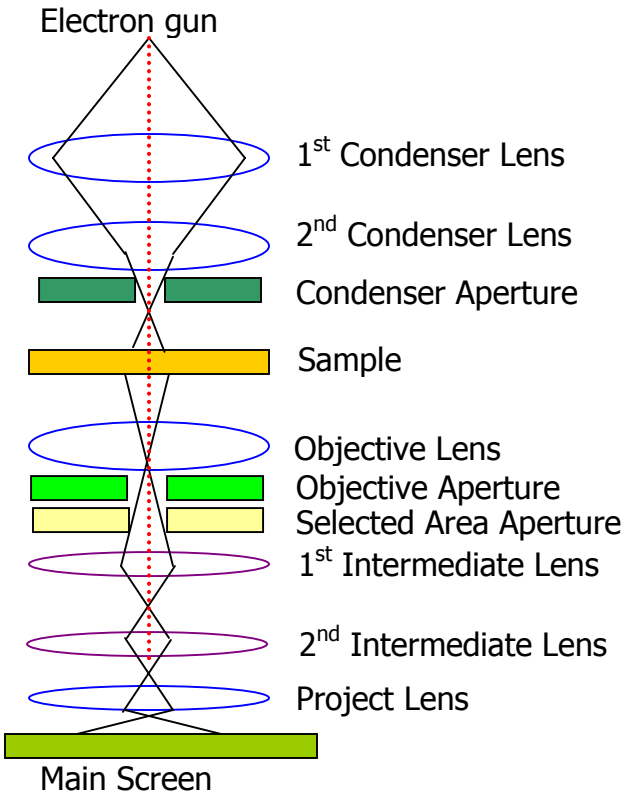

Figure 1.12: Schematic ray path for a transmission electron microscope.

condenser-lens system permits variation of the illumination aperture and the area of the specimen illuminated. The electron intensity distribution behind the specimen is imaged with a three or four stage lens system onto a screen. The image can be recorded by direct exposure of a photograghic emulsion inside the vacuum or digitally by camera.

1.3.5.2 TEM application

TEM is used heavily in both material science/metallurgy and the biological sciences. It allows the user to determine the internal structure of materials.

In both cases, the specimen must be specially prepared to a thickness which must be like as a thin foil, or etched so some portion of the specimen is thin enough to allow electrons to transmit through the sample, much like light is transmitted through materials in conventional optical microscopy. Because the wavelength of electrons is much smaller than that of light, the optimal resolution attainable for TEM images is many orders of magnitude better than that from a light microscope. Thus, TEMs can reveal the finest details of internal structure - in some cases as small as individual atoms.

TEM can provide high resolution because elastic scattering is an interaction process that is highly localized to the region occupied by the screened coulomb potential of an atomic nucleus. Whereas inelastic scattering is more diffuse; it spreads out over about a nanometer. TEM has the advantage to show the image thickness or crystalling specimens. In chapter 3, TEM will be used to characterize

Ru/Si and Cu/Ru/Si stack and the thermal stability of the structure, in which Ru as Cu diffusion barrier. Images of TEM will be discussed in detail.

1.4 Electrochemical Techniques

The science of electrochemistry was born at the end of the eighteenth centaury following intense interest in the production of electricity by animals such as the electric eel. From that starting line, electrochemistry has obtained a big development and applied in many areas in our life, such as plating metal, analysis and organic synthesis. [31] In this research, two main technical will be used: cyclic voltammetry (CV), chronoamperometry (CA), they will be specified later, but before we get in that details, some of the fundamental acknowledge will be presented first.

1.4.1 The Inhomogeneous Nature of Electrochemical System[32]

Electrochemical reactions can only take place at the interface of some electrode substrate and some conducting electrolyte solution. It is important to know that only the part of the electrode in immediate contact with the electrolyte can be affected. If there is no interface, there won't be any reaction happen. it is important to realize that the composition of the electrolyte varies with proximity to the electrode.

Figure 1.13 is a general representation of the interface area in electrochemical system. In fact, all the electrode reaction try to make the composition in the nearby solution different from that further away. At the electrode/electrolyte interface there is a very small area where the distribution of shifting electrons of

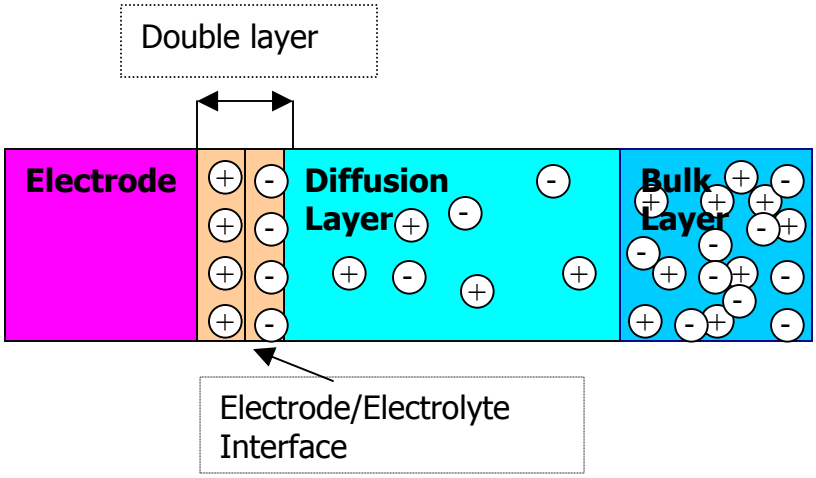

Figure 1.13: Physical structure of zones of electrode system.

the electrode is different from the rest of the electrode. The part of the solution close to the electrode, where the composition is affected by reaction, is named diffusion layer. It is quite small on usual dimension of cells, only 10^{-4}-10^{-1} cm. Further away from the electrode is the homogeneous bulk solution, where the composition is uniform.

Of even smaller dimension is the structure in the immediate vicitity of the interface. It is intuitive that the part of the solution very near to the electrode, within a few monolayers, must differ in structure from the characteristic of more remote cones, simply because this part of the system is forced to interact with the electrode, which apparently has a very different character from the bulk solvent, likewise, the distribution found in the interior of the metal. These interfacial zones on the two sides of the interface have dimensions of a few tens

of angstroms. Because that is the scale on which interatomic and intermolecular forces operate, the whole structure is called double layer.

An overall electrochemical reaction is the chemical change accompanying charge transfer across at an electrode/electrolyte interface. Its rate is limited by the speed and amount of reactants that can be moved from the bulk solution to the double layer by *mass transport*. Mass transport can be accomplished by diffusion, convection or migration.

1.4.2 Current: Working vs. Counter Electrodes

The working electrode is the electrode where we study chemical reactions. Reactions at the working electrode involve a transfer of charge. Electroneutrality must be performed as electrons are either extracted from or drawn into the working electrode for reactions to occur. To this effect a *counter electrode* is used to preserve electroneutrality by allowing electron flow and keeping charge buildup to a minimum. Electron will pass through the external circuit and back into the solution at the counter electrode.

Since the electrons are used or supplied on an integral, stoichoimetric basis in the electrode reaction, as show in the following, it is also important to note that the flow of electrons at the electrodes is directly proportional to the reaction rate. Consider the equation for the total charge passed (Q):

$$Q=nFN$$

N is the number of moles of reactants taken part in, n is the number of electrons per molecule involved in a reaction, and F is Faraday's constant, which

is 96,485 coulomb/mole of electrons. The rate of reaction, and therefore the rate of change in total charge is expressed as follows:

$$dQ/dt = nF*dN/dt = I$$

It shows that the rate change in total charge (dQ/dt) is the current I. Current (I) is expressed in terms of amperes.

1.4.3 Potential: Working vs. Reference Electrode

The energy required to move an electron from some arbitrary point A to point B is commonly referred to as *potential*. Physically, potential is the amount of work required to move an electron from an infinite point in space to a point of interest, for electrode chemical system, that point is at working electrode surface. More negative potentials are applied by increasing negative excess charge on an electrode to give higher electron energies. Adversely, more positive or less negative potentials are applied by increasing positive excess charge or decreasing electron energies. When studying electrochemical systems, the potential is the voltage difference between the working electrode and a *reference electrode*. The reference electrode won't be affected by the chemical processes occurring at the working electrode and is established in such a way that it is in equilibrium and does not pass current usually by containing a high concentration of electroactive species that are not sensitive to current flow. Thus a reference point is provided which the working electrode can be measured against.

If a negative potential is applied to working electrode, it may absorb the cations (positive ions) from the solution, which can neutralize the excess electrons at the surface of electrode. So when a reduction reaction occurs at cathode, at the same time oxidation will happen on anode. The working electrode could act as both anode and cathode. It just depends on what potential was applied to it. In this case, another electrode, named counter or auxiliary electrode, is introduced. It will help in the flow of current through the electrolyte by complementing the electrical polarity of working electrode.

Figure 1.14 illustrates the standard three-electrode system by which most electrochemistry is conducted. It must be noted that current and potential can

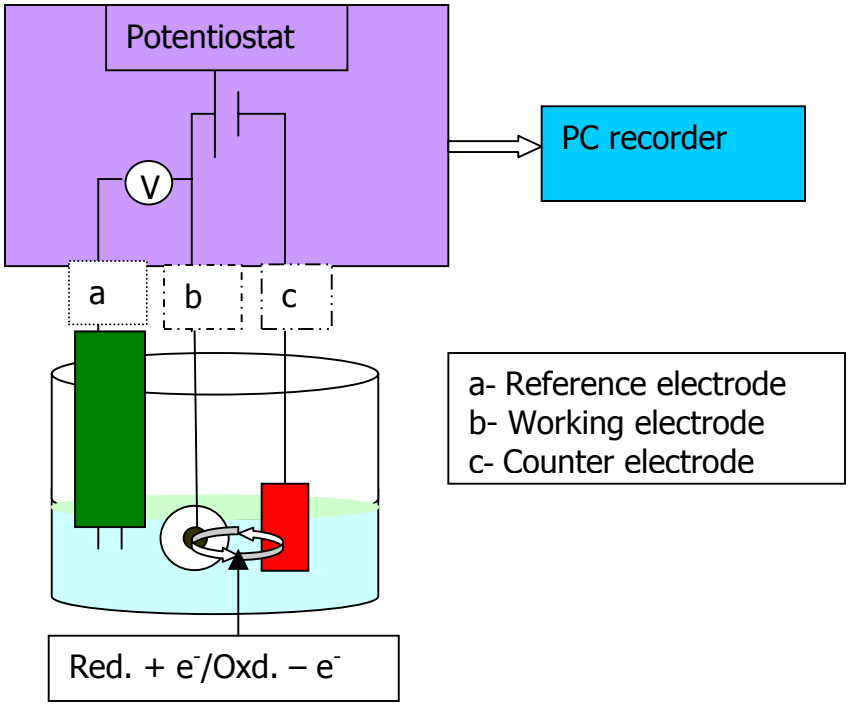

Figure 1.14: Three electrode system.

only be controlled separately, [32] never simultaneously, because potential applied will cause a current to flow in the circuit and a current controlled will set a

voltage. A device with feedback control called a potentiostat is capable of applying current to the working – counter electrodes, while monitoring the potential of the working versus the reference electrode.

An Eg&G Princeton Applied Research model 273A Potentiostat/Galvanostat (PerkinElmer, Inc., Wellesly, MA, http:www.perkinelmer.com/) and CHI 440 (CH Instruments) were used to obtain electrochemical data.

1.4.4 Open Circuit Potential

The OCP value is the potential of the working electrode versus the reference electrode when there is no current applied to the system. OCP is also a very electrode surface sensitive quantity and has been used extensively. Chapter 2 and 4 will use OCP as a fast way to tell if the surface of electrode is cleaned, including physical and electrochemical cleaning, for example, Ru metal's OCP in electrolyte is ~0.42 eV vs Ag/AgCl. If a reading is very far away from 0.42 eV, we know there is a problem.

1.4.5 Cyclic Voltammetry

Cyclic Voltammetry (CV) is an electrochemical technique where a working electrode goes through potential scan across a potential window. Usually starting from the open circuit potential (OCP) and scanning toward an anodic (or cathodic) vertex potential and then to an analogous cathodic (or anodic) vertex potential finishing back at the OCP completes one cycle, thus the cyclic voltammetry also was called potential cycling. By sweeping the potential across the potential window at a preset scan rate (for example 20 mV/sec) a cyclic

voltammogram (CV) plot is recorded as potential vs. current plot. In this way cyclic voltammetry can simultaneously "force: electron-transfer by applied potential and leads to subsequent chemical reactions. The information about consequences of electron transfer and the electron transfer kinetics and thermodynamics of a given redox couple on an electrode surface can be extracted from CV plots. CV will be used in chapters 2 and 4, and CV plots will be analyzed in detail.

1.4.6 Chronoamperometry

Chronoamperometry (CA) is an electrochemical technique, which involves the application of a potential step to the working electrode for a given time. Essentially current is collected with respect to time at a given potential. The applied potential was determined by what are you going to do. If you want remove (deposit) certain surface materials, a oxidizing (reducing) potential should be applied. A chronoamperogram of current versus time is obtained and the data may be disseminated for useful information. The CA technique is used for examining nucleation and growth mechanisms of materials on the working electrode surface.

CA will be used in chapter 2 to load UPD Cu on Ru and Ru Oxide. In chapter 3, it will be using to plate Cu electrochemically to study Cu diffusion barrier-Ru, and in chapter 4, it will be used to load some compounds at a certain potential to prepare ex-situ XPS samples.

1.5 References

1) http*://www.ti.com/corp/docs/kilbyctr/kilby.shtml*

2) Back to the Future: Copper Comes of Age, *http://domino.research.ibm.com/comm/wwwr_thinkresearch.nsf/pages/copper397.html;* IBM Corporation: New York (**1997**).

3) S. P. Murarrka, Mater. *Sci. Eng. R,* **19**, 87 (**1997**).

4) A. Jain, K. M. Chi, T. T. Kod M. J. Hampden-Smith, *J. Electrochem. Soc.,* **140**, 1434 (**1993**).

5) Shacham-Diamand, *J. Electron. Mater.*, **30**, 336 (**2001**).

6) International Technology Roadmap for Semiconductor -2002 Update,Semiconductor Industry Association (**2002**), pp. 74-75; see http://public.itrs.net/.

7) Ishita Goswami and Ravi Laxman, ATMI, San Jose, *Semiconductor International,* 5, (**2004**).

8) Vandenbroucke, D.A., R.L.V. Meirhaeghe, and F. Cardon, *J. Phys. D: Appl. Phys.,* **18**, 731 (**1985**).

9) R.J. H. Clark, *The Chemistry of Ruthenium*, New York: Elsevier, p12, (**1984**).

10) H. S. Momose, M. Ono, T. Yoshitomi, T. Ohguro, S. Nakamura, M. Saito, and Hiroshi Iwai, "Tunneling Gate Oxide Approach to Ultra-High Current Drive in Small-Geometry MOSFETs," *IEDM Tech. Digest*, p238 (**1994**).

11) Zhong, Huicai *Ru-based Gate electrodes for Advanced Dual-Metal Gate*

CMOS Devices, a dissertation to the graduate Faculty of North Carolina State University, (**2001**).

12) T. S. Kalkur and Y. C. Lu, *Thin Solid Films*, **205**, 266 (**1991**).

13) C. G. Parker, " *Device Quality Remote Plasma-Enhanced Chemical Vapor Deposited (RPECVD) Gate Dielectrics for MOS Applications*", a dissertation submitted to the Graduate Faculty of North Carolina State University, 1998.

14) B. E. Conway, *Electrochemical Supercapacitor*s, Kluwer-Plenum, New York: Kluwer Academic (**1999**).

15) G. Lucovsky, H. Yang, H. Niimi, J. W. Keister, J. E. Rowe, M. F. Thorpe, and J. C. Phillips, "*Intrinsic limitations on device performance and reliability from bond constraint induced transition regions at interfaces if stacked dielectrics*", presented at International Conference on Silicon Dielectric Interfaces, Raleigh, NC, Feb (**2000**).

16) Y.T. Kim, C.W. Lee, and S.K. KwakAppl. *Phys. Lett*. **67**(6), 807 (**1995**).

17) A. S. Arico, G. Monforte, E. Modica, P.L. Antonucci, V. Antonucci, *Electrochemistry Communications,* **2**, 466 (**2000**).

18) J.P. Popic, M.L. Avramov-Ivic, N.B. Vukovic, *Journal of Electroanalytical Chemistry,* **421***,* 105 (**1997**).

19) N. Matsui, K. Anzai, N. Akamatsu, K. Nakagawa, N. Ikenaga, T. Suzuki, *Applied Catalysis A.*, **179**, 247 (**1999**).

20) L. Zang, H. Kirsch, *Angew. Chem. Int. Ed.* **39**, 3921 (**2000**).

21) J.M Walls, *Methods of Surface analysis*, Printed In Great Britain at the

University Press, Cambridge, (**1989**).

22) Jone F. Watts and John Wolstenholme, *An introduction to surface analysis by XPS and AES*. New York: J. Wiley (**2003**).

23) Ebel, M.F., *Absolute calibration of an X-Ray photoelectron Spectrometer, Journal of Electron Spectroscopy and Related Phenomena*, **8**, 213 (**1976**).

24) Vickerman, J. C., Ed. *Surface Analysis - The Principal Techniques*; John Wiley & Sons: New York, (**1997**).

25) Wagner, C. D.; Riggs, W. M.; Davis, L. E.; Moulder, J. F. *Handbook of X-ray Photoelectron Spectroscopy*; Physical Electronics: Eden Prarie, MN, (**1995).**

26) Eric Lifshin, *X-ray Characterization of Materials*, New York (**1999**).

27) Klug, H. P., Alexander, L. E. *X-ray Diffraction Procedures: For Polycrystalline and Amorphous Materials*; Second ed.; Wiler-Interscience: New York, (**1974**).

28) James, R. W. *X-ray Crystallography:* Fifth ed.; Butler and Tanner LTD.: London, (**1962**).

29) Ludwig Reimer, *Transmission Electron Microscopy,* New York: Springer-Verlag, (**1993**).

30) Andreas Rosenauer, *Transmission electron Microscopy of Semiconductor Nanostructures,* New York: Springer (**2002**).

31) R. Kalvoda and Roger Parsons, *Electrochemistry in Research and Development*, New York: Plenum press, (**1985**).

32) Larry R. Faulkner, *Journal of Chemical Education*, **60** (4), 262 (**1983**).

CHAPTER 2

COPPER DEPOSITION ON RUTHENIUM AND RUTHENIUM OXIDE*

2.1 Introduction

Cu has been utilized to replaced Al as an interconnect metal in IC industry since 1997[1, 2]. Electrochemical Cu deposition has received considerably attention due to its low cost and relatively mild operating condition. The scaling-down trend of CMOS in IC chip drives the industry to look for a new material as Cu diffusion barrier. Ruthenium has shown to be a promising candidate for a copper diffusion but has seen limited studies, especially with copper deposition on ruthenium/ruthenium oxide in a copper plating solution. This chapter will describe the depth study of Cu plating on Ru and RuO_x. Especially, the investigation of Cu under-potential deposition (UPD) on Ru and RuOx will be in greater detail.

The electrochemical deposition of a metal A on an electrode B in the sub-monolay*er regime occurs at more positive potentials as compared to the Nernst potential if the interaction of A with B is thermodynamically more advantageous than that of A with A. We call this phenomenon as under potential deposition (UPD).

Cu UPD study was reported extensively on Pt, Au. Akiyoshi Kuzume and coworker studied Cu UPD on different Au single crystal-Au(111), Au(110),

* The majority of this chapter has been previously published: Zhang, Yibin; Huang, Long; Arunagiri, Tiruchirapalli N.; Ojeda, Oscar; Flores, Sarah; Chyan, Oliver; Wallace, Robert M Electrochemical and Solid-State Letters (2004), 7(9), C107-C110. Reproduced with permission from the Electrochemical Society, Inc.

Au(100), Au(554), Au(775), Au(332) and Au(755).[3] Dijana Simkunaite et. al investigated how addictives affected Cu UPD on polycrystalline Pt electrode in the presence on H_2SeO_3,[4] Martinez-Ruiz and coworker investigated the kinetics of Cu Underpotential Deposition on Iodine-Modified Au(111) Electrodes,[5] Zei, M. S. reported effect of chloride anions on Cu electrodeposition onto Pt(110) and Pd(110) surfaces.[6]

Interestingly, Cu UPD was observed first time on Ru oxide in the present study. Ruthenium oxide (RuO_2) exhibits distinct physical and chemical properties and is an important material for a wide range of technological applications. [7-9] RuO_2 has metal-like electronic conductivity (as high as 35 μΩ.cm) originating from partial filling of the d orbital in its tetragonal rutile structure. [10] In electrochemistry, RuO_2 is used as a corrosion resistant, low overpotential electrode for Cl_2 and O_2 production in the chloro-alkali industry, and also as a charge storage electrode in ultracapacitors for energy storage application.[11-12] In heterogeneous catalysis, RuO_2 serves as a promising material for direct methanol fuel cell application, catalytic oxidation of methane to synthesis gas and a robust catalyst for CO oxidation. [13-15]

Owing to its excellent thermal and chemical stability, conductive RuO_2 also attracts wide interests in the integrated circuit device applications, such as the oxygen-resistant contact electrode for ferroelectric memory devices, diffusion barrier for Al interconnects, and conductive wiring in integrated circuits. [16-17] We recently reported a new approach of utilizing Ru-based materials as a directly

plate-able, seed-less Cu diffusion barrier for advanced 65 and 45 nm nodes application.[18] Our experimental results demonstrate that the interfacial electrochemistry between Cu and Ru plays a key role in the barrier performance. Specifically, our data, as also those reported in the literature, show that Cu plates underpotentially on Ru. The Cu UPD deposition reflects the strong binding, and also the strong adhesion between Cu and Ru. Since Ru has a strong affinity to oxygen, in this chapter, we explore the interfacial electrochemistry between Cu and electrochemically oxidized Ru electrode substrate.

Unlike UPD on a metal surface, the literature report of Cu UPD on a transition metal oxide surface is relatively scarce. Existing reports focused on the effects of adsorbed oxygen or sub-monolayer residual oxides on Cu deposition. [19, 20] In this chapter, we systematically study Cu deposition on various thicknesses of hydrous ruthenium oxide electrode surface by the progressive cyclic voltammetry (CV) and x-ray photon electron spectroscopy (XPS). Our data demonstrate, for the first time, that Cu UPD also takes place on the conductive hydrous ruthenium oxide surface. The affecting factors (pH change, Cl^- concentration, et al) for Cu UPD and OPD on Ru and Ru oxide were explored. Also the comparison of the electrochemical behavior was carried out between RuO_x formed electrochemically and RuO_x formed thermally. The implication of Cu UPD on the Ru-based Cu-diffusion barrier is discussed.

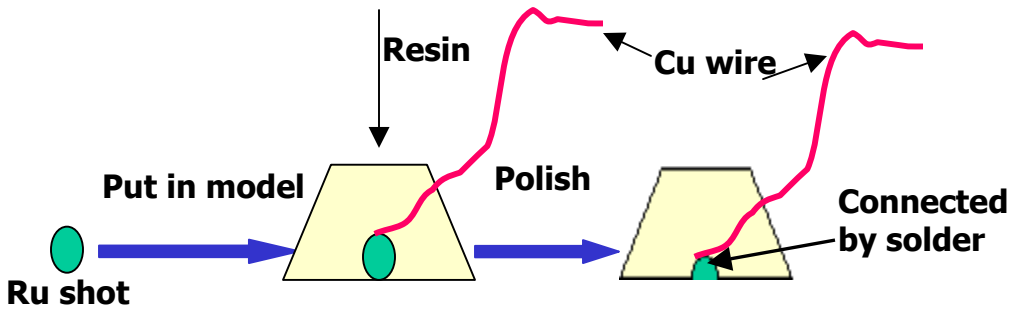

Figure 2.1**:** Process to make electrode (Copyright 2005 by Yibin Zhang).

Ru shots (ESPI Inc.) were made into disk electrodes as described in the reported procedure,[18a] as shown in Figure 2.1. High purity copper sulfate (Aldrich) and sulfuric acid (Mallinckrodt) were used to make all electrolyte solutions in ultra-pure water (18.2 MΩ, Millipore). Electrochemical investigation was performed using CHI 440 (CH Instruments) and model M273 (EG&G, Princeton Applied Research) Potentiostat/Galvanostats. A conventional three-electrode cell with a Pt sheet as the counter electrode and silver/silver chloride (3 M NaCl) as the reference electrode was employed. All solutions were pre-purged by N_2. The copper plating on Ru and oxidized Ru electrodes was carried out under N_2 ambient. Hydrous ruthenium oxide was electrochemically prepared by oxidizing a freshly prepared Ru electrode at 1.3 V for 3 minutes in a 0.5 M H_2SO_4 solution. X-ray photon electron spectroscopy (XPS) data were collected using a VG ESCALAB MKII spectrometer (VG Scientific Ltd) with an Al K_α x-ray as

the excitation source. All the anneal process was performed in the oven (Lindberg/Blue M TF55035A-1) with N_2 purging. Optical images were recorded using a Nikon ME600L microscope**.**

2.3 Results

Figure 2.2 shows progressive cyclic voltammograms (CV) collected from a freshly prepared Ru electrode immersed in a 2 mM $CuSO_4$/0.5M H_2SO_4 solution

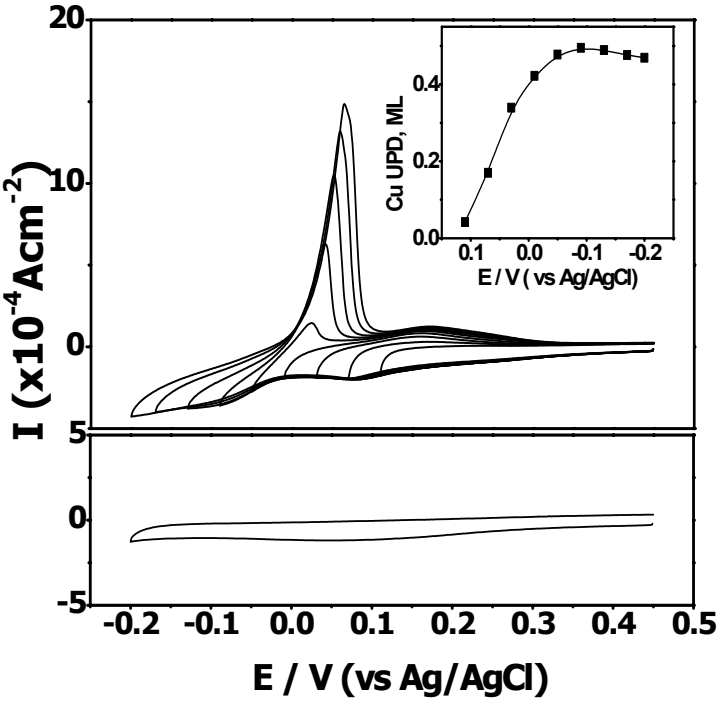

Figure 2.2: Top: progressive cyclic voltammograms collected from a freshly prepared Ru electrode immersed in a 2 mM $CuSO_4$/0.5M H_2SO_4 solution, insert : Cu UPD monolayer coverage vs. cathodic switching potentials. bottom: background CV in 0.5M H_2SO_4 solution. Scanning rate = 20 mV/sec**.**

purged by nitrogen. The CV scans start at the open circuit potential of Ru electrode, 0.45 V vs. Ag/AgCl, and move progressively negative to allow Cu^{2+} ions adsorption/reduction/deposition to take place on Ru electrode surface. On the reverse anodic scan the deposited Cu overlayers are oxidized and stripped from Ru electrode surface. The progressive increase of cathodic switching potentials helps to visually identify the potential range of Cu UPD growth. Two regions of interest can be seen in the cathodic scans of Figure 2.2. A small cathodic current increase between 0.1 V to 0 V followed by a larger cathodic current after 0 V. The equilibrium Nernst potential for Cu/Cu^{2+} is around 0.06 V (vs. Ag/AgCl) for 2 mM $CuSO_4$ solution. Therefore, the first current increase is assigned as an UPD of Cu on Ru electrode surface, followed by the over-potential deposition (OPD) of Cu bulk deposition. The Cu UPD monolayer (ML) coverage on Ru electrode surface is calculated from the integrated charge of UPD stripping peak after subtracting its background. As shown in the inset of Figure 2.2, the surface coverage of Cu UPD increases with cathodic potential and reaches a plateau of ca. 0.45 ML beyond – 0.05 V.

The conductive oxide is prepared electrochemically by holding the Ru electrode at + 1.3 V in 0.5 M H_2SO_4 solution for three minutes. Vigorous oxygen evolution accompanied by the brownish red solution species (likely RuO_4^{2-}) are generated from the Ru electrode surface during the anodic polarization. The optical pictures of Ru and Ru oxide under microscope was shown in Figure 2.3. Figure 2.3-a is Ru itself. Figure 2.3-b is the RuOx formed by holding at 1.1 V for

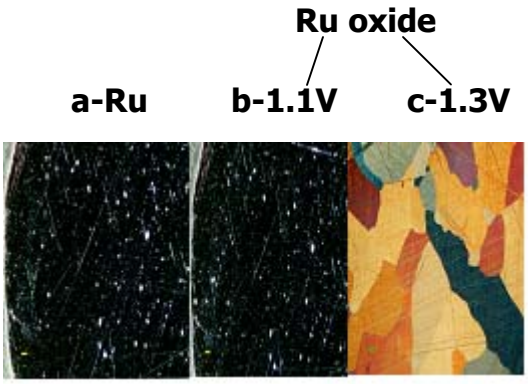

Figure 2.3: Optical pictures of Ru and Ru oxide (Copyright 2005 by Yibin Zhang).

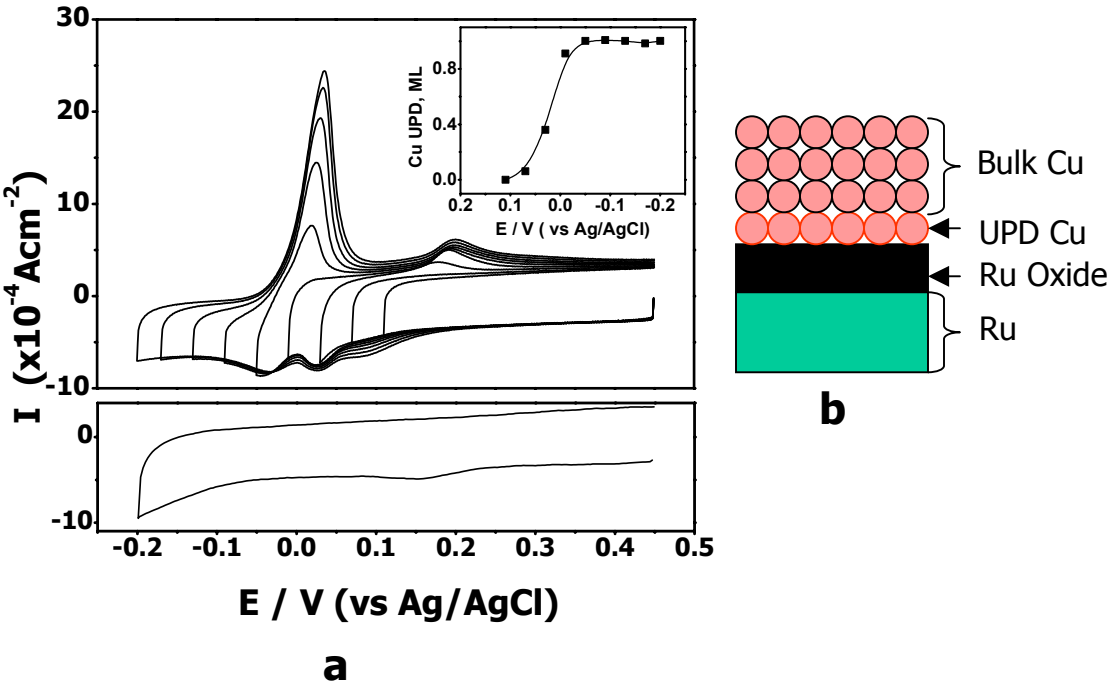

Figure 2.4: a) Conditions are Similar to figure 2.2, except a hydrous ruthenium oxide electrode (electrochemically prepared by holding Ru electrode at +1.3V for 3 minutes) was used to collect all CV; b) Physical structure of copper deposition on RuO_x/Ru electrode.

3min in 0.5M H_2SO_4; Figure 2.3-c is 1.3 V holding for 3min. We believe that colorful picture is from different Ru crystal structure. The oxidized Ru electrode has an open circuit potential of + 0.9 V with a dark blue-black color appearance indicating a thick oxide formation. The as-prepared oxidized Ru electrode is subjected to the same progressive CV experiments as the Ru electrode in a 2 mM $CuSO_4$/0.5M H_2SO_4 solution. As shown in Figure 2.4-a, a larger charging capacitance background current, ten times that of Ru electrode, is consistent with the conductive hydrous ruthenium oxide formation after anodic polarization. Most interestingly, two distinct Cu UPD and OPD deposition/stripping regions are also observed on the oxidized Ru electrode. The Cu UPD started at 0.15 V on oxidized Ru electrode surface and extended slightly past 0 V. The Cu UPD coverage grows with the increasing cathodic potentials and reaches a constant plateau of ca. 0.9 ML beyond – 0.05 V, see inset of Figure 2.4-a. Figure 2.4-b shows physical structure of Cu deposition (Cu UPD and Cu OPD) on the conductive hydrous ruthenium oxide

XPS provides a valuable complementary technique to cyclic voltammetry for revealing the actual surface chemical composition of the electrode after electrochemical treatment.[21] Figure 2.5 shows *ex situ* Cu 2p XPS spectra obtained form the Ru and electrochemically oxidized Ru electrode surfaces after holding at the UPD potential for ten minutes. XPS data confirms that Cu deposited under-potentially on both electrodes. However, the UPD Cu monolayer is mostly oxidized after exposure to air prior to XPS analysis.

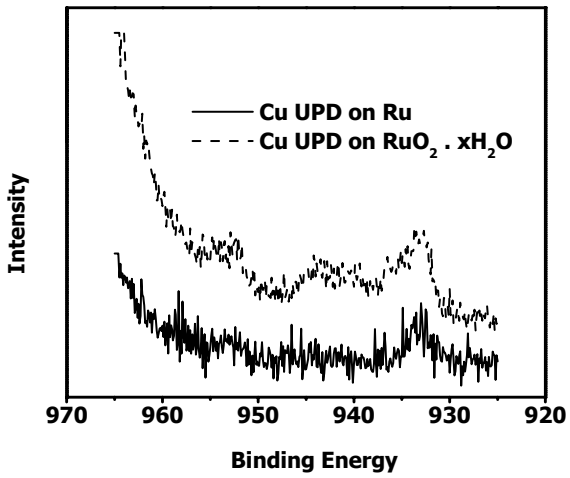

Figure 2.5: XPS spectra (Cu 2p) of Cu UPD on Ru and hydrous ruthenium oxide electrode surface.

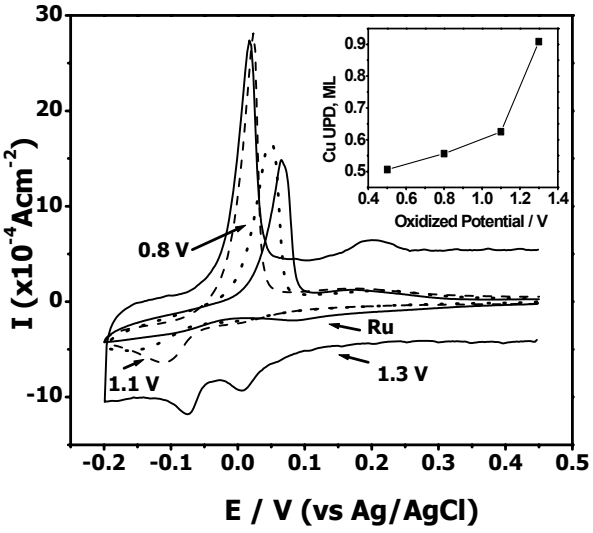

Figure 2.6: CVs collected in a 2 mM $CuSO_4$/0.5M H_2SO_4 solution using different oxidized Ru electrodes prepared by holding at +0.8 , +1.1 and +1.3V for 3 min. A corresponding CV from a freshly prepared Ru electrode is included for comparison.

Effects of varying the oxide-formation potentials on Cu UPD process are shown in Figure 2.6. After each anodic polarization, the oxidized Ru electrode was rinsed with water and Cu deposition was carried out in a 2 mM $CuSO_4$/0.5 M H_2SO_4 solution purged by nitrogen. The electrochemical oxide growth process is significantly accelerated when the oxidizing potential is greater than + 1.2 V. One can easily observe dark black oxide formation on Ru electrode and the corresponding CV shows a large increase of double layer charging capacitance. We chose + 1.3 V as the anodic polarization potential for preparing the entire oxidized Ru electrode. More positive anodic potential was not used due to the concern of excess Ru erosion. As the oxidized potential increases from 0.8 V to 1.3 V, both OPD and UPD Cu deposition/stripping peaks become sharper and better defined. In addition, the separation between Cu bulk and UPD stripping peaks grows larger on the Ru electrode oxidized at a more positive potential. Interestingly, the Cu UPD coverage also increases with the polarization potential, Figure 2.6 inset. By holding the potential at + 1.3 V, the effects of anodic polarization time increases are investigated. As illustrated in Figure 2.7, with as short as five second polarization at + 1.3 V, the oxidized Ru electrode already possessed all the CV current peak characteristics as that of the 180 second polarization. This suggests that the anodic polarization potential plays a major role in determining the Cu OPD and UPD characteristics on the oxidized Ru electrode.

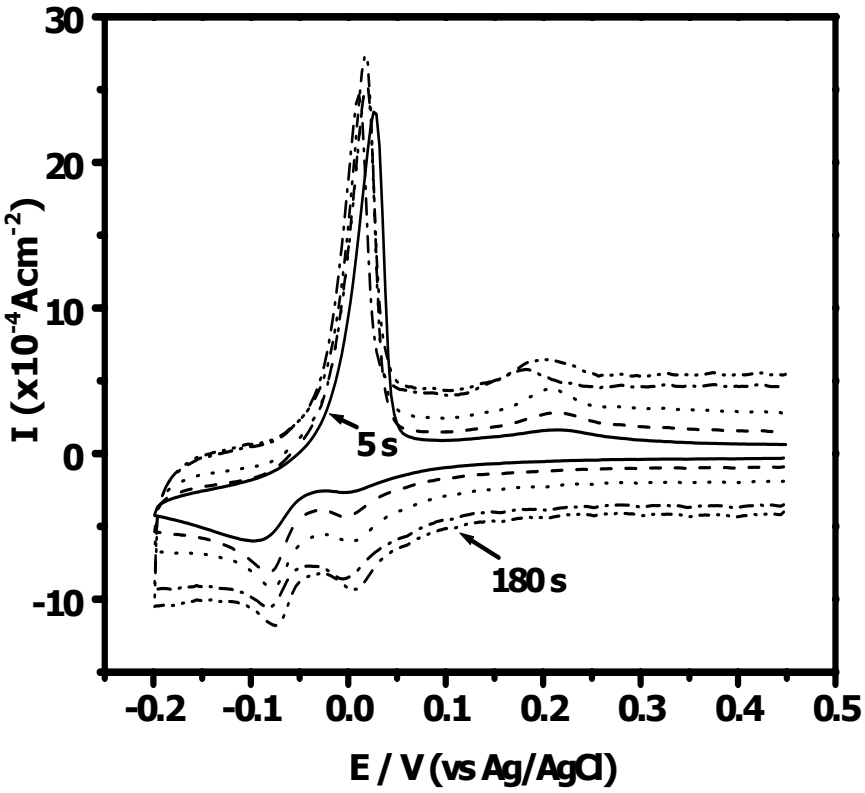

Figure 2.7: Effect of anodic polarization time (hold at +1.3 V) on Cu UPD and OPD. Notice the capacitance CV background increases with anodic polarization time.

Thermally formed RuO_x was investigated and compared with that formed electrochemically. Figure 2.8 is the CV of Ru Oxide (formed at 600 ^{o}C by annealing it under O_2 for 30min) in 2mM $CuSO_4$/0.5 M H_2SO_4 solution. Apparently,

there is a difference between electrochemically formed oxide and thermally formed oxide. There is no UPD Cu on thermal oxide.

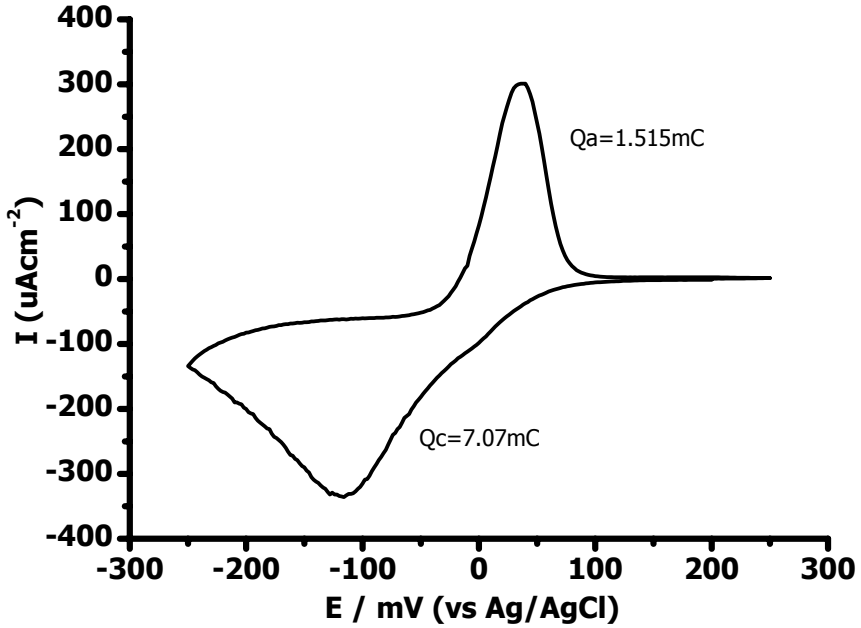

Figure 2.8: Thermal RuO_x behaviors in 2mM $CuSO_4$/0.5M H_2SO_4, Q_c-charge consumed in cathodic Range. Q_a-charge consumed in anodic range (Copyright 2005 by Yibin Zhang).

The deposition efficiency is very low compared to electrochemical oxide. Figure 2.9 shows how annealing affects the Cu plating on an electrochemical Ru Oxide. The Cu UPD disappears gradually (250 ^oC and 400 ^oC), then it comes back when the Ru oxide film is oxidized again electrochemically. If the Ru oxide formed electrochemically was soaked in base (3M NaOH) for ~3min, the Cu UPD will disappear. Work is in progress to further explore the surface chemistry that controls the observed phenomenon.

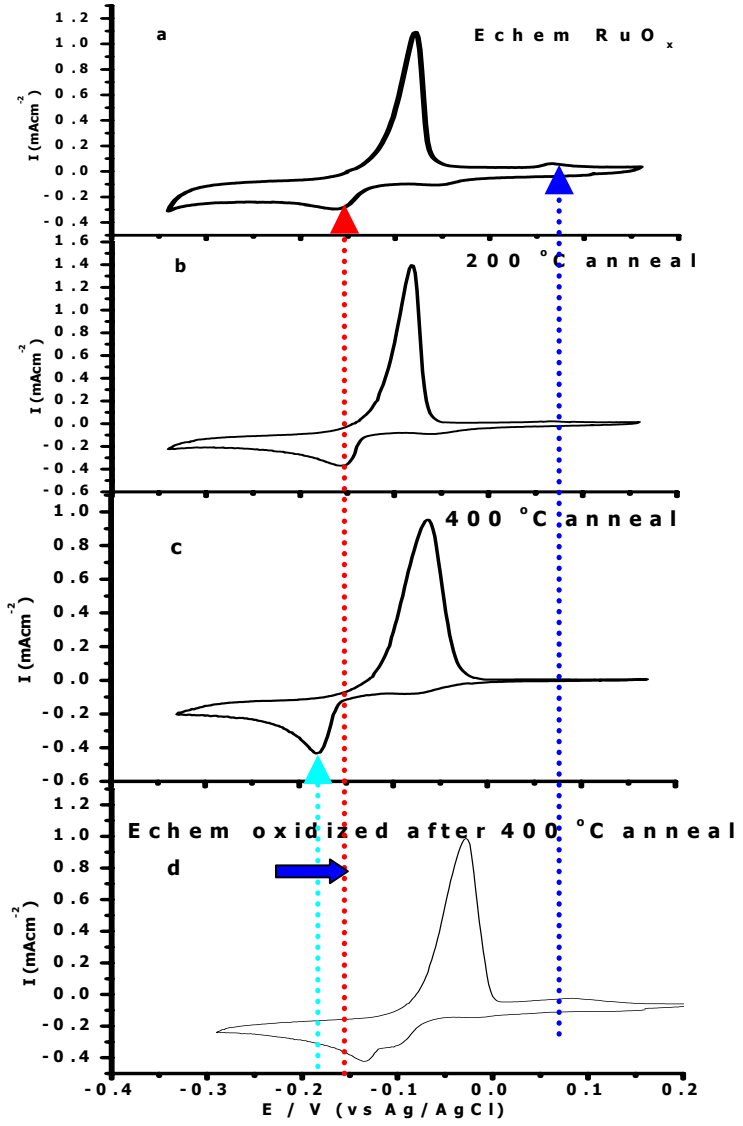

Figure 2.9: CV of Ru oxide formed electrochemically in 2mM $CuSO_4$/0.5M H_2SO_4 a) Ru oxide by CA 1.3V for 3min; b) anneal Ru oxide of a for 10min under N_2 at 200 ^oC; c) anneal Ru oxide of b for 10min under N_2 at 400 ^oC; d) Echem oxidizing Ru oxide of c for 3min by CA in 0.5M H_2SO_4 (Copyright 2005 by Yibin Zhang).

Figure 2.10 and Figure 2.11 show how pH of solution affects the Ru oxide behavior. The pH will greatly affect the Ru oxide behavior. With increasing the pH of the solution, the anodic peak around – 60mV visually disappears, so does UPD Cu.

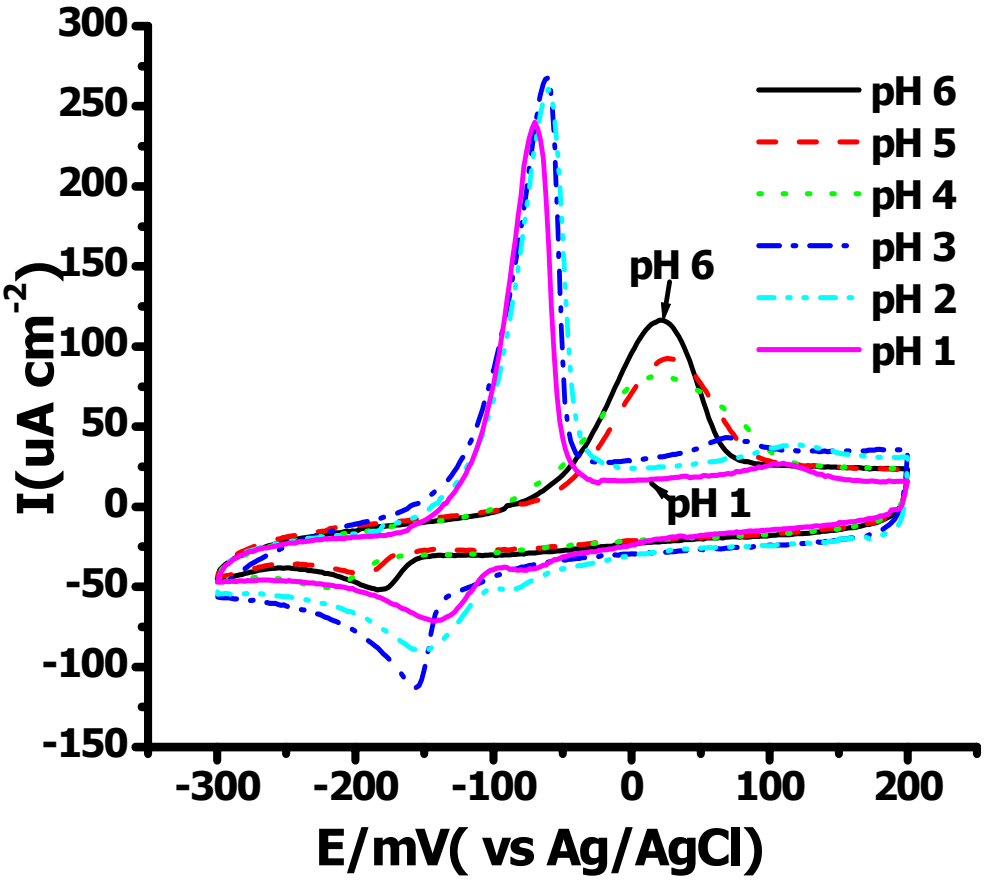

Figure 2.10: pH dependent experiment on RuO_x, which was formed electrochemically. CVs were collected in 2mM $CuSO_4$/0.1 M K_2SO_4 in pH 1, 2, 3, 4, 5 and 6 solution (Copyright 2005 by Yibin Zhang).

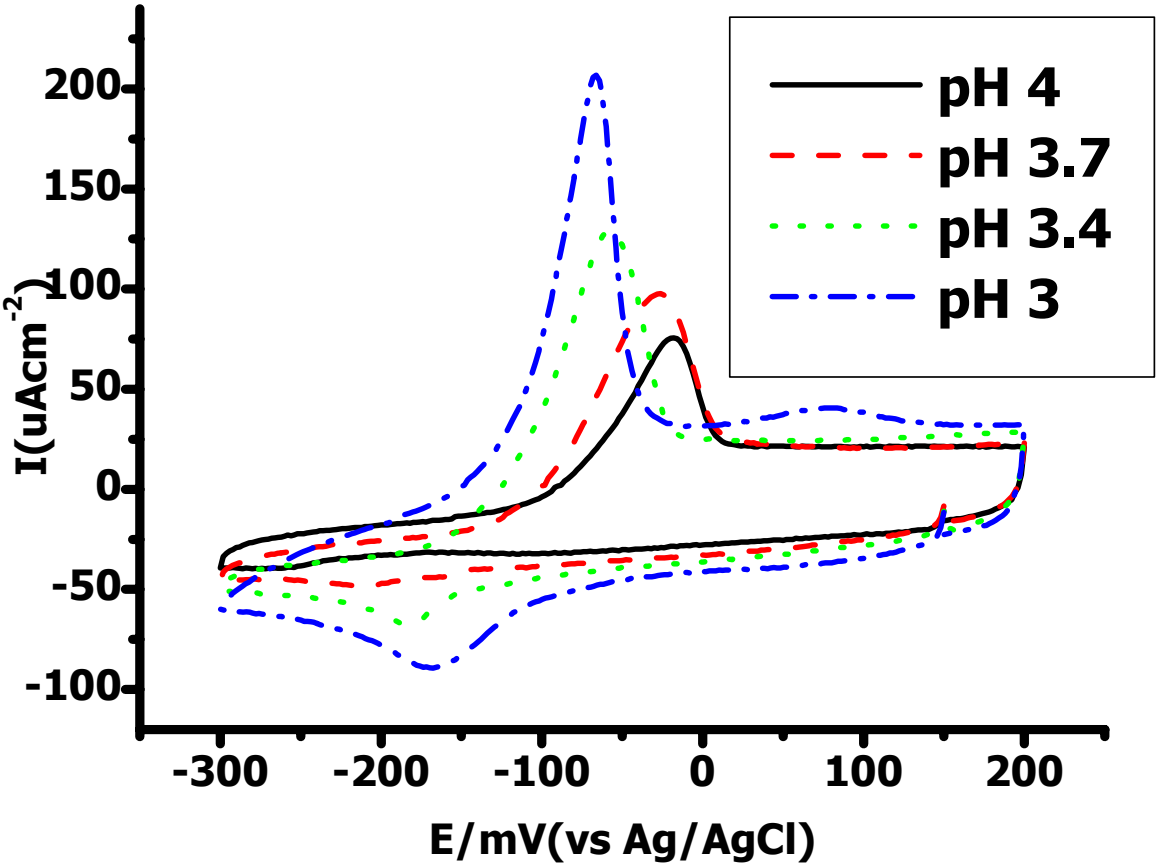

Figure 2.11: pH dependent experiment on RuO_x, which was formed electrochemically. CVs were collected in 2mM $CuSO_4$/0.1 M K_2SO_4 in pH 3, 3.4, 3.7 and 4 solution(Copyright 2005 by Yibin Zhang).

A big anodic peak at about 20mV shows up when pH of solution reaches 4. It keeps increasing from pH 4 to 6, as shown in figure 2.10. The Cl^- ion effect was also studied and shown in Figure 2.12. One can see the bulk Cu decreases with

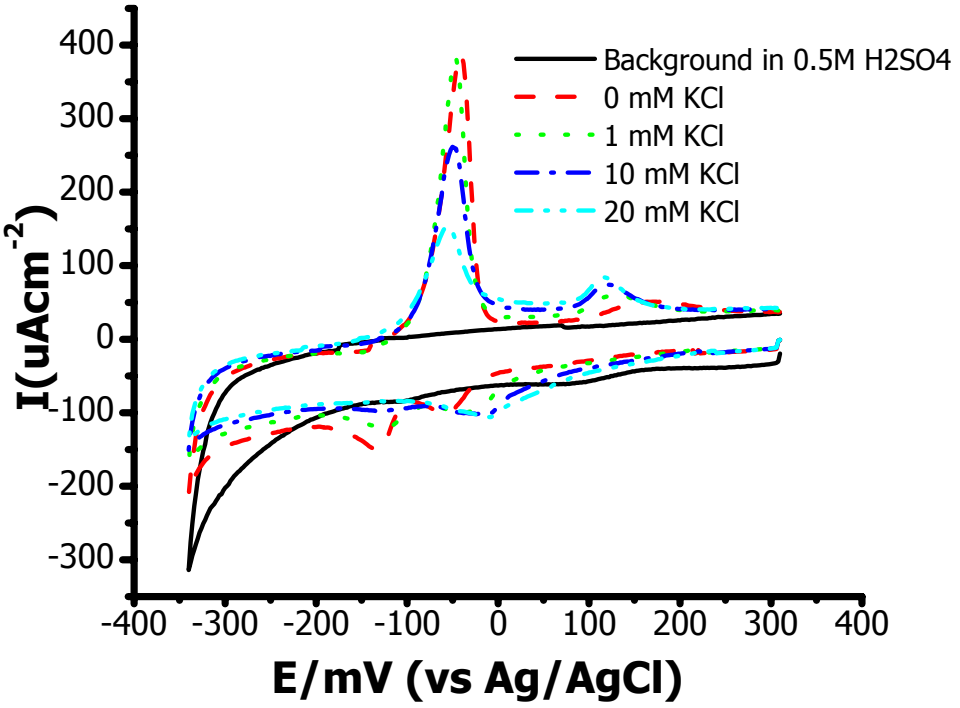

Figure 2.12: Cl^- effect on Cu UPD on RuOx formed electrochemically.

the concentration of Cl^- increasing, and the Cu UPD is un-affected mostly. UPD stripping peak shifts to negative with increasing the Cl^- concentration(Copyright 2005 by Yibin Zhang).

2.4 Discussion

2.4.1 Cu UPD on Ru and RuO_x

Ertl et al. previously reported that Cu forms a bi-dimensional monolayer and follows the hexagonal symmetry of Ru metal substrate before the bulk deposition process begins.[22] Kolb and Gerischer have shown that the underpotential shift ($\Delta E_p = E_{bulk} - E_{UPD}$) observed in UPD monolayer deposition corresponds thermodynamically to the difference in binding energies between a metal adatom to a foreign substrate and the metal adatom to its own lattice.[23] Based on underpotential shift obtained from anodic stripping scan (cf. Figure 2.2), ΔE_p = 110 mV, the first UPD Cu monolayer deposition is more stable by 21 kJ mol^{-1} than subsequent Cu multilayer deposit on Ru. The energetic gain of Cu UPD with respect to Cu OPD is close to the previously reported value of 27 kJ /mol [24]

Several experimental observations support that UPD Cu deposition also takes place on the electrochemically oxidized Ru electrode surface. As shown in Figure 2.4, the progressive CVs reveal that Cu UPD starts before the equilibrium Nernst potential for Cu/Cu^{2+} and is clearly separated from the potential of OPD bulk Cu deposition. That correlates well with the expected energetic gain of a Cu UPD process. Holding at the Cu UPD potential region, we observe that the obtained Cu coverage increases with time and inevitably reaches a constant sub-monolayer value. In addition, the increase of $[Cu^{2+}]$ did not cause significant change of Cu UPD coverage on both Ru and oxidized Ru electrodes. These observations are consistent with the surface-limiting nature of UPD process.

Furthermore the peak potentials of Cu bulk and UPD peaks did shift positively as expected when [Cu^{2+}] increases from 1 to 10 mM. Effect of scanning rate to Cu UPD is also studied. The Cu UPD deposition/stripping peaks are clearly visible on Ru and oxidized electrode surfaces up to 800 mV/sec. XPS characterization, Figure 2.5, after holding in 2 mM $CuSO_4$/0.5M H_2SO_4 solution at the Cu UPD potential provides a direct proof of Cu UPD deposits on the electrochemical oxidized Ru electrode surface.

Contrary to the general perception of metal oxides as insulating or semiconducting materials, the electrochemically prepared hydrous ruthenium oxide, RuO_xH_y, is a known mixed proton-electron conductor.[25] We can obtain well defined reversible CV of $Fe(CN)_6^{-3}$ on as-prepared RuO_xH_y electrode. The electroactive area of RuO_xH_y electrode, estimated from reduction peak current of $Fe(CN)_6^{-3}$, was ca. 1.5 times larger than that of the corresponding Ru electrode before oxidation. The increased surface roughness on RuO_xH_y electrode is likely the major contributing factor to the higher electroactive activity. It is worth noting that the bulk Cu stripping peak current on RuO_xH_y electrode also increases ca. 1.6 times with respect to Ru electrode, comparing Figures 2 & 4. Therefore, the effective Cu UPD coverage, after corrected with the electroactive area increase, is ca. 0.6 ML of Cu on the RuO_xH_y electrode.

The extent of surface oxidation, controlled by the anodic polarization potential, can significantly affect both the Cu OPD and UPD deposition (cf. Figure 2.6). Polarization at potential less than 0.8 V shows similar deposition/stripping

CV as the freshly polished Ru electrode. No observable visual change can be seen on Ru electrode when polarized at potentials less than 0.8 V. After holding at 0.8 V for three minutes, Cu UPD peak on the oxidized Ru electrode shifts more negatively compare to Ru electrode. Van Huong et al reported similar observation and attributed this to the presence of adsorbed oxygenated species on Ru electrode.[19] Quiroz et al. suggest adsorbed O-Ru surface bonding, modified the electron density of adjacent metallic Ru sites to affect the Cu UPD.[20] Our data show no noticeable increase of capacitance background and suggest very thin oxide (or sub-oxide) formation at 0.8 V. At the more positive oxidation potential of 1.3 V, i.e. thick oxide formation, both Cu OPD and UPD deposition/stripping peaks become sharper and better defined. Furthermore, the ΔEp increases to 170 mV (ΔG = 33 kJ mol^{-1}) on the RuO_xH_y electrode. The results suggest that the interfacial structure has changed and the binding of first monolayer of Cu on RuO_xH_y is stronger than Ru by 12 kJ mol^{-1}.

Kolb and Gerischer previously showed *empirically* that ΔEp is proportional to the difference in work functions ($\Delta\Phi$) between monolayer and polycrystalline substrate: [23]

$$\Delta E\text{p} = 0.5\ \Delta\Phi$$

The adsorption of oxygen on the Ru electrode surface is highly favorable due to the abundant unpaired *d*-electrons of Ru metal. The strongly chemisorbed surface oxide species will modify the Ru substrate electronic structure and directly affect its work function. Somorjai *et al.* showed that the sign and

magnitude of $\Delta\Phi$ depends essentially on the donor-acceptor properties of the chemisorption bonding pair.[26] That is, if the electron transfer takes place from the substrate (i.e. Ru) to the absorbed species (i.e. O bearing species) the work function will increase, consequently producing larger ΔE_p . Our UPD data corroborate with this argument. We observe close to 60% increase of ΔE_p for Cu UPD on RuO_xH_y in comparison to metallic Ru surface. In addition, Hartmann *et al.* have reported the measured work functions of Ru and RuO_2, using photoelectron spectroscopy techniques, are *ca.* 4.6 and 5.0 eV respectively. [27]

The interaction of Cu with RuO_xH_y electrode surface is mainly determined by the anodic polarization potential and less influenced by the oxide thickness (cf. Figures 2.6, 2.7). For instance, Ru electrode after a brief 5 seconds +1.3 V oxidation treatment already exhibits all the Cu UPD and OPD CV characteristics as the much thicker RuO_xH_y electrode prepared with full 3 minutes oxidation (cf. Figure 2.7). The oxide thickness can be inferred from the magnitude of double layer charging capacitance background. The data in Figures 2.6 & 2.7 imply that the variation of surface-oxide chemical states, controlled by oxidation potential, has a major influence on the progression of Cu UPD and bulk deposition. The *ex situ* XPS characterization data (not included) also confirm that Ru $3d_{5/2}$ peak shifts progressively toward higher binding energy with increasing positive oxidation potential used to prepare oxidized Ru film. Therefore, a proper chemical composition of RuO_xH_y film is needed to observe Cu UPD. In addition to stoichiometric requirement, there may also exist certain phases or domains,

formed only at the more positive oxidation potential, that are responsible for the favorable Cu UPD deposition. Grazing angle x-ray diffraction measurements show no discernible phases from the RuO_xH_y electrode. Interestingly, Dmowski et al. recently demonstrated, utilizing X-ray diffraction and atomic pair density function, that hydrous ruthenium oxide consists of rutile-like RuO_2 nanocrystals dispersed within the "amorphous" RuO_xH_y matrix.[23] We speculate that the Cu UPD may be operating collectively on the small nanocrystals domains which can not be detected by the common x-ray diffraction measurement. It will be interesting to further study the correlation between the dispersed RuO_2 nanocrystals and Cu UPD process on the RuO_xH_y electrode.

2.4.2 Cl^- Anion Effect on Cu UPD on Echem RuO_x

We found the Cu UPD and OPD will be affected by Cl^- as shown in figure 2.12. With increasing Cl^- concentration, the bulk Cu obviously decreases from first anodic peak. Also, the position of UPD and stripping peak of UPD Cu shifted the former to higher potential and the latter to lower potential. Because the Cu co-adsorbed with chloride forms a bi-layer in which copper atoms are absorbed on the Ru oxide and the Cl^- are on the top layer. The reason for Cu deposition decreases on Ru oxide in Cl^- anions solution is that the Cl^- anions absorbed on the surface are neutral atoms, but SO_4^{2-} exists as ion with charge. So in cathodic region, Cl^- will consume electron in competition with Cu^{2+} reduction, then cause less Cu deposit on the surface in Cl^- solution. The observed phenomenon is in good agreement with what literature reported on Au (111) electrode.[28, 29] Also in

Figure 2.12, the UPD Cu is shifted to a more positive position with increasing Cl^- concentration, Cl^- makes the UPD Cu deposition easier. This is consistent with the observation of literature.[30]

2.4.3 pH Effect on Cu UPD on Ru Oxide Formed Electrochemically

The pH effect on UPD formation on Ru oxide formed electrochemically was investigated as show in Figure 2.10 and Figure 2.11. We found in pH $\leq$3 solutions, the CV shape has no change, the behavior of Ru oxide is the same, and UPD still shows up. In the pH $\geq$4 solutions, the CV shape has a sharp change. With increasing pH value of the Cu plating bath, the reduction peak keeps moving negatively. The bulk Cu stripping peak in anodic peak disappears instead of another anodic peak at more positive potential. Obviously, it is not from the anodic stripping of UPD Cu. Since, the Cu UPD disappears, as shown in figure 2.10. A more clear changing process was observed when working in the pH range from 3 to 4 as shown in Figure 2.11. The data suggested the mechanism of the RuO_x in high pH solution is very different from that in low pH bath. The observed difference could be caused by Oxygen Reduction Reaction (ORR). As mentioned above, the RuO_x surface is favored for oxygen adsorption. In low pH solution, ORR effect is negligible since there are many protons in the bulk solution. In high pH solution, the pH change will be much more sensitive than low pH solution. Likely, it will lead to a different mechanism to take place around electrode and cause the sharp difference on RuO_x electrode in low pH solution and high pH solution.

2.4.4 Comparison of Echem RuO_x and Thermal RuO_x

Compared to Echem RuO_x, Ru oxide formed thermally (600 ^oC under O_2 for 30min) was study under the same condition. Interestingly, the thermal Ru oxide has no UPD showing up. It is only with bulk Cu deposition with about 30% efficiency. The capacitance is apparently smaller than the Ru oxide formed electrochemically, as shown in the Figure 2.8. We believe that the electrochemical RuOx has a different structure from the thermal RuO_x, and the difference has an important relation with structure water (like RuO_xH_y). Our observation is in agreement with literature.[25] This was convinced by another well designed experiment, as shown in Figure 2.9, We electrochemically oxidized Ru first, then annealed it under certain temperature. We found with increasing the anneal temperature (200 ^oC and 400 ^oC), the UPD become smaller and smaller, eventually when temperature reaches 400 ^oC, the UPD completely disappears. At the same time, the capacitance visually decreases significantly. If we electrochemically oxidized the electrode again, the UPD will come back, but the film was peeled off from the side. So, we think the hydrate Ru oxide, formed electrochemically, has the UPD phenomenon, not on the dry thermal Ru oxide.

2.4.5 Effect of Echem RuO_x on Bulk Cu Deposition

Another interesting point we found in 50mM $CuSO_4$ and 0.5M H_2SO_4 is that the Cu deposition is thermodynamically favored on RuO_x (formed electrochemically). As shown in Figure 2.13, Cu deposition peak moves in a positive direction when we increase the oxidizing potential, the efficiency is over 90%. There is 182 mV

shifting from Ru to RuOx formed at 1.3V. Results are summarized in the table 2.1. Actually this is good news for industry. They can save energy and reduce the cost of production, and they can take advantage of formal UPD Cu on RuO_x to satisfy the requirement of Cu deposition in high-aspect ratio vias or trenches for Cu interconnect microelectronics in the next generation of microelectronics.

The mechanism remains under investigation. We think probably the hydrate RuO_x plays a main role as a catalyst, which reduces the activation energy (here is potential change) of reaction of $Cu^{2+} + 2e^- = Cu$, similar to those Ru complex as catalyst in organic synthesis reported in literature.[31, 32] However, only the hydrate RuOx has this special property. As shown in Figure 2.9-c, after it was dehydrated by annealing at 400 ^oC, the catalyst function was gone, and the Cu deposition shift to more negative potential. The interesting point is, after electrochemically oxidizing it again, the Cu reduction peak has a trend

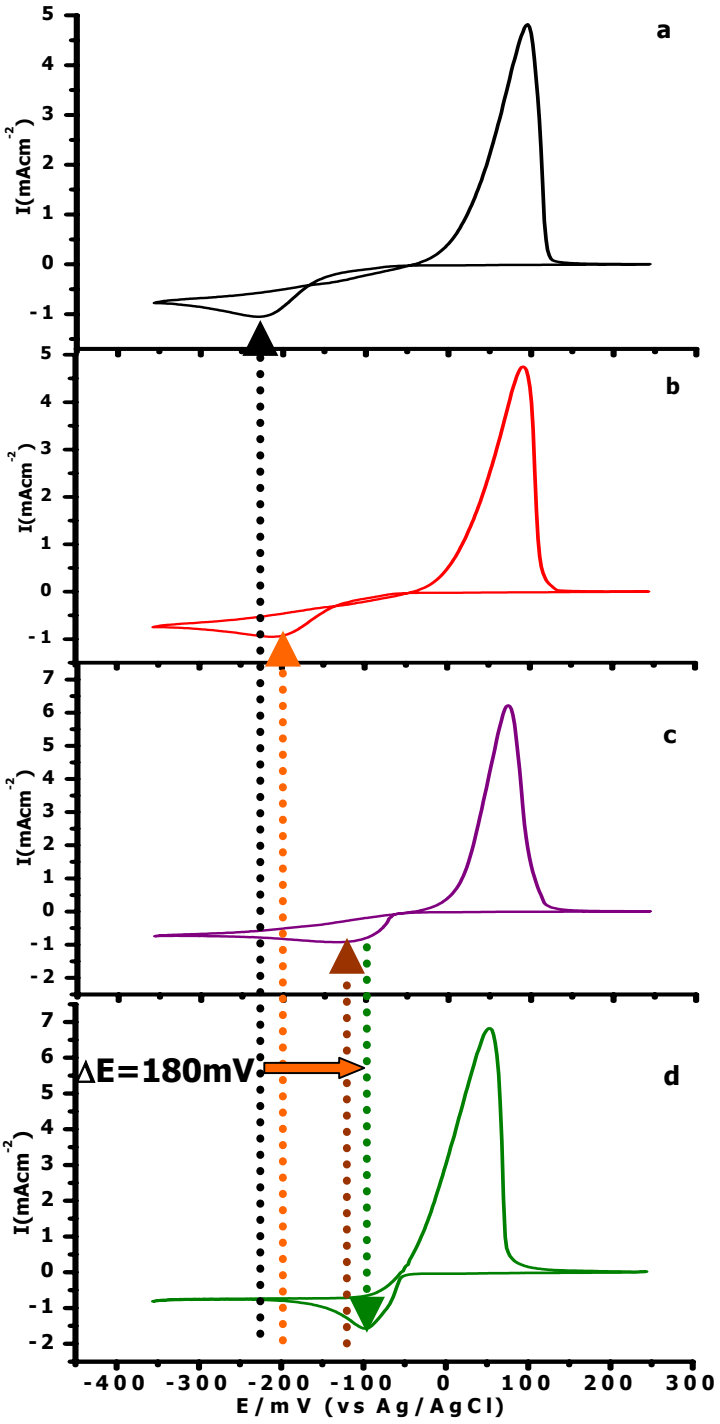

Figure 2.13: CVs of RuOx in 50mM $CuSO_4$/0.5MH_2SO_4, a) is Ru metal. RuOx was formed: b) 0.8V 3min; c) 1.2V 3 min; d) 1.3V 3min (Copyright 2005 by Yibin Zhang).

Oxidation potential	E_d V	Q_c mC	Q_a mC	Q_a/Q_c %	$Q_c/Q_{c\text{-}Ru}$	$\Delta E_d = E - E_{bare}$(V)
Bare Ru	-0.28	26.44	24.27	91.78	1.00	0
+0.8V	-0.21	31.89	30.18	94.64	1.21	0.07
+1.1V	-0.14	36.73	34.89	94.96	1.39	0.14
+1.3V	-0.10	48.46	45.29	94.95	1.83	0.18

Table 2.1: Summary of Cu deposition in 50mM $CuSO_4$/0.5M H_2SO_4 on Ru oxide formed at 0.8V, 1.1V, 1.2V and 1.3 V for 3 min polarization in 0.5MH_2SO_4, E_d- Cu reduction peak position, Q_c- charge of reduction peak (cathodic), Q_a –charge of oxidation peak (anodic), ΔEd-the difference of Cu reduction peak between Ru oxide and Ru metal (Copyright 2005 by Yibin Zhang).

to shift back the potential before annealing at 400 ^oC toward positive potential. Swider and coworker reported hydrous ruthenium oxide ($RuO_2 \cdot \chi H_2O$ or RuO_xH_y) is a mixed electron-proton conductor with a specific capacitance. [25] The structure water in hydrous RuO_x is necessary for charge storage; we also believe the structure water in hydrous RuO_x is necessary for thermodynamically favored Cu deposition on RuO_x formed electrochemically.

2.5 Summary

Cu UPD on the RuO_x formed electrochemically was observed. The pH, Cl^- anion effect on Cu UPD was studied. Considerable difference of electrochemical Ru oxide and thermal Ru oxide was observed. Cu deposition is thermodynamically favored on Ru oxide formed electrochemically. The observation of Cu UPD on Ru and its conductive oxide surfaces has important implications in the Ru-based Cu diffusion barrier application. Previously, we have demonstrated that a 20 nm Ru thin film functions well as a Cu-diffusion barrier after 450 C annealing. [18a] However, for the future 45-65 nm integrated circuit devices, the thickness of a functional diffusion barrier is limited to merely 5 nm. In such a ultra-thin non-epitaxial metal film, as demonstrated by Gjostein[33], where grain boundaries and dislocations are abundant and will provide the least energy resistant paths for Cu inter-diffusion. Conceivably, the amorphous conductive ruthenium oxide can be delivered electrochemically to plug the grain boundary diffusion passageways prior to Cu electroplating for maximizing the Ru-based barrier performance. Our current data suggest that both Ru and its conductive oxide easily receive *direct* Cu plating. More importantly, strong binding interaction, manifested by the observed Cu UPD process, exists between Cu and Ru as well as its conductive ruthenium oxide. Our separate scribe and peel tests confirm that stronger interfacial binding does promote excellent Cu adhesion, and that is critical important in order to withstand highly demanding chemical-mechanical planarization process during integrated circuits fabrication.

Therefore, ultra-thin film composed of Ru and its conductive oxides is a promising candidate as a directly plate-able Cu diffusion barrier for the future metal interconnect application.

2.6 References

1) International Technology Roadmap for Semiconductors, *http://public.itrs.net/Reports.htm*; SEMATECH Inc., (**2002**).

2) International Technology Roadmap for Semiconductors, *http://public.itrs.net/Reports.htm*; SEMATECH Inc., (**2003**).

3) Kuzume, Akiyoshi; Herrero, Enrique; Feliu, Juan M.; Nichols, Richard J.; Schiffrin, David J. Centre for Nanoscale Science, Department of Chemistry, the University of Liverpool, Liverpool, UK. *Journal of Electroanalytical Chemistry*, **570**(2), 157 (**2004**).

4) Simkunaite, Dijana; Ivaskevic, Emilija; Jasulaitiene, Vitalija; Kalinicenko, Aleksandras; Valsiunas, Ignas; Steponavicius, Antanas. Institute of Chemistry, Vilnius, *Lithuania. Chemija*, **15**(1), 12 (**2004**).

5) Martinez-Ruiz, Alejandro; Palomar-Pardave, Manuel; Valenzuela-Benavides, J.; Farias, Mario H.; Batina, Nikola. Facultad de Ciencias, Universidad Autonoma de Baja California, Ensenada, Mex. *Journal of Physical Chemistry B*, **107**(42), 11660 (**2003**).

6) Zei, M. S. Fritz-Haber Inst., Max-Planck-Gesellschaft, Berlin, Germany. *Zeitschrift fuer Physikalische Chemie* (Munich), **208**(2), 77 (**1999**).

7) a) S. Trasatti, G. Lodi (Eds.), *Electrodes of Conductive Metallic Oxides*, Part A

and Part B, Elsevier, Amsterdam,**1980** and **1981**. b) S. Trasatti, *Electrochemical Hydrogen Technologies*, Elsevier, Amsterdam, **104**, 1 (**1990**).

8) H. Over, *Applied Physics A*, **75**, 37 (**2002**).

9) W.F. Lin, J.M. Jin, P.A. Christensen, K. Scott, *Electrochimica Acta* , **48**,3815 (**2003**).

10) Rao, C.N.R.; Raveau, B.: *"Transition Metal Oxides Structure, Properties, and Synthesis of Ceramic Oxides"*, p 229-254, 2nd ed.; Wiley –VCH: New York.

11) P.C.S. Hayfield, *Plat. Met. Rev*. **42**, 116 (**1998**).

12) B.E. Conway, *Electrochemical Supercapacitors*, Kluwer: Plenum, New York, (**1999**).

13) a) A.S. Arico, G. Monforte, E. Modica, P.L. Antonucci, V. Antonucci, *Electrochemistry Communications,* **2**, 466(**2000**). b) J.P. Popic, M.L. Avramov-Ivic, N.B. Vukovic, *Journal of Electroanalytical Chemistry,* **421***,* 105 (**1997**).

14) N. Matsui, K. Anzai, N. Akamatsu, K. Nakagawa, N. Ikenaga, T. Suzuki, *Applied Catalysis A.*, **179**, 247 (**1999**).

15) L. Zang, H. Kirsch, *Angew. Chem. Int. Ed.* **39**, 3921 **(2000**).

16) a). L. Krusin-Elbaum, M. Wittmer, *J. Electrochem. Soc.* **135**, 2610 (**1988)**. b) T. Maeder, P. Muralt, L. Sagalowicz, M. Setter, *J. Electrochem. Soc.* **146**, 3393 (**1999)**.

17) E. Kolawa, F.C.T. So, E.T. Pan, M.A. Nicolet, *Appl.Phys.Lett.* **50**, 854

(**1987)**.

18) a) O. Chyan, T.N. Arunagiri, T. Ponnuswamy, , *J. Electrochem. Soc.*, 347, 150 (**2003**);

b) R. Chan, R. T.N. Arunagiri, Y. Zhang, O. Chyan, R.M. Wallace, M.J. Kim, *Electrochemical and Solid-State Letters*, **7**(8), G154 (**2004**);

c) Zhang, Yibin; Huang, Long; Arunagiri, Tiruchirapalli N.; Ojeda, Oscar; Flores, Sarah; Chyan, Oliver; Wallace, Robert M. *Electrochemical and Solid-State Letters*, 7(9), C107-C110 (**2004**).

19) N.C. Van Huong, M.J. Gonzalez-Tejera, *J. Electroanal. Chem.* **244**, 249 (**1988**).

20) M.A. Quiroz, Y. Meas, *J. Electroanal. Chem.* **157**, 165 (**1983**).

21) P.M.A. Sherwood, *Surf. Sci.*, **101**, 619 (**1980**).

22) K. Christmann, G. Ertl, H. Shimizu, *J. Catal.* **61**, 397 (**1980**).

23) D.M. Kolb, M. Przasnyski, H. Gerischer, *Electroanal.Chem.and Interfac. Electrochem.* **54**, 25 (**1974**).

24) E.M. Stuve, J.W. Rogers Jr., D. Ingersoll, D.W. Goodman, M.L. Thomas, *Chem. Phys. Letters.***149**, 557 (**1988**).

25) a) K.E. Swider, C.I. Merzbacher, P.L. Hagans, D.R. Rolison, *Chem, Mater.* **9**, 1248 (**1997**); b). D.A. McKeown, P.L. Hagans, L.P.L. Carette, A.E. Russell, K.E. Swider, D.R. Rolison, *J. Phys. Chem. B*, **103**, 4825 (**1999**).

26) G.A. Somorjai, *"Principles of Surface Chemistry"*, Prentice Hall: Englewood Cliffs, NJ, (**1972**).

27) A. J. Hartmann, M. Neilson, M. R. N. Lamb, K. Watanabe, and J. F. Scott, *Appl. Phys. A: Mater. Sci. Process,* **70**, 239 (**2000**).

28) Zhichao Shi, Shujie Wu and Jack Licek Lipkowski, *Electrochimica Acta*. **40** (1), 915 (**1995**).

29) D. M Kolb, Z. *Phys. Chem*. N. F. **154**, 179 (**1987**).

30) W. Dmowski, T. Egami, K.E. Swider-Lyons, C.T. Love, D.R. Rolison, *J. Phys. Chem. B.* **106**, 12677 (**2002**).

31) Duan-Ming Tan and Kin Shing Chan, *Tetrahedron Letters,* **46** (3), 503 (**2005**).

32) Ricardo Martínez, Gabriel J. Brand, Diego J. Ramón and Miguel Yus *Tetrahedron Letters,* **46** (21), 3683 (**2005**).

33) N.A. Gjostein, *"Diffusion"* , American Society for Metals; Metals Park, Ohio, (**1973**).

CHAPTER 3

STUDY ULTRA-THIN RU FILM BEHAVIOR AS CU DIFFUSION BARRIER IN THE STACK OF CU/RU/SI

3.1 Introduction

The largest driving force for recent development of new material for a Cu diffusion barrier is the need for ultrathin films with stable, scalable, Cu direct platable properties, because the size of gate oxide length will be shrunk to 45nm for the next generation of microelectronics.[1,2] As device dimensions are scaled down, Cu becomes the best choice as an interconnect material due to its higher electromigration (EM) resistance, and thus reliability, as well as lower resistivity (1.67 μ Ω .cm) compared to Al (2.69 μ Ω .cm) wiring. However, Cu has higher diffusivity and easily diffuses through dielectrics. [3,4] Thus, a thin, stable diffusion barrier is an essential requirement for Cu interconnect technology in integrated circuit (IC) Industry. Especially, for the next generation microelectronics, the anode will shrink to ~45 nm, and the diffusion barrier will step into ~5nm range. The current Ta/TaN diffusion barrier/liner for Cu interconnects will encounter scaling difficulties at the 45 nm node since Ta is too easily oxidized to receive Cu plating on the more resistive Ta/TaN.[5]. A Cu-seeding layer must be deposited over it to assure a good Cu electrofill. To maintain a low effective interconnect resistivity (ρ=2.2 μ Ω .cm), an ultra-thin diffusion barrier (~ 5 nm) is needed to

scale the next generation integrated circuit technology for 45 nm node.[6] Ruthenium (Ru) is an air-stable transition metal with nearly twice the electrical conductivity of Ta (Ru bulk resistivity ρ=7.1 μ Ω .cm vs. ρ=13 μ Ω .cm for Ta). Especially, like Ta, Ru shows negligible solubility with Cu even at 900 °C.[7] Recently, Ru obtained attractive attention as a Cu-plate-able diffusion barrier.[8-11] Lane, et al. proposed a family of liner materials based on the relative oxide stability in the acidic Cu plating condition.[8] Conformal electroplating is very important for Cu plating in high-aspect-ratio via or trenches.[12] We have recently reported that Ru is an excellent substrate for conformal Cu electroplating.[9a] The inherently favorable interfacial bonding manifests itself in strong adhesion between the electroplated Cu and the Ru substrate even when it was annealed over 600 ^{o}C.[9] Josell et al. studied seedless superfilling of Ru fine trenches by direct cop per plating.[10] A study of scaling limits of ultra thin Ru films prepared by the low-temperature chemical vapor deposition was recently reported.[11]

Electrochemical Cu plating is very attractive due to its low cost, low process temperature, and good ability to fill vias compare to PVD and CVD.[6] It was reported that Ru is directly electroplate-able with Cu and forms a conducting oxide. [9a, 9c] Cu underpotential deposition was demonstrated on both Ru and Ru oxide surfaces. It was also reported the direct plate-ability of Cu on ultra-thin Ru films (5 nm to 20 nm) with over 95% efficiency.[9b, 13] However, implementing Cu electroplating on a 5 nm Ru deposited on 300 mm patterned wafer remains a technological challenge due to the large resistivity increase across a wide plating

area. While PVD of Cu is independent of the resistivity of its substrate, the efficiency of ECD of Cu is determined by the rate of the heterogeneous electron transfer process (e.g. $Cu^{2+}(aq.) + 2e^{-} = Cu(s)$) occurring across the ultra-thin Ru substrate/copper acid bath interface. A large iR drop in Cu plating bath will inhibit uniform potential control on Ru surface and consequently lead to poor characteristics of ECD Cu deposits. One approach to circumvent the resistivity hurdle is to pre-deposit a Cu blanket coating by physical vapor deposition (PVD) prior to the ECD back fill process. Therefore, both types of ECD-Cu, PVD-Cu/Ru interfaces could co-exist in the same wafer.

In our previous study, diffusion study results of a Cu/(20 nm Ru)/Si system using secondary ions mass spectroscopy (SIMS) depth-profiling and transmission electron microscopy (TEM) were investigated.[9b] The TEM results corroborated with SIMS profiling data to demonstrate that ~ 20 nm thin Ru film effectively prevents Cu diffusion up to 450°C. In this chapter, interfacial stability of electroplated Cu/ Ru (5nm)/Si structures were investigated, another principal emphasis of this study is comparative investigation of the Cu diffusion process and interfacial phenomena in two different types of structures: ECD Cu/(5 nm Ru) Si and PVD Cu/(5 nm Ru)/Si. TEM, RBS, XPS and Analytical Electron Microscopy (AEM) will be combined to characterize inter-diffusion results of a Cu overlayer directly electroplated on a ~ 5 nm Ru film supported by a Si (100) substrate. The quality of the Ru films prepared by MS sputtering system will be characterized by XPS and TEM. High-resolution AEM reveals an interlayer growth

between Ru and its underlying Si substrate. Interfacial characterization studies were performed on PVD Cu/(5 nm Ru)/Si and ECD Cu/(5 nm Ru)/Si structures using TEM along with optical imaging and four point sheet resistivity measurements. Backside SIMS depth profiling analyses were conducted to probe the interfacial profiles of as-deposited and annealed Cu/(5 nm Ru)/Si structures and compared to TEM results. A series of XPS experiments were carefully designed to investigate the behavior of both PVD and ECD Cu in Cu diffusion study, the difference was observed and it will be discussed in this chapter.

3.2 Experimental

Ultra thin Ru films were prepared on a pre-cleaned HF etched Si wafer by using a standard DC magnetron sputtering tool at a chamber pressure of 20 mTorr and Ar flow rate of 10 sccm. The base pressure was 1×10^{-8} Torr. HRTEM was used for measuring the thickness of the as-deposited Ru film and also for analyzing pre and post-annealed Cu/(5 nm Ru)/Si structures. A Philips CM200FEG TEM was employed. PVD Cu films were thermally evaporated in a JEOL-JEE-4X evaporator at a base pressure of $< 7 \times 10^{-7}$ Torr. Subsequent high-resolution AEM analysis was carried out using a JEOL JEM 2010 equipped with energy dispersive X-ray (EDX) and electron energy-loss spectroscopy (EELS) for elemental analysis of sub-nanometer. ECD Cu was done from high purity $CuSO_4.5H_2O$ (Aldrich) with H_2SO_4 (Mallinckrodt) as supporting electrolyte made using ultra pure water ($R > 18.2$ MΩ, Millipore), and was performed on CHI 440 (CH Instruments Inc.) and M273 (EG&G, Princeton Applied Research)

potentiostat/galvanostats. A conventional three-electrode electrochemical set-up with Pt sheet as counter electrode, Ag/AgCl (3 M NaCl) as reference electrode was used. They are the same as the procedures in our previous report.[9a, 9b]

Annealing was done in an evacuated quartz tube (< 1 x 10^{-6} Torr). Optical images were obtained using a Nikon ME600L microscope. SIMS analyses from the backside of the Cu/(5 nm Ru)/Si structures were performed in a Cameca 6f spectrometer. Prior to the SIMS analysis, the Si back substrate in Cu/(5 nm Ru)/Si samples were mechanically polished down to within 1 – 2 μm. XPS data were collected using a VG ESCALAB MKII spectrometer (Thermo VG Scientific) with an Al K_α excitation sources

3.3 Results

The thickness was controlled by supplied power and the deposition time, and it was calibrated by RBS. The quality of the Ru thin films was characterized by XPS. Figure 3.1 show the XPS data of some films of Ru (2.5nm, 5nm, 10nm), Figure 3.1-a is O 1s, Figure 3.1-b is Ru 3d and Figure 3.1-c is Si 2p. For the 5nm and 10nm Ru film, the XPS spectrum shows that there is a little Ru oxide on the surface. Ar^+ sputtering was used to characterize the underneath layer of the 5nm Ru/Si, as shown in Figure 3.2. With increasing the Ar^+ sputtering time, the top layers were removed. O1s (529.7 eV), which comes from Ru oxide, disappears at last, and only the adsorption oxygen (~ 532 eV) was left. To check the thermal stability of the stack of Ru/Si, 5nm Ru/Si was annealed with N_2 purging. XPS spectrum with resolved angle was collected, as shown in Figure 3.3.

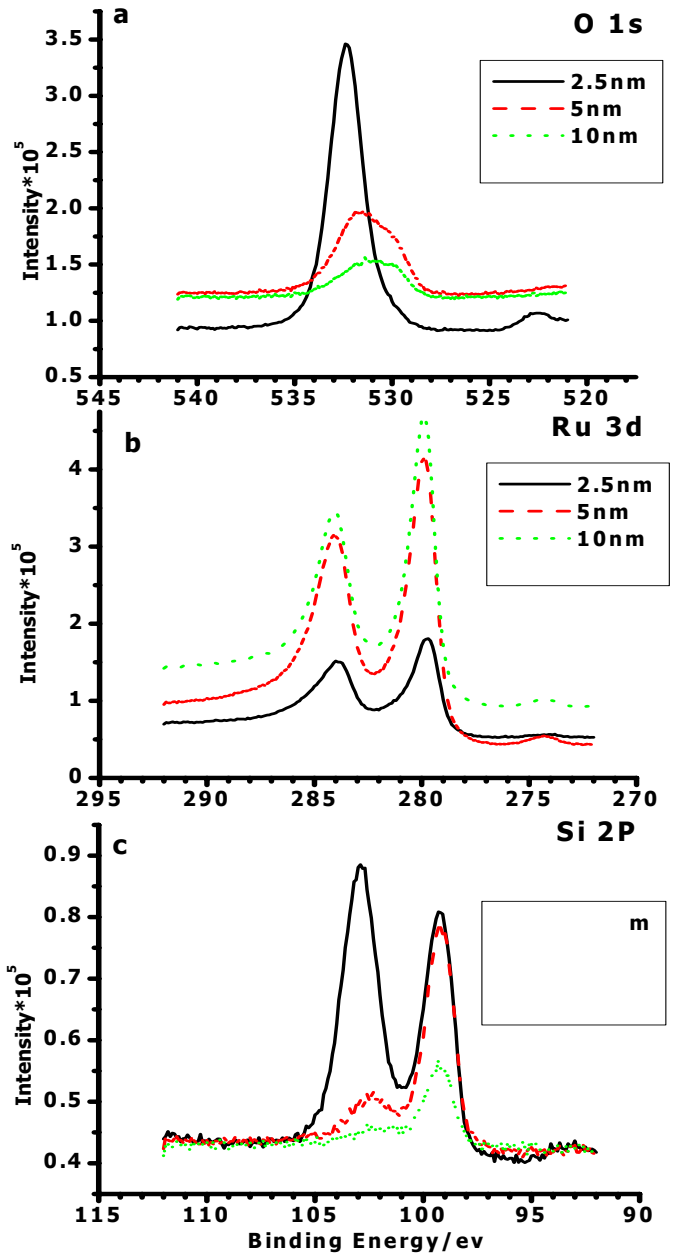

Figure 3.1 XPS spectrum of Ru thin films a) O 1s; b) Ru 3d; c) Si 2p.

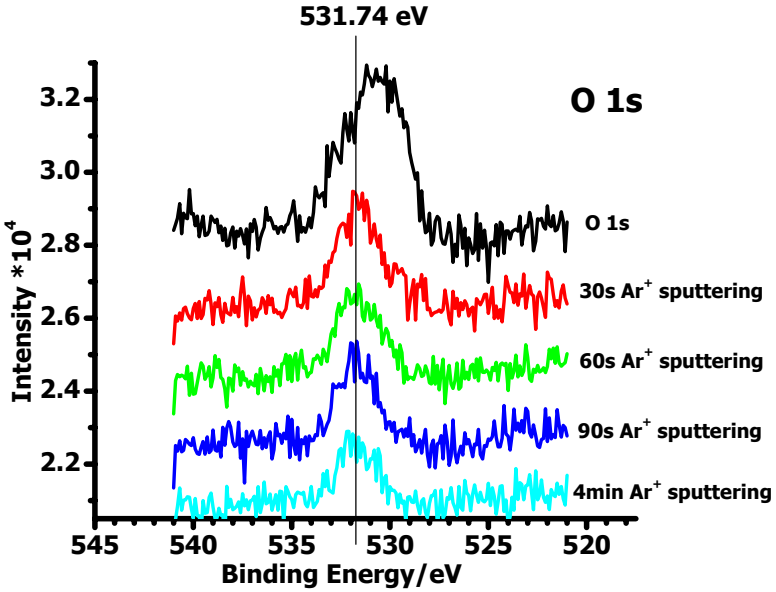

Figure 3.2: XPS spectrum of O 1s by Ar^+ sputtering on 5nm Ru/Si.

Obviously, there is some Ru oxide form on the sample. To get depth profile information, the XPS spectrum was collected from a sputtered sample. The spectrum shows that the Ru oxide was formed just on the surface of bulk Ru, underneath Ru is still Ru metal, as shown in Figure 3.4.

PVD and ECD Cu/Ru (5nm)/Si was characterized by XPS (Figure 3.5 a and b)) and TEM (Figure 3.6 - a, c, e and g), The XPS and TEM data shows that both PVD and ECD Cu produce good quality Cu metal, Cu $2p_{3/2}$=932.2 eV. The thickness of the Ru is ~5nm based on TEM image (Figure 3.7).

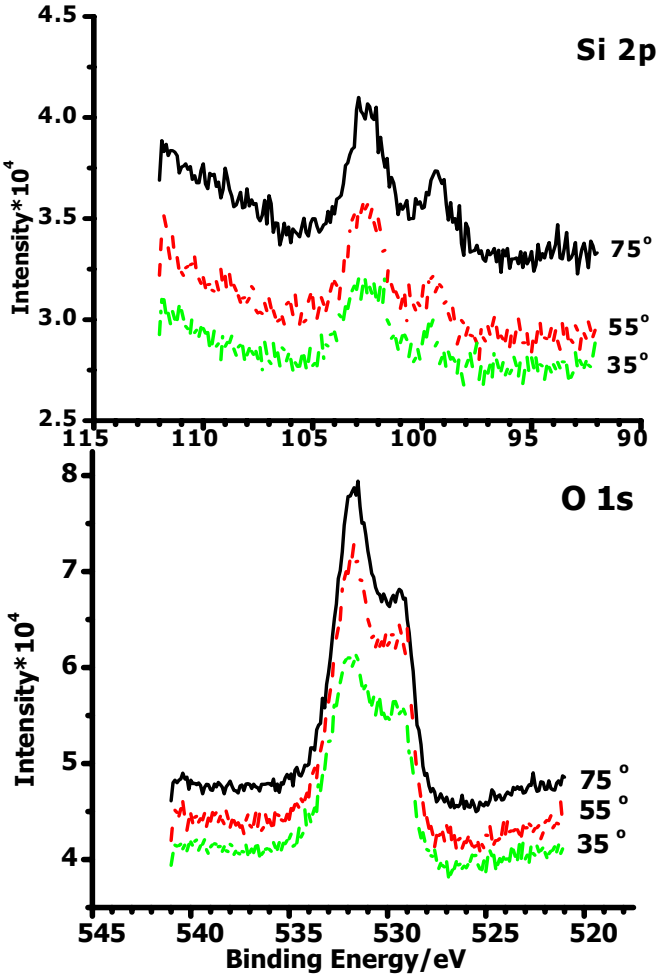

Figure 3.3: XPS spectrum of Si 2p and O 1s in resolved angle on 5nm Ru/Si annealed at 350 ^{o}C with N_2 purge.

We designed an analytical scheme (Figure 3.8) involving XPS analyses before and after etching removal of Cu overlayer using concentrated HNO_3. The non-annealed Cu/(5 nm Ru)/Si samples were subjected to XPS monitoring after

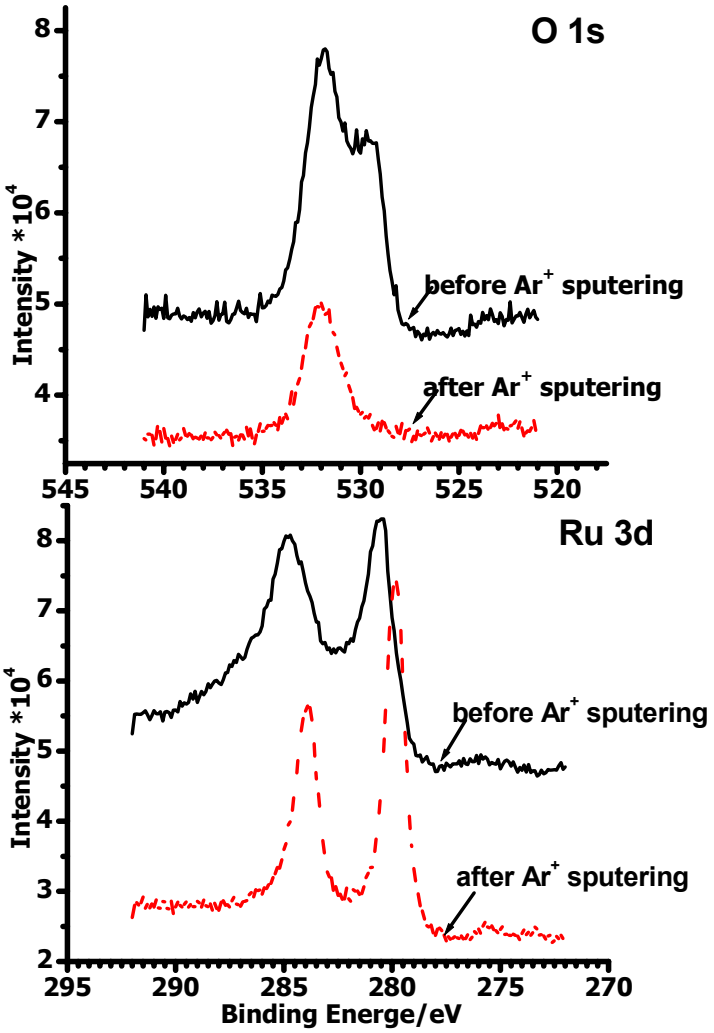

Figure 3.4: XPS spectrum after Ar^+ sputtering on 5nm Ru/Si annealed at 350 ^oC with N_2 purge.

repeated HNO_3 etching lasting for up to 20 min. XPS spectra from all test samples showed no Cu after 5 minutes of HNO_3 etching. This demonstrated the efficacy of HNO_3 in etching Cu. This experiment was used to investigate Cu

diffusion through Ru, including both PVD Cu and ECD Cu. Because it will be hard to be removed by HNO_3 etching if the Cu diffuses inside of Ru, or even worse, Cu

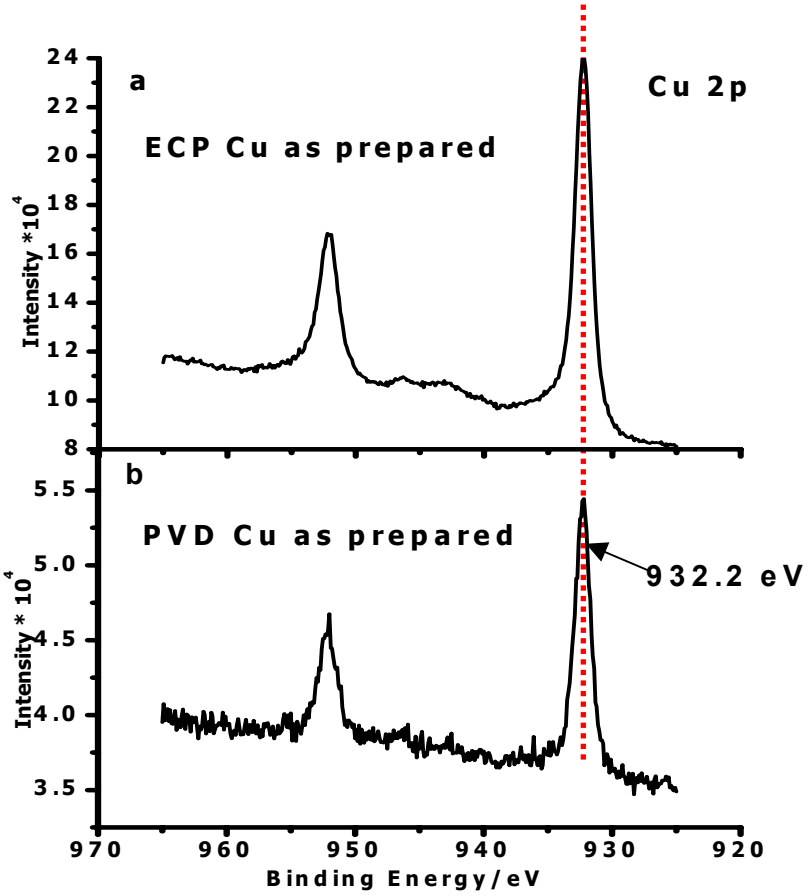

Figure 3.5: XPS spectrum of a) ECP Cu (~70nm)/Ru/Si) as prepared; b) PVD Cu (~70nm)/Ru/Si) as prepared.

completely breaks through Ru film to meet with Si substrate and react with it when annealing Cu/Ru/Si stack under high temperature. The left Cu or Cu silicide can be detected by XPS after HNO_3 etching. Figure 3.9-f is XPS spectrum of Cu 2p collected on PVD Cu/Ru/Si annealed at 450 ^oC in vacuum for 10 min. The peak position of Cu $2p_{3/2}$ changed from 932.2 eV (Cu^0) to 933 eV (Cu silicide).

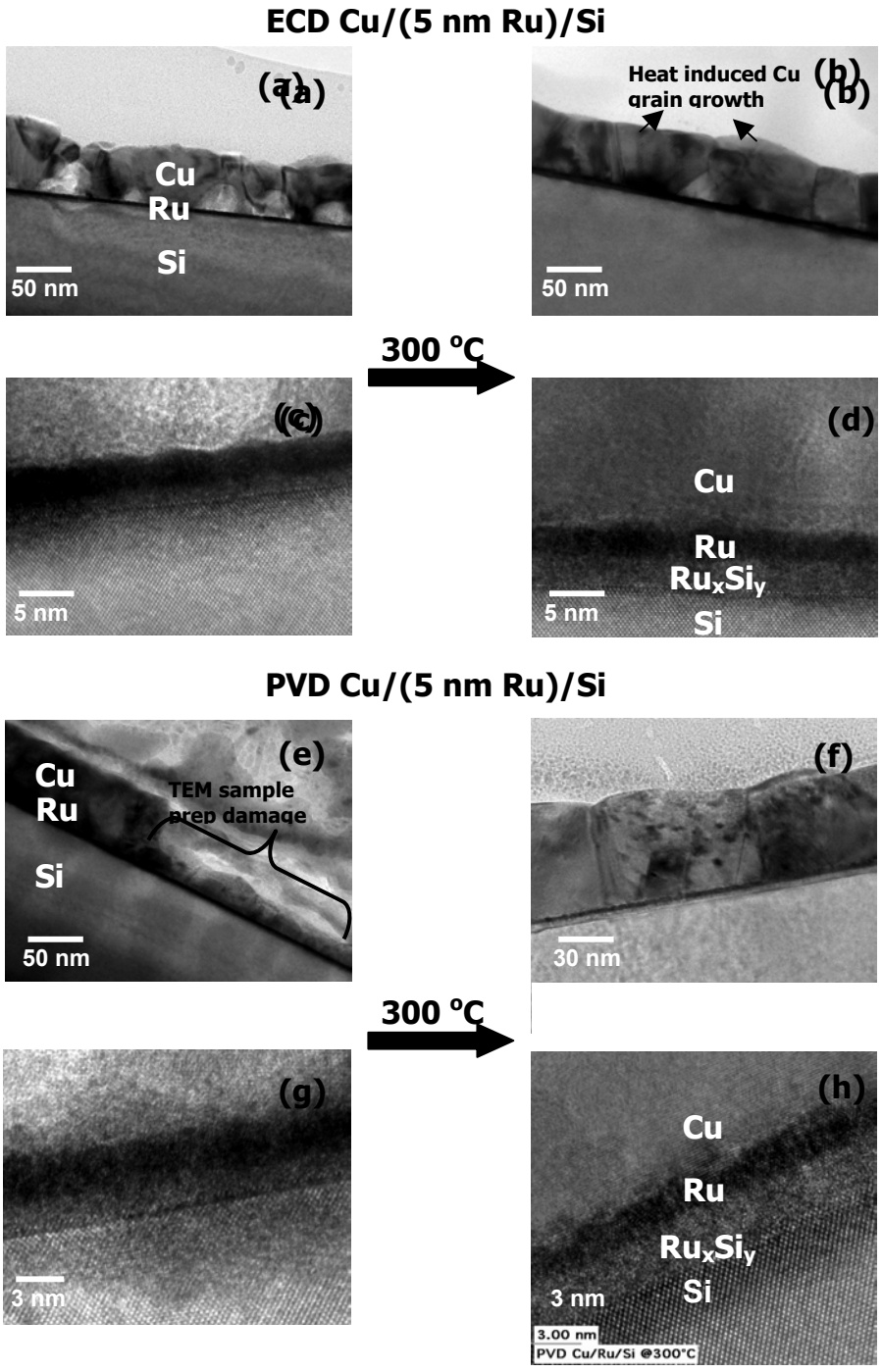

Figure 3.6: TEM images of ECD Cu/(5 nm Ru)/Si (a) & (c) – RT; 300 ^{o}C vacuum annealed for 10 min. – (b) & (d). PVD Cu/(5 nm Ru)/Si at RT (e) & (g) – RT; 300 ^{o}C vacuum annealed for 10 min. – (f) & (h).

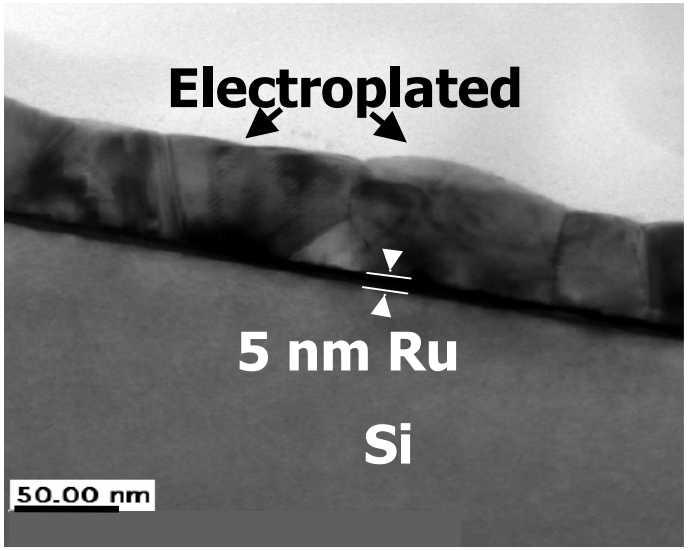

Figure 3.7: TEM image for electroplated -Cu/(5 nm Ru)/Si structure annealed at 300 ^{o}C shows heat-induced Cu grain growth on an intact Ru barrier layer, corroborates RBS data.

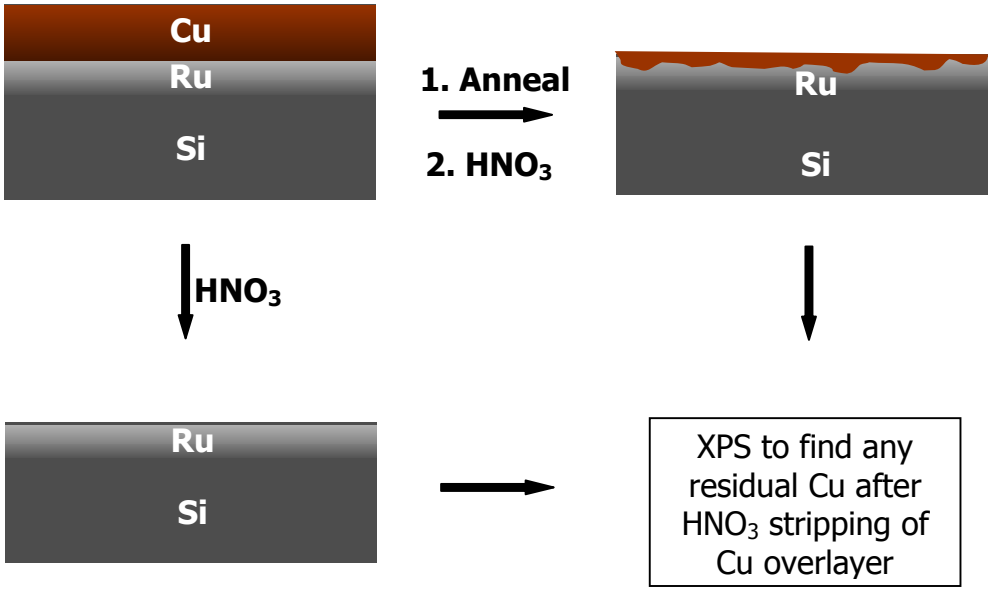

Figure 3.8: Scheme employing XPS for investigating the residual Cu in ECD and PVD Cu/(5 nm Ru)/Si samples at RT and after annealing at 300 ^{o}C, under vacuum for 10 min. and HNO_3 etching.

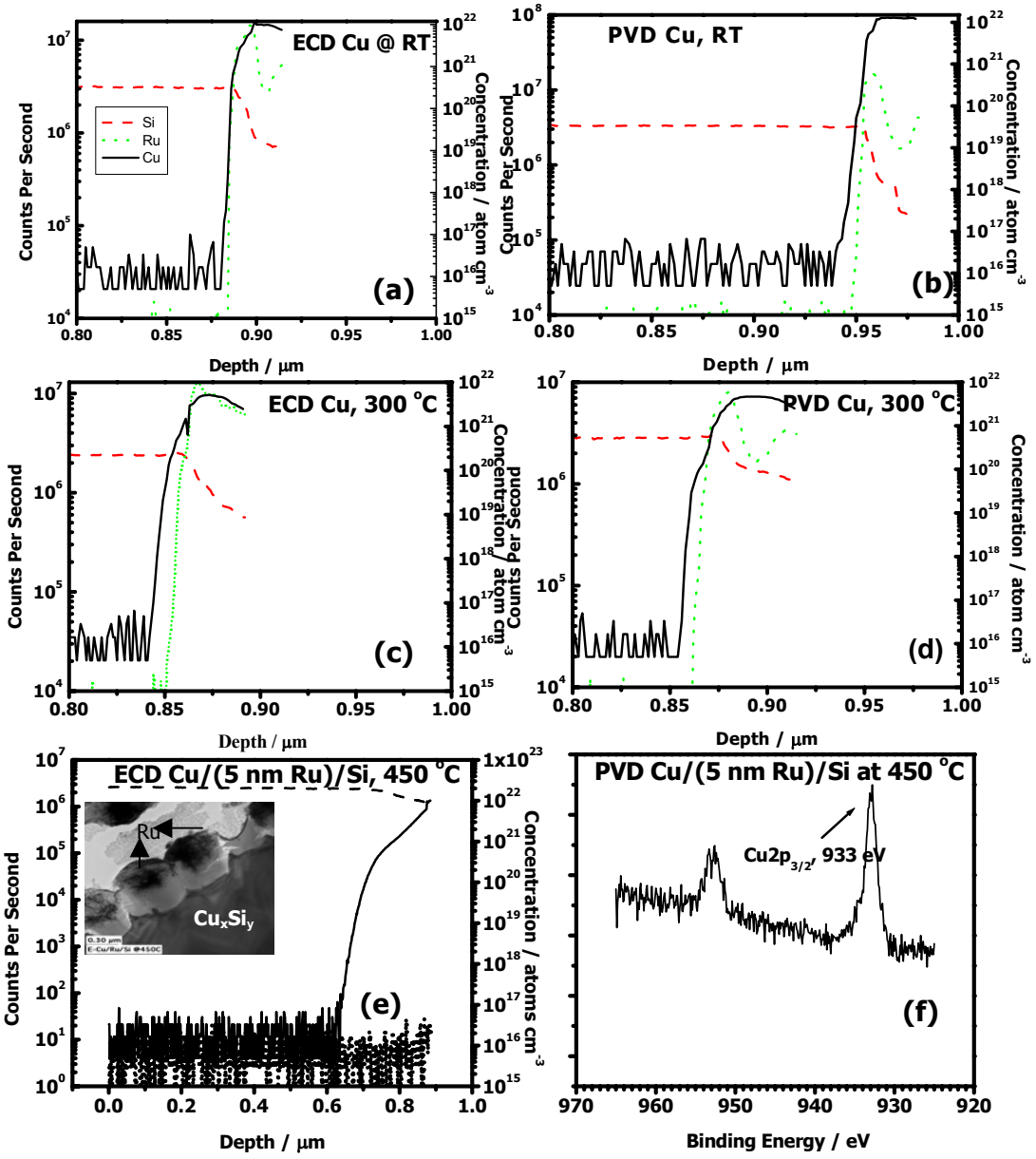

Figure 3.9: (a) – (e) Back-side SIMS Depth Profiling for ECD and PVD Cu/(5 nm Ru)/Si Structures at RT, 300 °C and 450 °C vacuum annealed for 10 min. (f) Cu XPS spectra for ECD and PVD Cu/(5 nm Ru)/Si at 450 °C, 10 min. vacuum annealed.

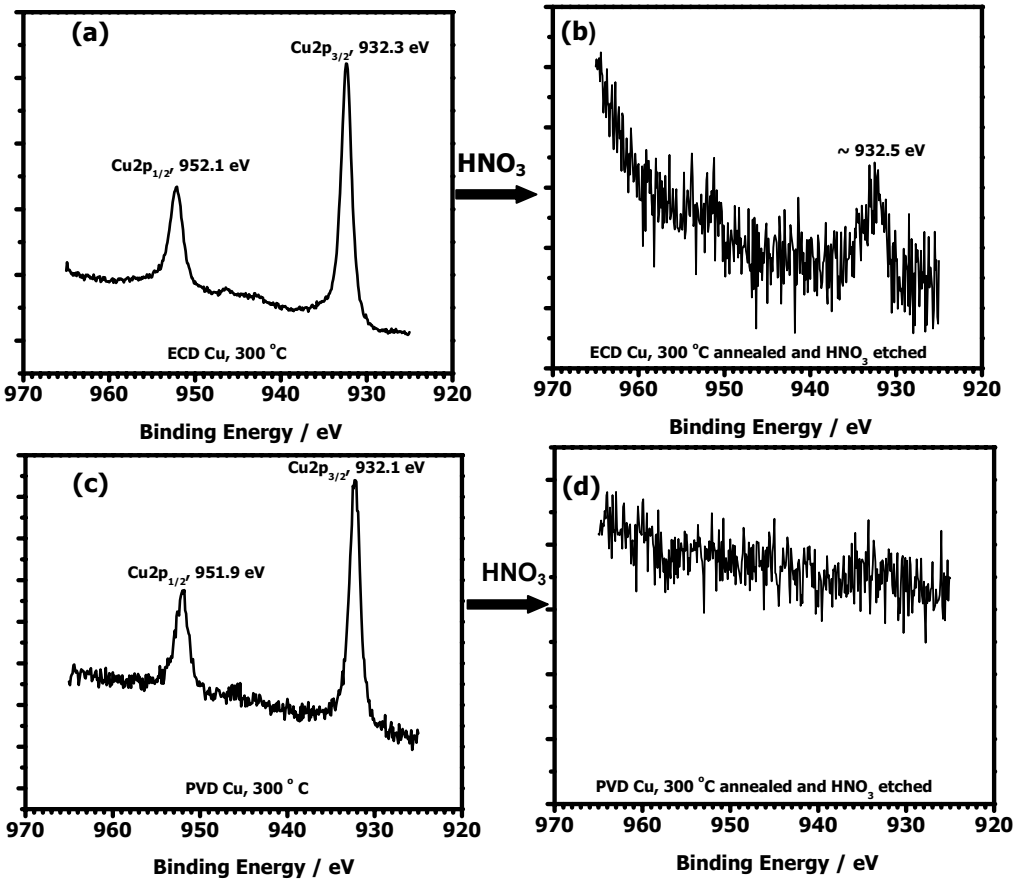

Figure 3.10: XPS spectra of ECD Cu/(5 nm Ru)/Si – (a) & (b) and PVD Cu/(5 nm Ru)/Si – (c) & (d) annealed at 300 ^{o}C in vacuum anneal for 10 min. and etched in concentrated HNO_3.

Figure 3.11 shows that RBS spectrum on Cu/Ru (5nm)/Si RT, 300^{o}C and 450^{o}C annealed samples under vacuum. It clearly shows that 450 ^{o}C anneal made the Ru fail as diffusion barrier but the Ru successfully blocks Cu diffusion under 300 ^{o}C anneal.

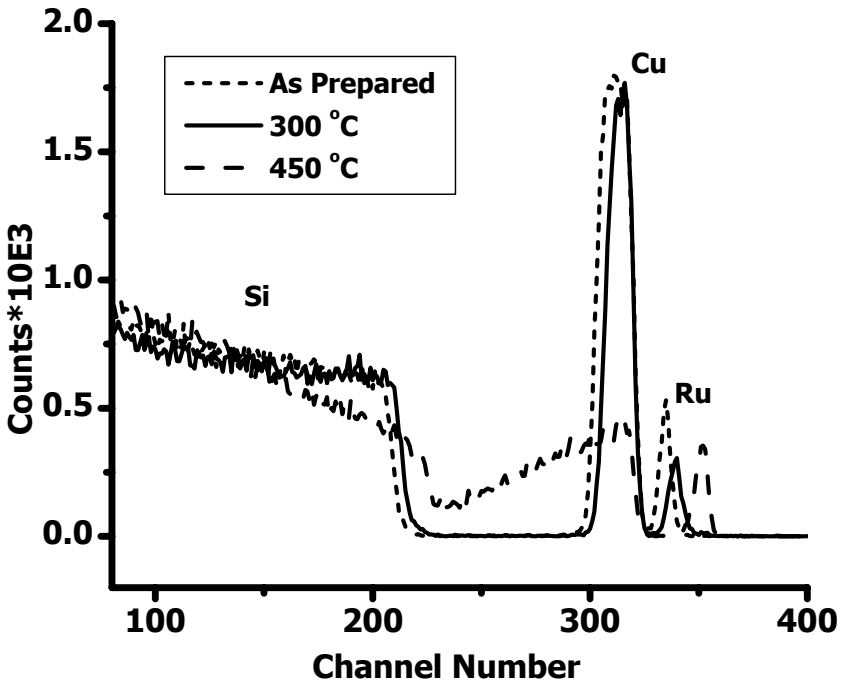

Figure 3.11: RBS spectrum shows Cu diffusion prevention by 5 nm Ru film up to 300 ^{o}C and Ru barrier failure at 450 ^{o}C. (10 min. vacuum annealing).

Figure 3.9 is the SIMS data on PVD and ECD Cu/Ru/Si. It provides additional evidence that the 5nm Ru can block the Cu diffusion under 300 ^{o}C anneal but fail at 450 ^{o}C. Figure 3.6 and figure 3.7 are TEM images taken on PVD and ECD Cu/Ru/Si sample at RT and 300 ^{o}C anneal. It is consistent with RBS and SIMS data.

3.4 Discussion

3.4.1 Characterization of Ru Thin Film

The Ru thin films, as prepared, were characterized using XPS shown in Figure 3.1, Figure 3.1-a is the O 1s. It clearly shows there are two kinds of O showing up, one is at ~ 532 eV, which comes from oxygen adsorption on the surface of the Ru films, another one is around 529.7 eV, which can be assigned as RuO_x. Figure 3.1-b is Ru 3d, you can see from the $Ru3d_{5/2}$, it was a minute asymmetry but the dominant peak is around 280 eV, which means that most of the Ru (bulk Ru) is Ru (0) metal. Figure 3.1-c is Si 2p, which was detected from the interface of the Ru and Si. There are apparently two peaks at 99.4 eV and 102-103 eV respectively. We believe that the first one is from Si substrate, the second one belong to Ru silicide, this is in agreement with the Ru silicide formation proposal between Ru and Si, which will be discussed in the following sections. There is another possible assignment for the second peak at 102-103 eV. It comes from SiO_x due to Si oxidizing with the oxygen source in the ambience in the PVD chamber. However this assignment is not compatible with the EELS data, which shows that the oxygen is below detecting limitation (less than 2 atomic %). Since there is no Ru silicide XPS data reported, no reference is available. To interpret the Si peak from the interface between Ru and Si precisely, more tools (such as XRD) and experiment are needed. The Ru silicide investigation is being carried on in our group right now.

3.4.2 Behavior of Ultra Thin Film Ruthenium as a Copper Diffusion Barrier*

The interfacial stability of electroplated Cu/(5 nm Ru)/Si film stack before and after vacuum annealing was studied using RBS. Figure 3.11 indicates that the Cu/(5 nm Ru)/Si structure remains intact after annealing at 300 °C for ten minutes. However, the 5 nm Ru barrier fails after 450 °C annealing as shown by RBS. The spectra of the 450 °C anneal shows clearly that Ru moved to the surface of the structure and the Cu film diffused into the Si substrate. TEM cross-sectional imaging was used to examine the microstructure and real-space physical arrangement of Cu/(5 nm Ru)/Si structures after annealing. As shown in

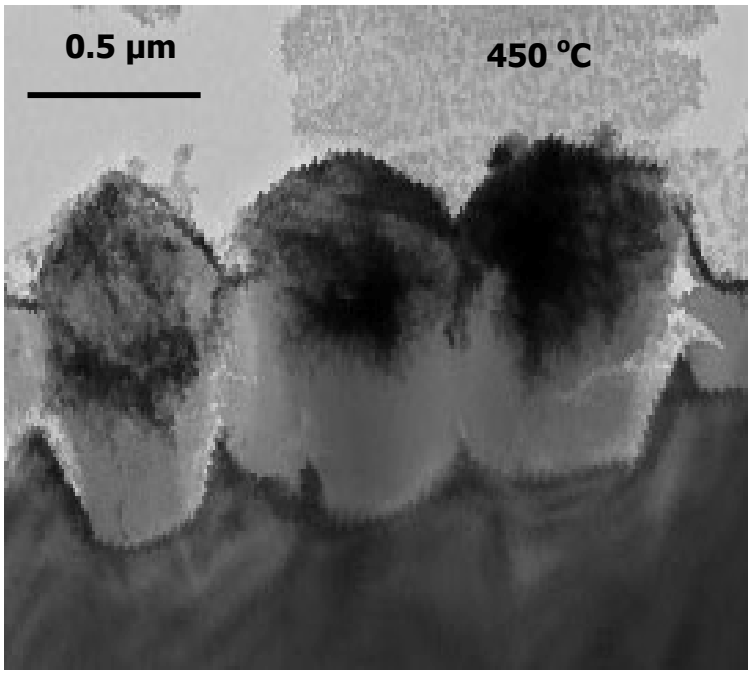

Figure 3.12: TEM image of the interface in sample electroplated Cu/(5 nm Ru)/Si annealed under vacuum for 10 min. at 450 °C.

* This section has been previously published: T. N. Arunagiri, Yibin Zhang, O. Chyan, M. El-Bounani and M. J. Kim, Applied Physics Letter, Vol 86 (8) pp.083104-1-083104-3. Reproduced with permission from the American Institute of Physics

Figure 3.7, TEM image concurs with RBS data to show that the Cu/Ru interface remains stable and unchanged after 300 °C anneal. Previously reported TEM data show that a thicker 20 nm sputtered Ru film has a columnar microstructure oriented vertically with respect to Si substrate.[9b] In contrast, an ultra thin 5 nm Ru film is amorphous and does not show columnar microstructure. Also, the thermally induced grain growth of electroplated Cu over layer is clearly seen on the top of 5 nm Ru film. Many of the Cu grains have expanded, after annealing, to cover the entire thickness of the electroplated Cu layer shown in Figure 3.6 - a

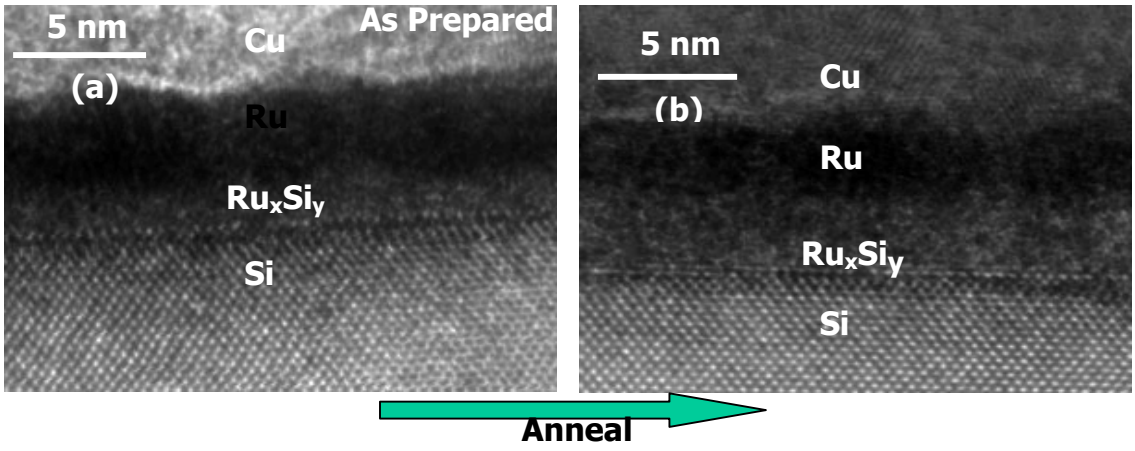

Figure 3.13: HRTEM of (a) Cu/(5 nm Ru)/Si structure shows a ~ 1-2 nm interlayer in the as-prepared Ru/Si samples and (b) after 300 ^{o}C annealing showing interlayer expansion to ~ 3 nm.

and b, the TEM image as shown in Figure 3.12, 5nm Ru will fail as Cu diffusion barrier annealing at 450 ^{o}C for 10min, this is in agreement with the RBS data.

High-resolution TEM images reveal the growth of an interlayer between Ru and its underlying Si substrate. Even prior to the annealing, Figure 3.13-a, the high-resolution TEM indicated that as prepared Ru film actually consists of ~ 4 nm Ru and a thin interlayer (~ 1-2 nm) with a lighter TEM contrast than Ru metal film. When annealed at 300 °C, Figure 3.13-b, the interlayer grew close to 3 nm at the expense of the Ru over layer (ca. 3 nm remaining) and likely of its underlying Si substrate as well. The interlayer remains amorphous throughout annealing. It is worth noting that the remaining 3 nm Ru film is still acting as an efficient diffusion barrier for Cu diffusion at 300 °C vacuum anneal. However, TEM shows extensive Cu diffusion into Si after 450 °C annealing and a complete breakdown of the Cu/(5 nm Ru)/Si interface corroborating the RBS finding.

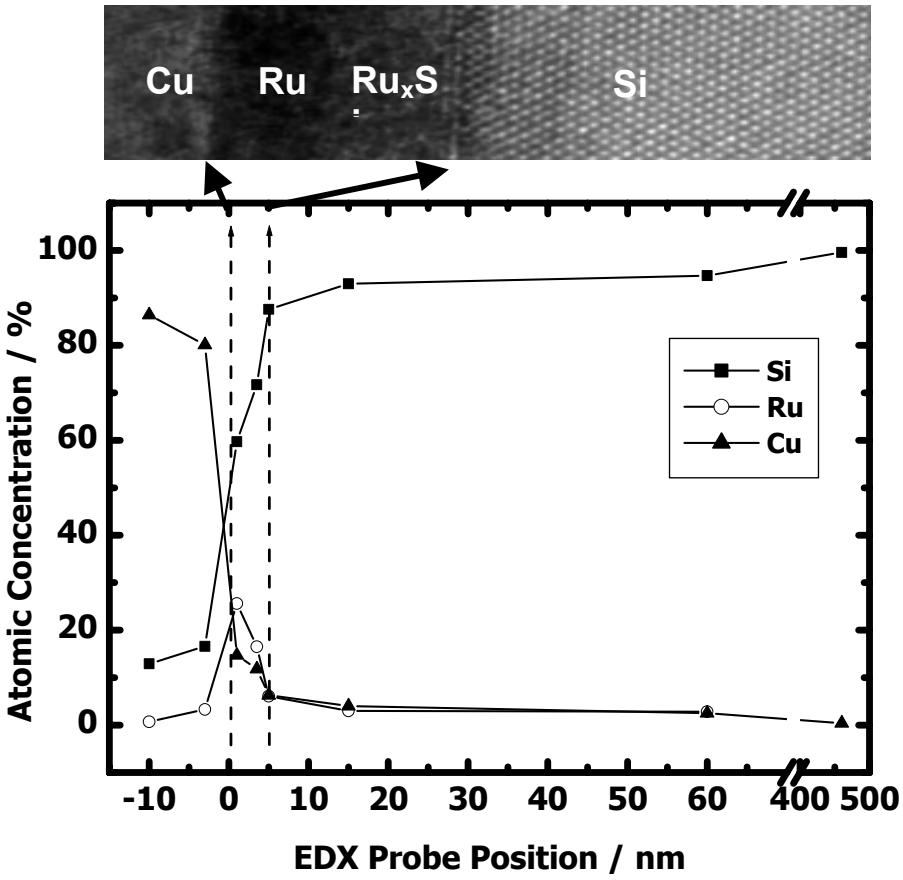

Figure 3.14: EDX atomic concentration profiling of the Cu/(5 nm Ru)/Si cross-section after vacuum annealed at 300 ^{o}C for 10 min.

High-resolution AEM analysis was employed to probe the elemental composition across the Cu/(5 nm Ru)/Si interfaces. Figure 3.14 depicts a depth profile of the percent atomic concentrations with respect to EDX probing position (~ 1 nm probe size) for 300 $^{\circ}$C annealed sample. The atomic concentration is calculated from the measured EDX intensity with an empirical sensitivity factor for each detected element. As depicted in Figure 3.14, the Cu signal depth profile suggests effective blocking of Cu diffusion by the ultra thin Ru barrier. The Ru

signal reaches a maximum on Ru metal thin film then decreases gradually across the interlayer and finally returns to baseline in Si back substrate. Furthermore, substantial Si was detected within the interlayer region before reaching the plateau of Si bulk substrate. To complement the EDX results, high-resolution electron energy-loss spectroscopy (EELS) was used to probe the oxygen content across the Cu/(5 nm Ru)/Si interface. EELS data indicate all oxygen signals are below instrumental detection limit.

Study of ruthenium silicide (Ru_2Si_3) formation by thermally induced inter-layer reaction between Ru and Si has been reported.[14,15] It has been shown that Si is a dominant diffusion species in the chemical interaction between Si and Ru.[15] Also, transformation of a denser Ru film to a less dense Ru_2Si_3 increases the original thickness of Ru film after silicidation.[14] In the current study, the EDX depth profiling clearly shows co-existing of Ru and Si within the ~ 3 nm interlayer. Also, the total thickness of Ru/interlayer has expanded by ca. 10% after 300˚C annealing as revealed by the high-resolution TEM images, Figures 3.13-a &3.13-b. Therefore, our AEM analysis data suggest that the interlayer of annealed sample is likely to be ruthenium silicide (Ru_xSi_y) formed by diffusion/reaction of Si with Ru.

One should note that the as-prepared Ru/Si samples also contain a thin (~ 1-2 nm) interlayer. Silicon oxide formation during sputtering could also be the potential source of the interlayer. However, the subsequent EELS analysis, performed on the 300˚C vacuum annealed structure, shows oxygen content to

be lower than instrumental detection limit (< 2 atomic %). We suggest that the interlayer in the as-prepared structure is mostly a non-stoichiometic ruthenium rich silicide. Room temperature metal silicide formation has been previously reported on similar noble metals like Pt and Ir.[16] In addition, the reported bond formation enthalpy for Si-O (800 kJ/mol) is twice that of Si-Ru. (397 kJ/mol). [17] Consequently, the more stable silicon oxide layer would have functioned as a passivation layer to prevent the observed interlayer growth process similar to the finding by Matsuri et al.[14]

The current finding implies that the silicide formation within the Ru/Si interface may determine the failure temperature of 5 nm Ru-based diffusion barrier. When annealed to 450 °C, cross sectional TEM shows fragmentation of Ru containing patches scattered on top of an extensive Cu silicide formation. One likely cause is that the continuous conversion of Ru to Ru_xSi_y eventually nullifies the remaining Ru barrier function and leads to a complete diffusion of the Cu through the Ru silicide into the Si substrate that would eventually form Cu silicide. Kwak et al. have reported that formation of a Ta-Si amorphous interlayer is the main cause of Ta barrier failure in Cu/Ta/Si structure.[18] Our recently reported diffusion study shows Cu can diffuse through a thicker 20 nm Ru barrier film to react with Si substrate after 550 ^oC annealing.[9b] The inter-grain boundaries within the Ru columnar microstructure could be the energetically favorable paths for the Cu diffusion. Subsequent TEM shows the delamination of an intact 20 nm Ru film after Cu penetration into Si substrate. In contrast,

current work shows 3-5 nm amorphous ultra-thin Ru film can withstand Cu-diffusion to at least 300 ^{o}C and fails at a higher temperature mainly through the interlayer silicidation process.

3.4.3 Comparison PVD Cu an ECD Cu in the Diffusion Study

TEM images of ECD Cu/(5 nm Ru)/Si and PVD Cu/(5 nm Ru)/Si have been shown in Figure 3.6-(a) – (d) and (e) – (h) respectively. TEM images on the left depict as-prepared samples before thermal annealing. While those on the right show TEM images after vacuum anneal at 300 ^{o}C for 10 minutes. In the TEM images of Figure 3.6-(a) and (e), as-prepared ECD Cu layer shows a less-dense deposit compared to its PVD Cu counterpart. This is likely due to the H_2-evolution reaction that also occurs on Ru during Cu electroplating process, thereby affecting the ECD Cu deposit. However, both ECD and PVD Cu deposits undergo similar thermal induced Cu grain growth process when annealing to 300 ^{o}C. As clearly visible in both Figure 3.6-(b) and (f), most of Cu grains have expanded into the whole thickness of the Cu film.

High-resolution TEM images, Figure 3.6-(c) and (g), show an interfacial layer (ca. 1 – 2 nm) between Ru and Si for both ECD and PVD Cu/(5 nm Ru)/Si film stacks at RT. The interfacial layer grows to ca. 3-4 nm after annealing at 300 ^{o}C while Ru layer decreases to about 2-3 nm in thickness. It was mentioned that this interfacial layer growth is due to Ru-silicide formation at RT.[13] Although the Ru layer erodes down from 5 to less than 3 nm due to silicidation, it still effectively impedes both ECD and PVD Cu diffusion into Si up to 300 ^{o}C. This

observation is very significant in supporting Ru as a promising liner material for the next generation IC platform, since the barrier thickness is expected to scale down to ≤ 5 nm at the 45 nm nodes. Thus except for the difference in the initial 'packing density' of ECD and PVD Cu deposits, all Cu/(5 nm Ru)/Si structures show Ru silicidation at the Ru/Si interface and maintain their stability up to at least 10 min. vacuum anneal at 300 ^{o}C.

SIMS depth-profiling investigation was undertaken to discern the relative elemental composition across the interfaces in Cu/(5 nm Ru)/Si structures and to supplement TEM data. The rationale for following a back-side SIMS route i.e. from under the Si layer up rather than from Cu layer down across Cu/(5 nm Ru)/Si structures was to avoid any misinterpretation due to primary ion knock-on and atom mixing effects.[9b] Figure 3.9-(a) – (e) show the backside SIMS profiling of ECD and PVD Cu/(5 nm Ru)/Si structures. At RT both ECD and PVD Cu structures (Figure 3.9-(a) and (b)) clearly show a large Si signal plateau until the Ru/Si interface is reached. At this point both Ru and Cu atom concentration begin to increase. As the primary beam continues removing Ru and reaches the Cu/Ru interface, the detected Ru atom concentration shows a decline. The profiling is continued further into the Cu layer where predominantly Cu atoms are detected. Similar profiles are obtained for ECD and PVD Cu/(5 nm Ru)/Si structures after 10 min. vacuum anneal at 300 ^{o}C. The SIMS data shows that there is maintenance of structural integrity with no drastic movement of Cu atoms detected across the ultra thin Ru film barrier into Si. In other words, the

results corroborate TEM data and demonstrate the prevention of Cu diffusion by an ultra thin ≤ 5 nm Ru film for at least up to 10 min. in vacuum at 300 ^{o}C.

However, when ECD and PVD Cu/(5 nm Ru)/Si samples were annealed at 450 ^{o}C in vacuum for 10 min., backside SIMS (Figure 3.9-e) detects Cu atoms much before Si concentration falls. The results indicate that the ultra-thin Ru film fails to prevent Cu diffusion into Si at 450 ^{o}C. Corresponding TEM image (inset in Figure 3.9-e) shows the breakdown of the ultra thin Ru film (with remnants) and mixing of Cu with Si. The corresponding optical images indicate a complete fading of Cu metallic color and replaced by a rough surface morphology with dark brown features of ca. 1 μm. Also, the apparent sheet resistivity has increased. The progressive erosion of the Ru ultra-thin barrier by silicidation is attributed to be the main cause of ultra-thin Ru barrier breakdown. XPS confirms the formation of Cu-silicide as expected after the break down of Ru barrier. Figure 3.9-f shows the XPS region scan with the Cu $2p_{1/2}$ and Cu $2p_{3/2}$ peaks located at 952.6 and 933.0 eV, respectively, which are in agreement with literature reported Cu_3Si.[19-22]

Although SIMS depth profiling analysis is useful in assessing the overall interfacial integrity, its lateral resolution is limited by artifacts of sputtering such as mixing of atoms at the surface, ion implantation and preferential sputtering. In contrast, XPS analysis is non-destructive with ample sensitivity (10^{-1} monolayer). Through prudent design of experiments, it can be tailored to study thin film interfaces effectively. In order to probe Cu/Ru interface within the Cu/(5

nm Ru)/Si film stack after annealing, Figure 3.10-(a) and (c) show XPS Cu region spectra respectively for ECD and PVD Cu/(5 nm Ru)/Si samples after annealing for 10 min. in vacuum at 300 ^{o}C. The Cu $2p_{1/2}$ and Cu $2p_{3/2}$ peak profile and locations show that both ECD and PVD Cu remain in metallic state after annealing. After etching off Cu with HNO_3 and subjecting to XPS again, the PVD Cu/(5 nm Ru)/Si sample showed no Cu within XPS detection limit, while ECD Cu/(5 nm Ru)/Si sample showed residual Cu, which could not be removed even after extended periods of HNO_3 etching. Similar experiments when performed on thicker Ru films i.e. ECD and PVD Cu/(20 nm Ru)/Si samples, again showed residual Cu only with ECD Cu/(20 nm Ru)/Si samples.

According to the presence of XPS Cu $2p_{3/2}$ at ~ 932.5 eV, in Figure 3.10-b, and absence of oxide O 1s at ~ 530.3 eV, the detected Cu residue in the annealed ECD Cu/Ru/Si samples after HNO_3 etching is assigned to zero valence metallic state.[23, 24] The aggressive HNO_3 etching precludes the present of ECD Cu on Ru surface. Hence, the likely place where this ECD Cu could be present after annealing of the ECD Cu/(5 nm Ru)/Si structure is either within the ~ 6 nm Ru/Ru-silicides layer or further down into the bulk Si substrate. Based on the limiting escape depth of X-ray photoelectron, we propose that the detected ECD Cu XPS signal did not originate from the deeper Si substrate. Hence, the residual Cu likely resides in the 6 nm Ru/Ru-silicides double layer. These observations imply that a minute amount of ECD Cu is diffusing further into ultra-thin Ru film.

The principal difference between ECD and PVD Cu is their processing condition. While ECD of Cu relies on the reduction of Cu^{+2} ions from acidic solution on the Ru surface, PVD of Cu depends on thermally evaporated Cu to coat Ru in a line-of-sight deposition. The wet electrochemical process could allow ECD Cu to have a more conformal coating along the terrain of 5 nm Ru film surface.[9] However, the observed grain growth process after annealing should homogenize this minor initial packing difference of ECD and PVD Cu at the Cu/Ru interface. Alternative explanation for the observed Cu residues in ECD Cu/Ru/Si could arise from some Ru surface modifications (possibly) occurring during the wet Cu electroplating. For instance, H_2-evolution occurs alongside with the Cu deposition during cathodic scan. Ru is known to absorb large quantities of H_2. The solubility of the latter can be as high as 1500 times its volume.[25] The absorbed H_2 along with any electrolyte species impurities may change its physico-chemical properties of ultrathin Ru film to aid in Cu diffusion. Another possible reason to cause that PVD Cu shows better result than ECP Cu. That is Ru oxide, this will be discussed in detail latter.

3.4.4 The Role of Ru Oxide in Blocking Cu Diffusion

For the future 45-65 nm integrated circuit devices, the thickness of a functional diffusion barrier is limited to merely 5 nm. Such an ultra thin nonepitaxial metal film was demonstrated by Gjostein, [26] where grain boundaries and dislocations are abundant and provide the least resistant paths for Cu interdiffusion.

Conceivably, conductive ruthenium oxide can be delivered to plug the grain boundary diffusion passage prior to Cu electroplating for maximizing the Ru-based barrier performance.[27, 28]

As pointed about above, another possible reason which causes PVD Cu performs better than ECD Cu is RuO_x on top of bulk Ru, which plays a role to plug the Ru boundary and limit the path for Cu diffusing through Ru, as shown in Figure 3.15. The XPS data in Figure 3.1 show that there is some RuO_x on the surface of 5nm Ru film from the O 1s, two peaks show up, ~532 eV and ~ 529.7 eV. The former is from the adsorption O_2 from air in the XPS chamber, and the latter is from RuO_x. Since ECD Cu plating will go through electrochemical reaction in acid bath, the observed Cu residues in ECD Cu/Ru/Si shown in Figure 3.10-b could arise from some Ru surface modifications (possibly) occurring

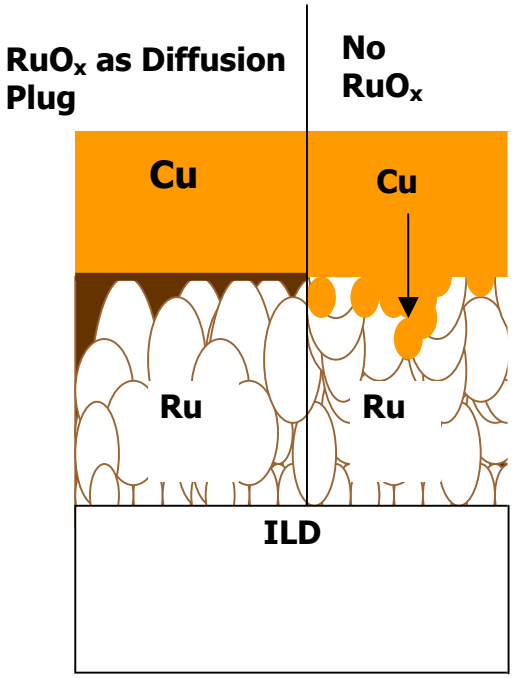

Figure 3.15: RuO_x on the bulk Ru to block Cu diffusion due to oxygen atom plug into the boundary between Ru atoms.

during the wet Cu electroplating. For instance, H_2-evolution occurs alongside with the Cu deposition during cathodic scan. Probably, RuOx was removed during this electrochemical process. So the Cu can slowly diffuse inside Ru film as Cu (0), which inserts between the Ru atoms and can not be removed by HNO_3 etching. It was confirmed by XPS as mentioned above shown in Figure 3.10-b. But for PVD Cu, since Cu is physically deposited on the 5nm Ru, so the very thin layer of RuO_x is still on the top of "bulk" Ru. It makes the Cu/Ru/Si structure more stable during anneal, the Cu has no chance get into Ru "bulk" annealing at 300 ^{o}C from 10min, as show in Figure 3.10-d.

Currently, the project of using RuO_x to improve the Ru function as Cu diffusion barrier is ongoing in our group. We have two ways to put RuO_x on the top of bulk Ru, electrochemically and physically (PVD). The advantage of the former is that UPD Cu can be plated on the electrochemical RuO_x surface conformally and strongly as reported.[9c] PVD RuO_x is an advanced technology, but for vias and trenches with high-aspect-ratio (over 10), PVD will have an formidable difficulty to deposit a few Å of RuOx deposition within light special constrains for 45 nm node.[29] So, Atomic Layer Deposition (ALD) is another choice to implement a few Å RuO_x deposition conformally.[8, 12,30-31] Also, as the hint we can get from Figure 3.3 and Figure 3.4, thermally formed RuO_x is another potential choice of intergrain diffusion blocker. It can be controlled by changing the anneal temperature, time and the ambience. The resolved angle XPS data clearly shows that a layer of RuO_x was formed on the surface after annealing. It is in agreement with the Figure 3.4, after Ar^+ sputtering, only Ru (0) was left with adsorbed oxygen (532 eV), and that means the bulk Ru underneath the RuO_x remains metallic during the RuO_x forming process.

3.5 Summary

We have demonstrated that direct Cu plating on a 5 nm Ru film, prepared by magnetron sputtering, is feasible with good Cu quality. The high-resolution TEM combined with RBS data establishes the interfacial stability between Cu/(5 nm Ru)/Si after annealed at 300 ^oC. High-resolution EELS analyses showing no O, supported by EDX, reveal an interlayer silicidation process that is attributed to

the final break down of Ru barrier layer. The data suggest that Ru thin film is a good candidate as a directly platable Cu diffusion barrier for the advanced integrated circuits application.

Comparative interfacial characterization study was carried out on ECD Cu and PVD Cu deposited (5 nm Ru)/Si structure. TEM reveals a less-denser packing morphology of ECD Cu as compared to PVD Cu. Both PVD and ECD Cu/(5 nm Ru)/Si structures retain their interfacial integrity after vacuum annealing at 300 ^{o}C. The thermally induced Ru silicide formation causes the break down of ultra-thin Ru barrier at 450 ^{o}C as revealed by TEM, backside SIMS, XPS and resistivity measurements. XPS analyses after etching removal of Cu overlayer show that minute ECD Cu could penetrate further into Ru thin film matrix as comparing to PVD Cu.

3.6 References

1) Singer, P. In *Semiconductor International*, (**2004**).

2) Peters, L. In *Semiconductor International*, (**2003**).

3) S.P. Murarka, *Mater. Sci. Eng., R*. **19**, 87 (**1997**).

4) Y. Shacham-Diamand, *J. Electron. Mater.* **30**,336 (**2001**).

5) K. M. Takahashi, *J. Electrochem. Sco.,* **147**, 1414 (**2000**).

6) International Technology Roadmap for Semiconductor -2002 Update, Semiconductor Industry Association (**2002**), pp. 74-75; see http://public.itrs.net/.

7) Binary Phase Alloy Digrams, 2nd ed., T. B. Massalski, Editor, p. 1467, Materials

Information Society, (**1990**).

8) M. W. Lane, C. E. Murray, F. R. McFeely, P. M. Vereechen, and R. Rosenberg. *Appl. Phys. Lett.* **83**, 2330 (**2003**).

9) a) O. Chyan, T. N. Arunagiri and T. Ponnuswamy, *J. Electrochem. Soc.,* **150**, C347 (**2003**). b) R. Chan, T. N. Arunagiri, Y. Zhang, O. Chyan, R. M. Wallace, M. J. Kim, T.Q. Hurd, *Electrochem. Solid-State Lett.,* **7**, G154 (**2004**). c) Y. Zhang, L. Long, T. N. Arunagiri, O. Ojeda, S. Flores, O. Chyan, R. M. Wallace, *Electrochem. Solid-State Lett.,* **7** (9), C107 (**2004**).

10) D. Josell, D. Wheeler, C. Witt and T. P. Moffat, *Electrochem. Solid-State Lett.* **6**, C143 (**2003**).

11) Q. Wang, J. G. Ekerdt, D. Gay, Y. M. Sun, J. M. White, *Appl. Phys. Lett.* **84**, 1380 (**2004**).

12) H. Kim, *J. Vac. Sci. Technol. B,* **21** (6), 2231 (**2003**).

13) Arunagiri, T. N.; Zhang, Y.; Chyan, O.; El-Bouanani, M.; Kim, M. J.; Wu, C. T.; Chen, L.-C.; Chen, K.-H. *Appl. Phys. Lett.*, **86** (8), 083104-1 (**2005).**

14) Y. Matsui, Y. Nakamura, Y. Shimamoto, M. Hiratani, *Thin Solid Films*, **437**, 51 (**2003**).

15) E.V. Jelenkovic, K.Y. Tong, W.Y. Cheung, S. P. Wong, *Semicond. Sci. Technol*. **18**, 454 (**2003**).

16) S. J. Morgan, R. H. Williams, J. M. Mooney, *Appl. Surf. Sci.*, **56-58**, 493 (**1992**).

17) David R. and H. P. R. Frederikse, CRC Handbook of Chemistry and Physics,

CRC press, 77th Ed. New York, (**1996**).

18) J.S. Kwak, H.K. Baik, J.H. Kim, S.M. Lee, *Appl. Phys. Lett.,* 71, 2451 (**1997**).

19) Qu, X. P.; Lu, H.; Peng, T.; Ru, G. P.; Li, B. Z. *Thin Solid Films*, **462-463**, 67 (**2004**).

20) Sarkar, D. K.; Bera, S.; Narasimhan, S. V.; Chowdhury, S.; Gupta, A.; Nair, K. G. M. *Solid State Comm.*, **107**, 413 (**1998**).

21) Shin, D. W.; Wang, S. X.; Marshall, A. F.; Kimura, W.; Dong, C.; Augustsson, A.; Guo, J. *Thin Solid Films*, **473**, 267 (**2005**).

22) Cros, A.; Aboelfotoh, M. O.; Tu, K. N. *J. Appl. Phys.* **67**, 3328 (**1990**).

23) C. A. N, Fernando, P. H. C. de Sila, S. K. Wethasinha, L. M. Dharmadasa, T. Delsol, M. C. Simmonds, *Renewable Energy,* **26**, 512 (**2002**).

24) N. S. Mclntyre and M. G. Cook, *Analytical chemistry*, **47**(13), 2008 (**1975**).

25) Llopis, J. F.; Tordesillas, I. M. In *Encyclopedia of Electrochemistry of the Elements*; Bard, A. J., Ed.; Marcel Dekker Inc.: New York, Vol. VI, 278-295 (**1976**).

26) N. A. Gjostein, *Diffusio*n, American Society for Metals, Metals Park, OH (**1973**).

27) M. A. Nicolet, *Thin Solid Films,* **52**, 415 (**1978**).

28) E. Kolawa, F. C. T. So, E. T.-S. Pan, and M.-A. Nicolet, *Appl. Phys. Lett.,* **50**, 854 (**1987**).

29) International Technology Roadmap for Semiconductor, Semiconductor Industry Association (**2001**), see http://public.itrs.net/.

30) M. Ritala and M. Leskela¨, Nanotechnology, **10**,19 (**1999**).

31) M. Leskela¨ and M. Ritala, Thin Solid Films, **409**,138 (**2002**).

32) M. W. Lane, C. E. Murray, F. R. McFeely, P. M. Vereecken, and R. Rosenbaum, Appl. Phys. Lett. **83**, 2330 (**2003**).

CHAPTER 4

RU ELECTROCHEMICAL BEHAVIOR IN HIGH PH $CUSO_4$ ACIDIC

4.1 Introduction

Electrochemical deposition of Cu in Cu^{2+} ion solution has been widely studied. Most of the studies focused on two regions: investigation in acid solution (pH less than 1) and in basic solution (pH is higher than 8). For the latter, precisely saying, it is Cu_2O deposition rather than Cu deposition.

Switzer's group reported a series of studies of Cu_2O, including investigation of Cu and Cu_2O layered nanostructure, [1,2] Cu_2O nanocubes on InP(001)[3] and epitaxal electrodeposition of Cu_2O.[4,5] Their work was mainly performed in basic solution (pH 8-12). S. Leopold and coworkers reported electrochemical deposition of cylindrical Cu/Cu_2O microstructures in basic solution (pH around 9.3)[6]. Y.C. Liu group formed $Cu_2O/ZnO/ITO$ stack by using electrochemical method, Cu_2O layer was deposited in pH 10 solution.[7]

Electrochemically plating Cu is popular due to its low cost, low process temperature, and good ability to fill vials in the microstructure of Cu interconnect compared to physical vapor deposition (PVD) and chemical vapor deposition (CVD).[8] For most of reports of Cu plating on metals, it is always conducted in low pH acid solution.[9-12] Previously, we reported that Cu could be electrochemically plated on Ru film.[13] Also we investigated electrochemical (Echem) behavior in acid $CuSO_4$ solution.[14] To get systematic study on Ru, we tried to increase the pH value of the solution. Compared to our previous work in

low pH acid solution (pH=0), [14] an apparently different behavior of Ru in higher pH acid solution (greater than 4) was observed. Per our acknowledge, little is known about the mechanism of Cu plating on noble metal (such as Ru and Pt) in higher pH acid solution (pH 4-7).

In this chapter, electrochemical deposition of Cu on a polycrystal Ru electrode surface was investigated in $CuSO_4$ solution of different pH value. As a comparison experiment, Pt was studied under the same condition as Ru. The result is similar. Especially, detail investigation was performed in pH 5 solution on Ru and Pt. Cu plating bath was adjusted to pH = 5 by adding appropriate acid or base. Cyclic voltammetry (CV) data indicates a distinct difference of electrochemical behaviors in solution pH5 compared to low pH solution (pH=0). XRD, SEM, XPS and electrochemical quartz crystal microbalance (EQCM) were used to characterize the chemical oxidation states, deposit-mass variation and morphology on Ru and Pt electrode surface. In pH 5 solution of $CuSO_4$ + K_2SO_4, based on XPS, XRD and EQCM results, we observed an interesting posnjakite [$Cu_4SO_4(OH)_6.H_2O$] formation triggered by electrochemical processes on the Ru and Pt electrode surface. Cu (I)-Cu_2O was found in the process. In this chapter, the mechanism of electrochemical reaction will be given and a proposed mechanism of forming $Cu_4SO_4(OH)_6.H_2O$ on Ru and Pt surface will be discussed.

4.2 Experimental

Ru shots (ESPI Inc.) were made into disk electrodes as described previously in the reported procedure.[13] Ruthenium (99.95% pure) was deposited on a precleaned Si wafer by a standard magnetron sputtering system (base pressure, $1* 10^{-8}$ Torr). High purity potassium sulfate (K_2SO_4, Aldrich) and Copper sulfate ($CuSO_4$, Mallinckrodt) were used to make all electrolyte solutions in ultra pure water (18.2 MΩ Millipore).

Electrochemical investigation was performed by using CHI 440 (CH Instruments) and model M273 (EG&G, Princeton Applied Research) potentiostat/galvanostats. A conventional three-electrode cell with a Pt sheet as the counter electrode (CE) and Murcury/Murcury Sulfate (3 M K_2SO_4)-MSE as the reference electrode was employed, all the potentials reported are relative to MSE. Pt rod (d = 0.002 inch) was used as CE in EQCM.

EQCM data were collected on an Electrochemical Workstation Model 400 (CH Instruments, Austin TX). The electrochemical quartz crystal nanobalance (also known as EQCM for its "Micro" suffix) has been proven to be an effective mean of monitoring nano-scale mass changes related to electrode potential variations at its surface. The principles of operation are based on the converse piezoelectric response of quartz crystals to mass variations in the crystal's surface. The EQCM is based on an electronic circuit driving an AT-cut quartz crystal resonator; these two compose an electronic oscillator.

Saurbrey[15] first demonstrated the relationship between a crystal vibrating and the corresponding changes in mass by a series of simple deductions based on the thickness shear mode of oscillation of a quartz crystal: [16]

$$\Delta f = \frac{-2\Delta m f_0^2}{A\left(\mu_q \rho_q\right)^{\frac{1}{2}}}$$

Where f_0 is the resonant frequency of the fundamental mode of the crystal, A is the area of the Pt disk coated onto the crystal (0.206 cm^2 for given crystal), ρ_o is the density of the crystal and μ is the shear modulus of quartz. EQCM is combined QCM to electrochemistry for the determination of metals deposited onto the crystal. The equation is commonly re-arranged in a way that the relationship between frequency change and mass change is easily observed:

$$\Delta f = -C\Delta m$$

The quartz crystals (ICMG, Oklahoma City) have a fundamental frequency of 7.995 Mhz; a constant value of $C=7.064\times10^6 hz/g*cm^2$ was observed. The electrode structure used in our study is Pt (1000 Å)/ Ti (100 Å)/ quartz.

One of the main advantages of the EQCM technique in the study of adsorption phenomena[17] is the possibility of obtaining simultaneous voltammetric and gravimetric response. An equivalent molar mass can be determined according to Faraday's law, and get direct information about the electrode reaction species,

measured at the same surface. In addition, stainless steel wires extending from the metallic electrode surface were fixed by using silver epoxy (Tracon, Inc.), and soldered to copper rods. This established the connection between the oscillator box and the quartz crystal, and allowed the use of the optical microscope.

XRD Characterization was done on Simens D-500 Defractometer. A Cu Kα X-ray source and a DACO (Socabim, Germany) detector with computer control were employed to acquire the diffractograms. The experiments were run in the 2-68° 2θ angle range; the step size was 0.05° and dwell time was 1 s. XPS data were collected using a VG ESCALAB MKII spectrometer (VG Scientific Ltd) with Al Kα or Mg Kα X-ray as the excitation source. Optical images were recorded using a microscope (Nikon ME600L).

4.3 Results

Ru behavior in different pH solution was explored as shown in figure 4.1 (pH=1, 2, and 3) and in Figure 4.2 (pH=4, 5 and 6). Triple CVs were collected continuously in each pH solution with 2mM $CuSO_4$ /0.1M K_2SO_4. The shape of CVs has no difference in low pH solution (PH=1, 2, 3) shown in Figure 4.1. Only one reduction peak (Cu^{2+}/Cu) in cathodic region and one corresponding oxidation peak (Cu/Cu^{2+}) in anodic region. The three CVs in each solution overlap each other, which mean the redox couple is reversible in pH 1, 2 and 3 solutions. Starting in pH4 solution as shown in figure 4.2, the CV shape gradually

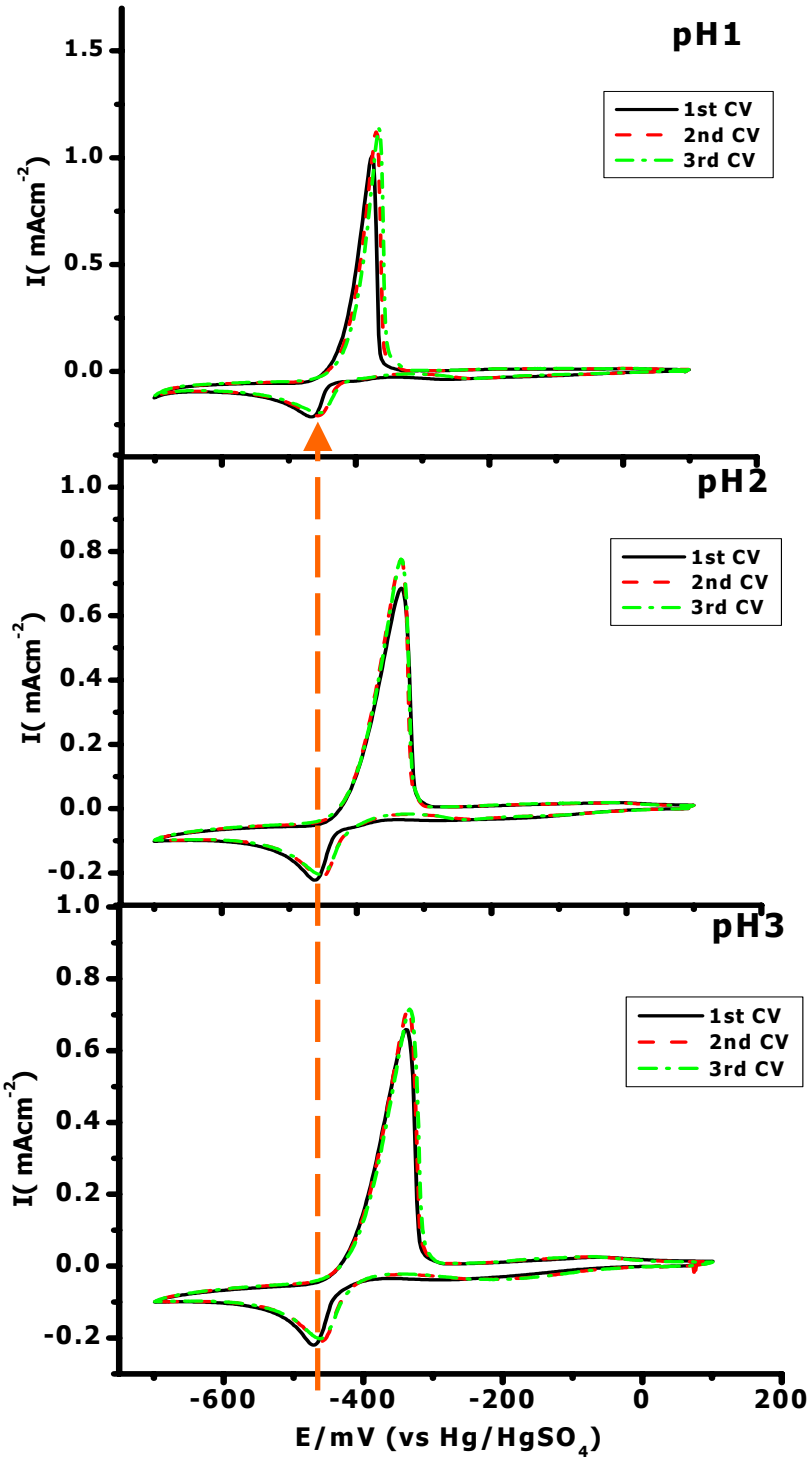

Figure 4.1: Ru in pH 1, 2 and 3 solution 2mM$CuSO_4$/0.1M K_2SO_4, three cyclic voltammetry was collected continuously in each solution.

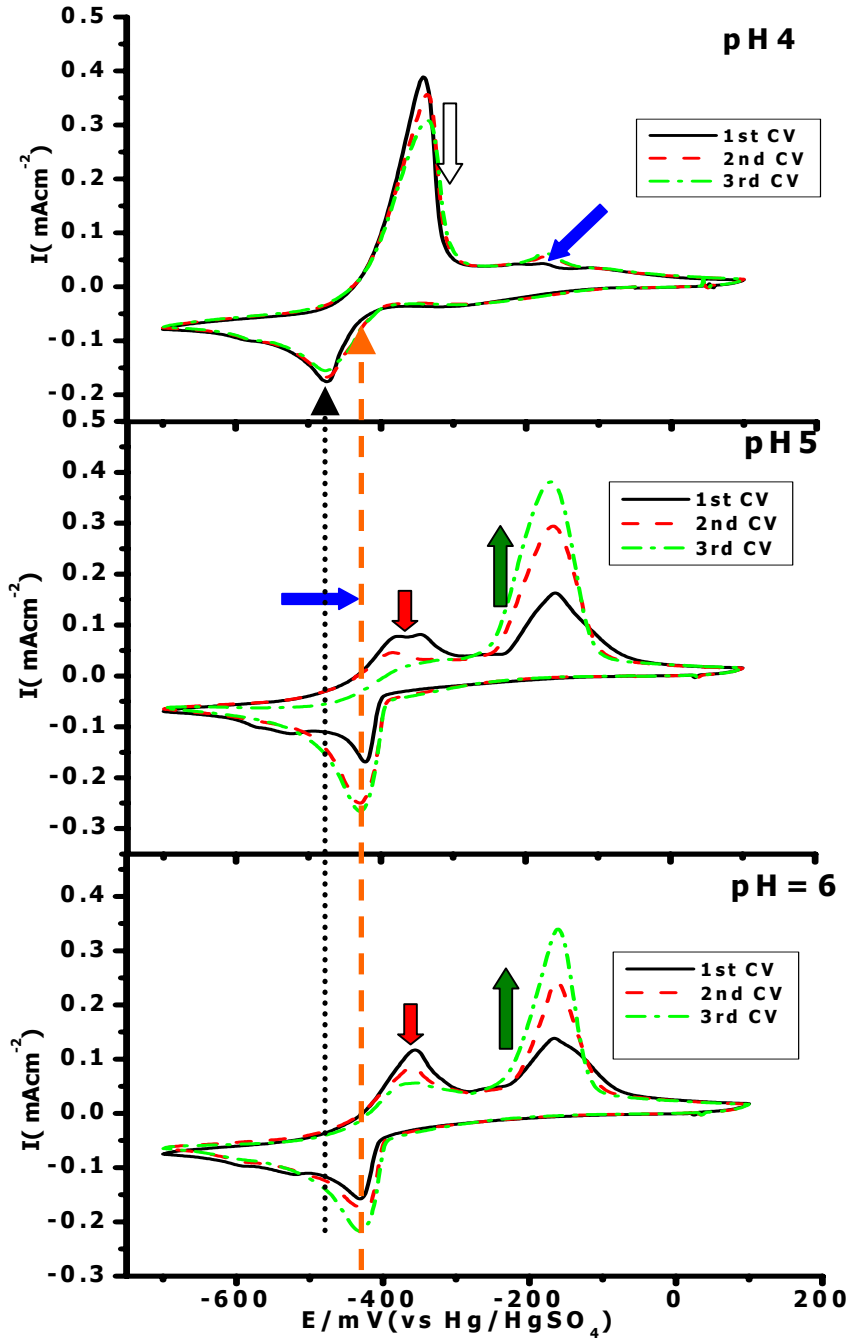

Figure 4.2: Ru in pH 4. 5 and 6 solution 2mM $CuSO_4$/0.1M K_2SO_4, three cyclic voltammetry was collected continuously in each solution.

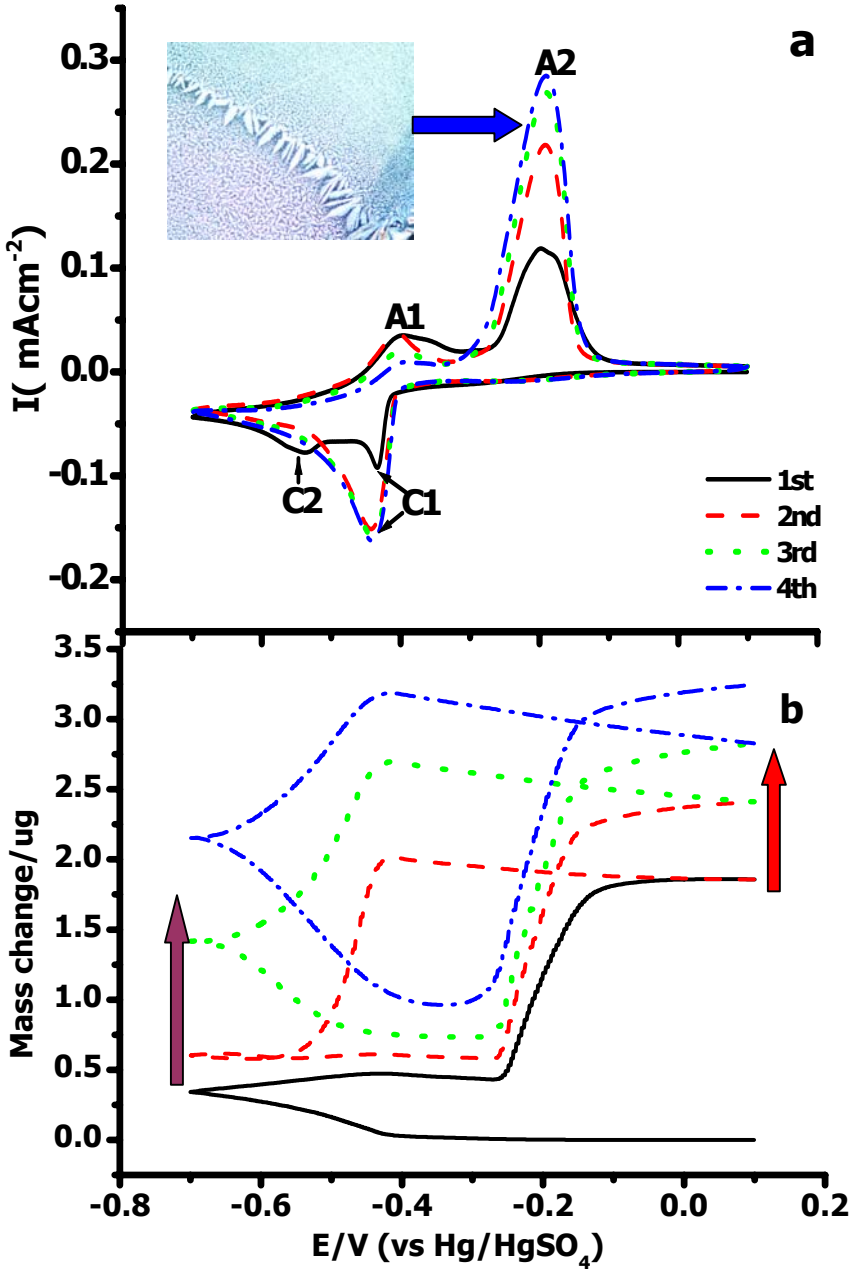

Figure 4.3: a) multiple CVs in 2mM $CuSO_4$/0.1 M K_2SO_4 pH 5 solution on Pt ; b) mass response corresponding to CVs of a in 2mM $CuSO_4$/0.1 M K_2SO_4 pH 5 solution on Pt. The insert optical picture was taken after multiple CVs in 2mM $CuSO_4$/0.1 M K_2SO_4 pH 5 solution.

changes, the obvious differences from pH 1, 2, 3 solution are: 1) in pH 5 and 6 solution, the 1st CV has two reduction peaks, but in 2nd and 3rd CVs, the two peaks merge into one in cathodic region. 2) In anodic region, there are two obvious oxidation peaks showing up. Especially, in pH 5 and 6 solutions, the second anodic peak (A2) keeps increasing and becomes very dominant with CV cycling. Contrarily, the first anodic peak (A1) keeps "shrinking".

Cyclic Voltammetry (CV) was combined with *in situ* EQCM mass response shown as Figure 4.3, Figure 4.3-a shows multiple CVs collected on a freshly cleaned Pt in 2mM $CuSO_4$ /0.1M K_2SO_4 solution in the laboratory atmosphere, pH was adjusted to 5 by adding 3M NaOH, The CV scans started from open cuicurt potential (OCP), about -0.1V, and moved negative to let Cu^{2+} ions to be reduced and deposited on Pt electrode surface. In cathodic range, the first cathodic peak shows up at -0,44V (C1), the second one at -0.55 V (C2). On reverse anodic scan Cu species (Cu^0 and Cu_2O) were oxidized and stripping off from Pt electrode surface, the first anodic peak is at about –0.41V (A1), the second one at about -0.2V (A2). The figure 4.3-b is *in situ* EQCM mass response corresponding to the CVs in Figure 4.3-a. The CVs behavior is obviously different from those collected in lower pH solution we presented previously [14]. In the 1st CV, there were two well defined cathodic peaks, C1 and C2 as labeled in Figure 4.3-a, also two well defined anodic peaks A1 and A2 show up in anodic range, the interesting point is: with second, third and fourth CV running in cathodic range, C1 becomes bigger, C2 visually gets disappear (probably a small C2 merge into the bigger

C1); in anodic region, A1 keeps decreasing and A2 keeps increasing. EQCM data (mass vs applied potential) shows: In the 1st CV scan, there is a mass gain at both C1 and C2 and a slight mass dumping at A1, then followed by a huge mass gain at A2. Starting from 2nd CV, there is big mass dumping even in the cathodic potential region, about -0.42V as shown in Figure 4.3-b.

Blue-Greenish-Precipitate (BGP) was observed on the Ru electrode after finishing three CVs as shown in Figure 4.3-a –the inserted optical image, which was taken under microscope (the similar BGP was seen on the Pt electrode, not show here). BGP has a very well crystallized structure, it is consistent with the basic copper sulfate deposit reported in the literature.[18] Figure 4.4-a is the picture taken on the sample prepared by scanning from OCP (~-0.1V) to C1 (-0.44V) on Ru electrode in 2mM $CuSO_4$/0.1M K_2SO_4 pH5 solution. The reddish particles were visually observed on Ru electrode surface. The shape of the particles is rectangular or triangular using highest magnification ($\times$1000) under optical microscope and SEM as shown in figure 4.4 –a&b. The similar observation was reported by Lee.[19] Figure 4.4-c and figure 4.4-d are the optical pictures taken under microscope after 1 CV and 3 CV respectively on Ru in 2mM CuSO4/0.1M K_2SO_4 pH5 solution. The optical picture inserted in d was taken by using dark field under microscopy.

The XRD data (Figure 4.5) collected on BGP clearly shows that the crystal structure matches very well with reported posnjakite ($CuSO_4(OH)_6.H_2O$).[20,21] Posnjakite ($Cu_4SO_4(OH)_6.H_2O$) is not stable in air. It is stable in the solution, but

it can be easily become dehydrated in air. Even at room temperature, Posnjakite will gradually change to bronchantite ($Cu_4SO_4(OH)_6$). Figure 4.5-a is XRD spectrum

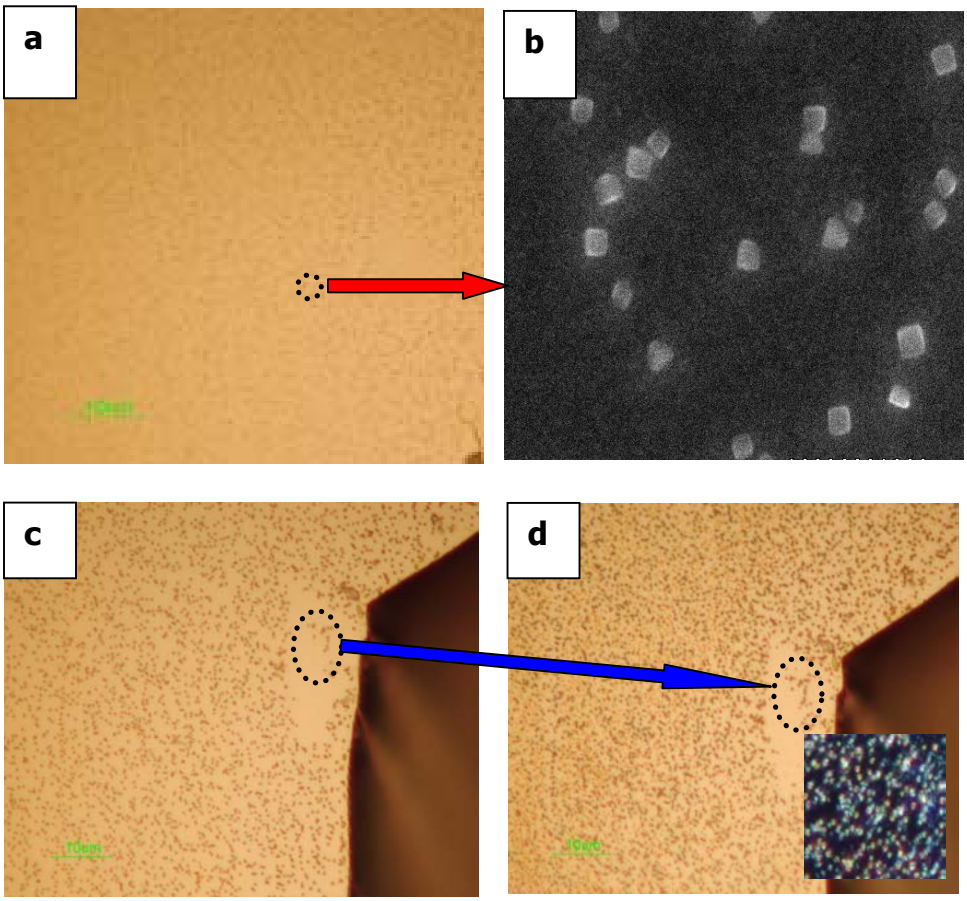

Figure 4.4: Optical pictures (a, c and d) and SEM image(c) on Ru: a) OCP scanning to C1 in 2mM $CuSO_4$/0.1 M K_2SO_4 pH 5 solution on Ru; b) SEM image by rooming in a part of sample a; c) after 1 CV cycle in2mM $CuSO_4$/0.1 M K_2SO_4 pH 5 solution on Ru; d) after 3 CV cycles in 2mM $CuSO_4$/0.1 M K_2SO_4 pH 5 solution on Ru. The inserted optical picture in d was taken by using dark field under microscopy.

of the fresh sample, which was just taken out from solution. There is only posnjakite in BGP deposit, but after exposure in air for four weeks, as shown in Figure 4.5-b, some of posnjakite was transformed to bronchantite. This is in agreement with the observation of Watanabe.[20] Watanabe and coworkers studied Cu corrosion process on Cu plate exposed in urban, rural/coastal and hot spring area in Japan. They found the initially formed posnjakite would change to bronchantite after further exposure.

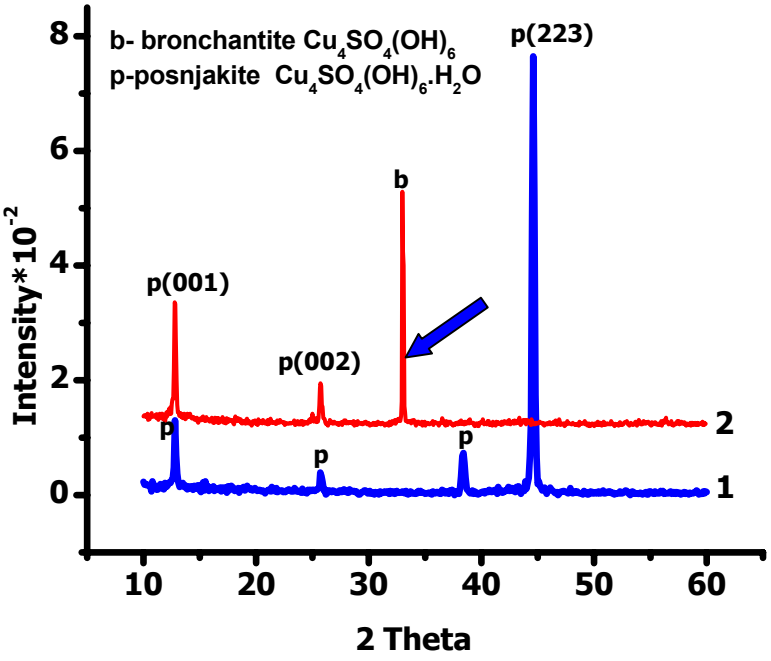

Figure 4.5: XRD spectrum of blue white precipitate formed in 2mM $CuSO_4$ +0.1 K_2SO_4 pH 5 solution on Ru by running CVs continually: 1) Blue white precipitate taken out from solution; 2) Blue white precipitate exposed in air about one month.

XPS is a valuable complement technique to Echem for identifying the actually surface chemical composition formed at certain condition on electrode. Figure 4.6-a is an XPS (Cu 2p) spectrum collected on sample prepared by polarizing at C2 (-0.55v) for 3min to identify what was formed at C2. Similarly, Figure 4.6-b is used to examine what was formed at C1 (-0.44V). Figure 4.6-c is an XPS (Cu 2p) spectrum of BGP formed on Ru. Figure 4.7 is the S 2p (168.53 ev) region on the same BGP sample as Figure 4.6-c.

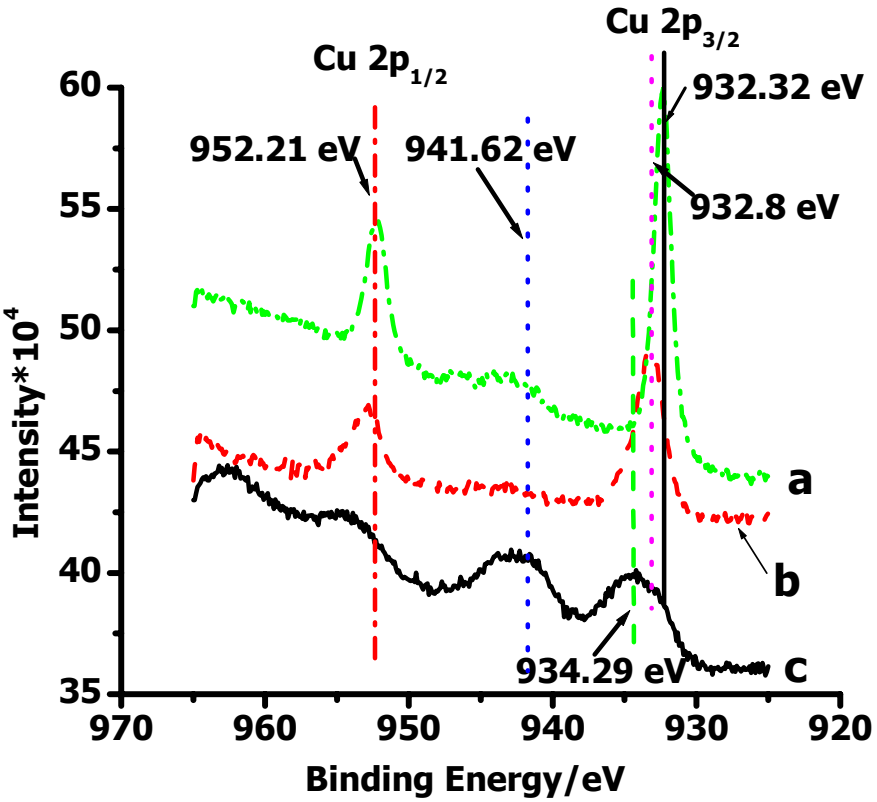

Figure 4.6: XPS spectrum of Cu 2p for compounds formed in 2mM $CuSO_4$ +0.1 K_2SO_4 pH 5 solution on Ru: a) holding at C2 for 3min; b) holding at C1 for 3min; c) Blue greenish precipitate formed by repeated cycling on Ru.

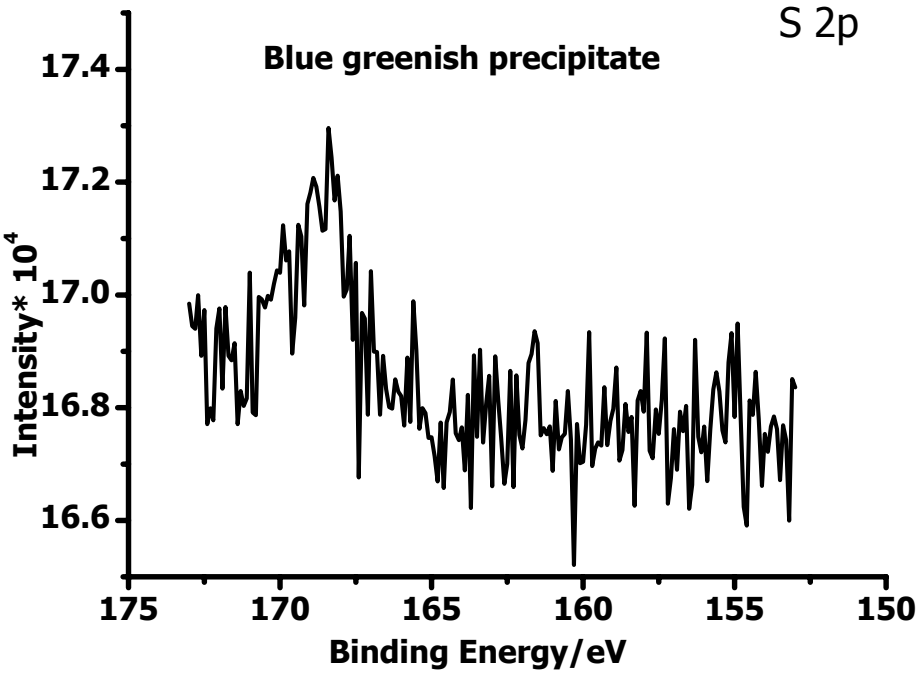

Figure 4.7: S 2p XPS spectrum of blue greenish precipitate.

Effect of Argon (Ar) purging on the CV shape and mass change was investigated, as shown in Figure 4.8. Figure 4.8-a is 4 CVs done on Pt electrode; a positive pressure of Ar was maintained over the solution during this experiment. Figure 4.8-b is *in situ* EQCM mass change corresponding to the CVs in Figure 8-a. We observed that C1 decreased and C2 increased with Ar purging; in the reverse anodic scan, A1 keep increase and A2 keep decrease. There is about 0.5 μg mass gain at A2 in the 1st CV. In 2nd and 3rd cycle, mass gain keeps decrease. Eventually, in the 4th CV, the mass gain at A2 became 0g.This trend is obviously opposite to the trend shown in Figure 4.3-a, which was collected in the laboratory atmosphere.

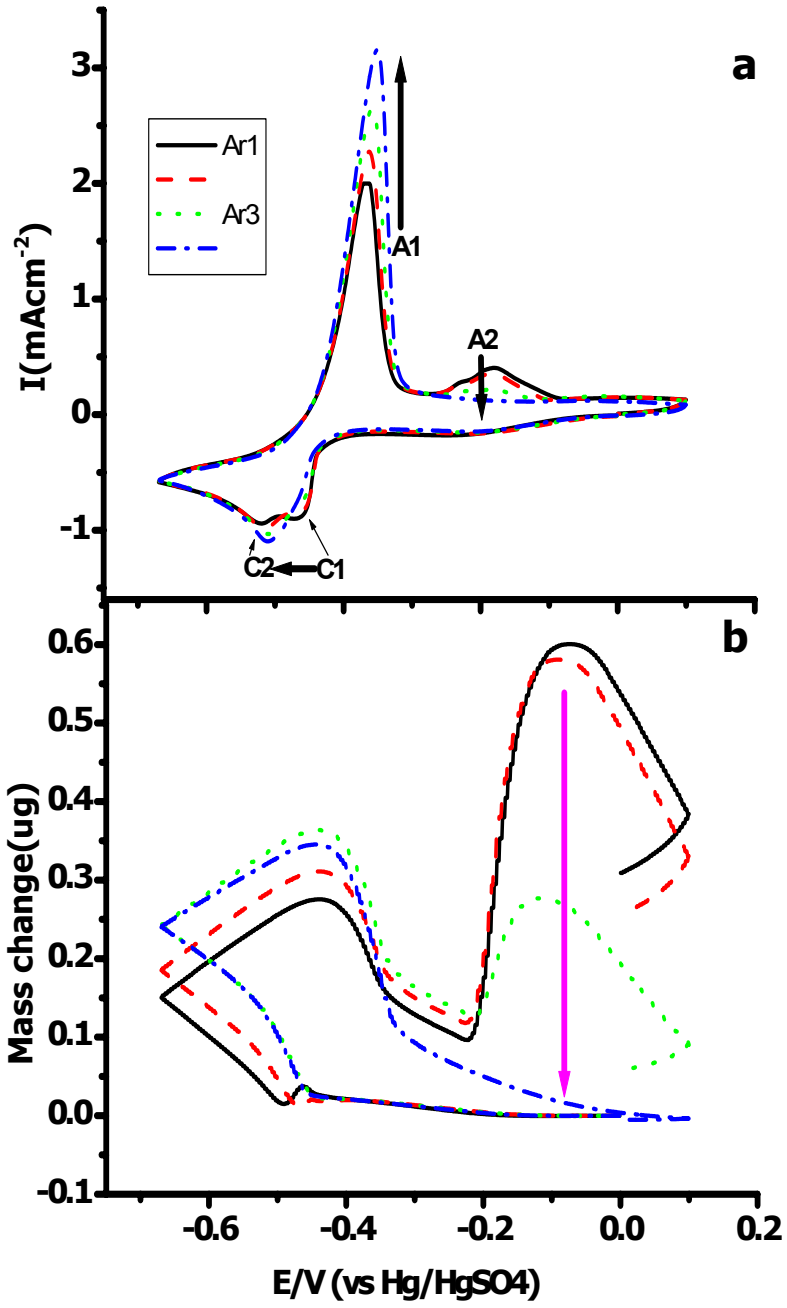

Figure 4.8: Ar purging: a) 4 CVs progressively in 2mM $CuSO_4$/0.1 M K_2SO_4 pH 5 solution on Pt, 20mv/second; b) mass response to 4CVs of a in 2mM $CuSO_4$/0.1 M K_2SO_4 pH 5 solution on Pt.

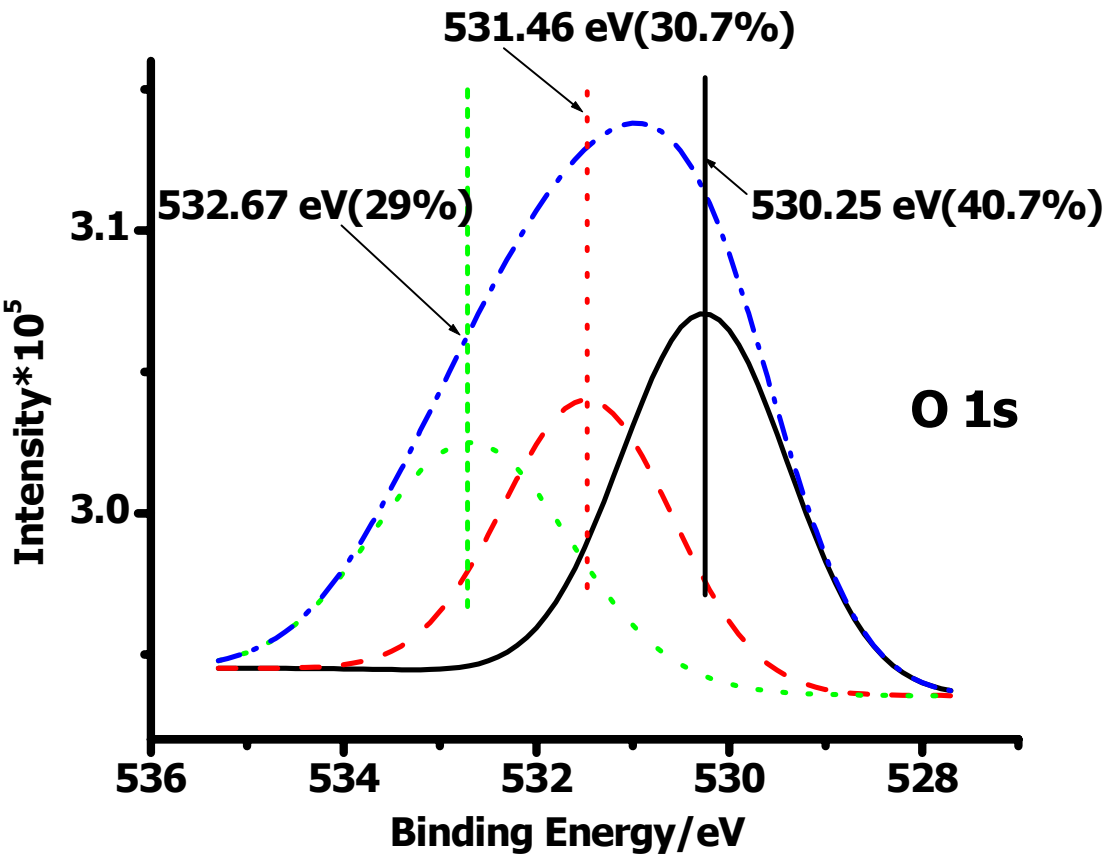

Figure 4.9: XPS spectrum of O 1s on sample prepared by holding at 0.44V for 3min.

4.4 Discussion

Previously we investigated the Ru and Ru oxide electrochemical (Echem) behavior in 2mM $CuSO_4$/0.5M H_2SO_4 (pH ≅ 0). [14] The result of the study on Ru and Pt electrodes Echem behavior in pH5 solution is considerably different from that in very acidic solution.[22] With the help of XPS, SEM, XRD and combination of CV and EQCM, we can well understand the Echem mechanism.

4.4.1 Characterization of Chemicals Formed at C1, C2 and BGP

The peak position of Cu $2p^{3/2}$ in XPS data in Figure 4.6-a is 932.32 eV; it provides evidence that the Cu is formed at C2.[23] In the Figure 4.6-b, the peak position is 932.8 eV, and optical color is reddish and the shape of the partials is rectangular or triangular. The observation is consistent with Switzer and Lee's as mentioned previously.[3, 5,19] This proves that the compound formed at C1 is likely Cu_2O, the peak position matches the report in the literature.[24, 25] In the O1s region as shown in Figure 4.9, there are three peaks, 530.25 eV, 531.46 eV and 532.67 eV. The first one belongs to Cu_2O, [25,26] and the third one is from the adsorption H_2O. We suggest the second one belongs $Cu(OH)_2$, [27,28] which comes from two possible sources: 1) $Cu(OH)_2$ formed in local area near electrode surface due to Oxygen Reduction Reaction (Cu^{2+}/ $Cu(OH)_2$), which will be discussed in detail latter; 2)$Cu(OH)_2$ formed by oxidizing an intermediate in the process of Cu_2O formation(CuOH/ $Cu(OH)_2$) as shown in sketch drawing of Figure 4.10. Thus, we concluded that Cu_2O is forming first at C1 (~ -0,44 V). The size of the Cu_2O particles was measured under microscope, which was about 0.2 um and independent on Cu^{2+} ion concentration. We found that the size of Cu_2O was not changed in solution with different Cu concentration (2mM, 5mM and 10mM), only the density was changed: the higher the concentration was, the denser Cu_2O was deposited on the Pt or Ru electrode.

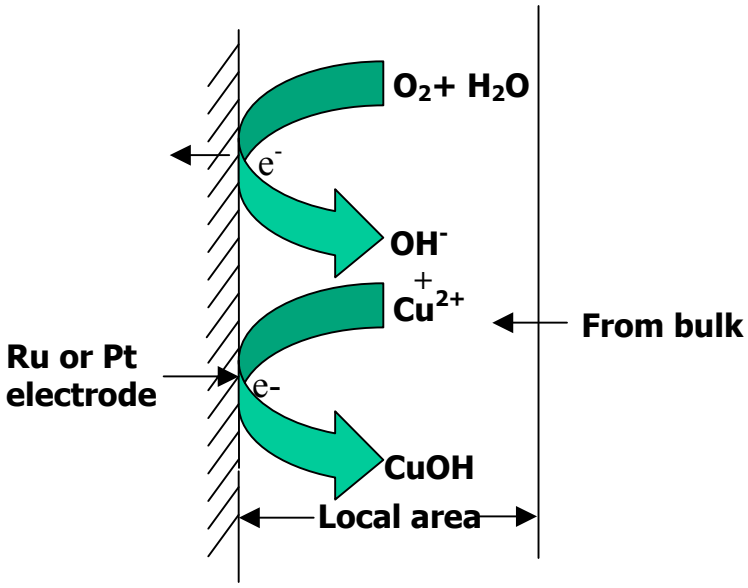

Figure 4.10: Sketches drawing of Local area around Ru or Pt electrode surface.

The BGP formed on the Ru electrode was identified by XPS and XRD, Figure 4.5 confirms that BGP is $Cu_4SO_4(OH)_6.2H_2O$-posnjakite, it matches very well with the literature.[20,21] Also the XPS data collected on BGP is consistent with XRD data. Cu $2p_{3/2}$(934.29 eV) in Figure 4.6-c is the evidence that Cu oxidation state is Cu^{2+} in BGP. According to the literature,[24] this peak can be assigned to $Cu(OH)_2$. S 2p (168.53 eV) showed that the S belongs to SO_4^{2-}, which is agreement with the literature.[20, 23,29]

4.4.2 Mechanism of the Electrochemical Reaction on Electrode

In cathodic region, C1 has been associated with the formation of Cu_2O shown as equation 1. This was confirmed by the XPS data of the Ru sample polarized at C1 (-0.44V) for 4min (Figure 4.6-b). It is in agreement with King's

observation when he studied Oxygen Reduction Reaction) ORR on Cu in neutral NaCl solution.[30] When scanning to C2, the Cu (0) was formed $Cu^{2+}/Cu^{(0)}$ shown as equation 2. Cu was confirmed by the XPS data shown in Figure 4.6-a. The mechanism is different from literature, which studied in basic solution. Both Abrantes[31] and Gewirth[32] thought Cu (0) was formed by continuously reduction of Cu_2O or CuOH at C2 in basic solution. In our study, if the Cu was formed by reduction of Cu_2O formed at C1, C2 should proportionally increase with C1. The fact is when C1 becomes bigger; C2 visually disappears, as shown in Figure 4.3-a. The reason to cause this difference probably is the pH difference of solution. They used very basic solution (pH=12-13), but we worked pH 5 solution.

In the reverse anodic scan, the 1st peak A1 can be assigned to the Cu oxidizing to Cu^{2+} based on the mass change of *in-situ* EQCM data. 2nd peak (A2) is associated with Cu_2O oxidation to $Cu(OH)_2$, This is in good agreement with literature.[24,32,33] As for the assignment of A1, it is different with the literature,[32] which reported Cu/Cu_2O or CuOH at A1 in basic solution. There is a general agreement that the initial species on Cu electrode is cuprous oxide formation in basic electrolyte. Gewirth[32] proved the A1 should be Cu/Cu_2O oxidation by using CV combined with Atomic Force Microscopy (to get force spectroscopic). In our experiment, as observed in *in-situ* EQCM data shown in Figure 4.3-b. There is a mass loss at A1. Thus, we think it should be Cu/Cu^{2+}. Mass loss is due to dissoluble Cu^{2+} formed on the surface of electrode. If undissolved Cu_2O was formed, there should be mass gain at A1. The reason causing this difference is

probably that Cu_2O is more favored forming in highly basic solution. PH of the solution in the literature is 13, and they worked on Cu electrode, which is different from ours- pH 5, Ru or Pt electrode. Thus, we proposed following reaction took place on the surface of Ru or Pt electrode in 2mM $CuSO_4$ +0.1 K_2SO_4 pH 5 solutions.

C1: $2Cu^{2+} + 2e + 2OH^- = Cu_2O + H_2O$ (1)

C2: $Cu^{2+} + 2e^- = Cu$ (2)

A1: $Cu = Cu^{2+} + 2e^-$ (3)

A2: $Cu_2O + 2H^+ = 2Cu^{2+} + H_2O + 2e^-$ (4)

$Cu^{2+} + 2OH^- = Cu(OH)_2$ (5)

4.4.3 Local pH Change due to Oxygen Reduction

We believed that oxygen is a key factor to affect CV shape in pH5 solution. Oxygen reduction reaction (ORR) happened on the surface of Ru or Pt electrode as shown in equation 6. This causes the pH around the surface of electrode (local area, 25-30 um adjacent to electrode) to increase.[30] King and coworkers reported the local pH value could reach 10. Park and his coworkers reported the pH value could reach 12 in aerated NaCl due to ORR by using the electrochemical pH microsensor.[34] Zerbino and Mele investigated the oxygen effect on oxide formation on Cu in borax solution (pH9). [35] We think that the local pH increase is the trigger to form Cu_2O, because the thermodynamically favored reduction process is formation of Cu metal at low pH as equation 2; at

higher pH, the formation of Cu_2O would be favored as equation 1. This is consistent with what Switzer's group observed.[36,37]

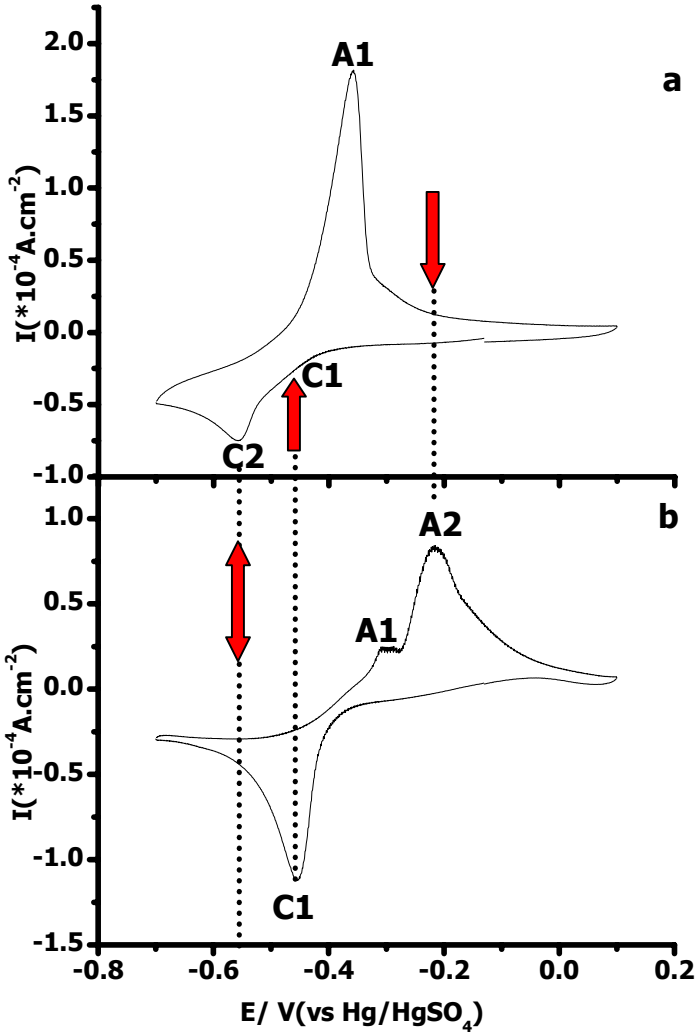

Figure 4.11: CV plots on Ru in 2mM $CuSO_4$ +0.1 K_2SO_4 pH 5 solution a) in pH 5 buffered solution-Acetic acid/Sodium acetate a; b) no buffered. Scanning rate is 20mV/s.

$$O_2\,(g) + 2\,H_2O + 4\,e^- = 4\,OH^- \qquad (6)$$

Local pH increase caused by ORR is very important for Cu_2O formation. Lee reported that Cu_2O can be formed in pH 4.7 solution[19], and he conjectured that maybe it is because of local pH increase due to equation 6 without direct evidence. In our study, this was confirmed by the experiment of using buffered pH 5 solution as shown in Figure 4.11. There is no C1 but an obvious big C2 at cathodic region and a huge A1 but no A2 was observed at anodic region in pH5 buffered solution (Figure 4.11-a). In the unbuffered solution, we obtained an opposite result shown in Figure 4.11-b. Thus, obviously, in buffered solution, the OH^- from ORR was neutralized immediately. So the local area is always acidic. Formation of Cu is favored in this case. This strongly supports that the local pH is likely a key to C1 (Cu_2O formation) and A2 (Cu_2O oxidation). Figure 4.8 is Ar purging experiment, Ar was blowing on the top of the solution and a positive pressure was maintained on the surface of solution to let O_2, dissolved in the solution, to be slowly driven off. CVs were collected and *in-situ* EQCM mass change was performed at the same time. At cathodic region, C1 (Cu_2O formation) keeps decrease, but C2 (Cu formation) gradually increases, eventually C1 disappears. In anodic region, A1 (Cu/Cu^{2+}) increases, but A2 ($Cu_2O/Cu(OH)_2$) gradually decreases, eventually both C1 and A21 disappear. During this process, the O_2 concentration becomes less and less, even there is limited OH^- forming due to the trace ORR, which will not significantly affect pH of local area much. The local pH still keeps acidic. So there is no C1 and A2 at all. The CV is simplified as just Cu^{2+} reduction (C2) and Cu oxidation (A1) as shown the 4^{th} CV

in figure 4.8-a. Thus, we believe whenever the local pH increases and reaches a certain pH value (caused by ORR), even with a weak acidic bulk solution, Cu_2O can be formed on the electrode surface. There is a proton concentration gradient

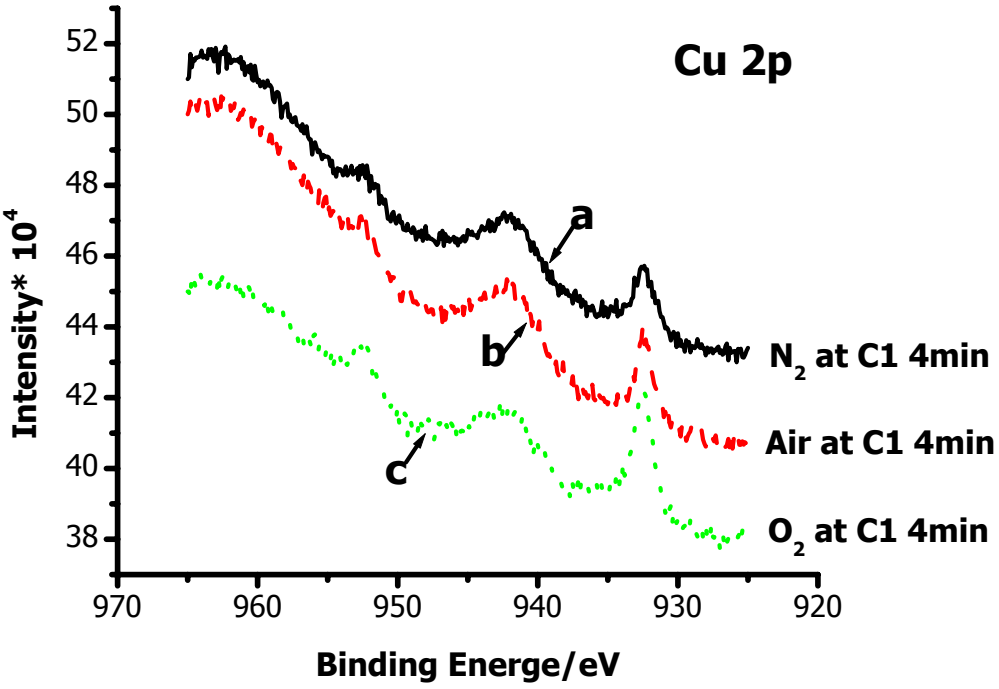

Figure 4.12: XPS spectrum of Cu 2p of compound formed at C1 (~0.44V for 4min holding) on Ru a) N_2 purge; b) in atmosphere; c) O_2 purge.

profile between local area and bulk solution. Protons diffuse from bulk to local area. The higher concentration of proton in bulk (lower pH value), the faster the OH^- in local area can be neutralized, the local pH gets less chance to increase. That is the reason why there is seldom report about that Cu_2O was observed in low pH value solution (less than 1).

Figure 4.12 provides another evidence for the importance of ORR. It is XPS (Cu 2p) data of Cu_2O formed at C1 (-0.44v) in 2mM $CuSO_4$ +0.1 K_2SO_4 pH 5

solutions with different gas purging. By comparing the peak intensity(Cu $2p^{3/2}$), we found that only a little bit Cu_2O was formed in N_2 purging solution, but we can get more Cu_2O in O_2 purging solution, It is obviously that the intensity of Cu2p3/2 keeps increasing on samples (Ru electrode) prepared in: a) N_2 purging; b) air; c) O_2 purging solution. This proves that ORR would strengthen Cu_2O formation in O_2 rich solution due to local pH increase.

As we proposed above, the A2 is Cu_2O/Cu^{2+}oxidation. The source of the Cu_2O, which will be oxidized at A2, comes from C1. This can be confirmed by the experiment shown in Figure 4.13. The A2 becomes bigger and bigger with

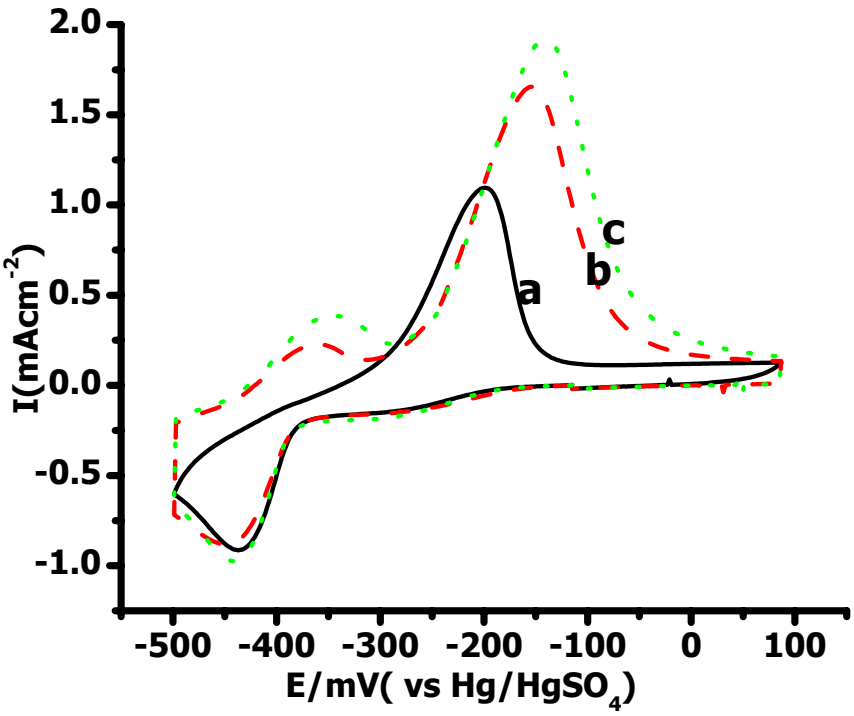

Figure 4.13: CVs of Ru electrode in 2mM $CuSO_4$ +0.1 K_2SO_4 pH 5 solution a) no holding at –0.5, b) holding at –0.5V for 30s; c) holding at –0.5V for 60s.

increasing polarizing time at –0.5v. As shown in Figure 4.3-a, Whenever C1 shows up, A2 will appear, and A2 will increases proportionally with C1 increasing. This observation matches well with the mechanism we proposed above.

4.4.4 Patination- Posnjakite Formation [$Cu_4SO_4(OH)_6.H_2O$]

Interestingly, we get $Cu_4SO_4(OH)_6.H_2O$-posnjakite on Pt or Ru electrode surface visually after collecting a few CVs in 2mM $CuSO_4$/0.1M K_2SO_4 ph 5 solution, which was confirmed by XRD and XPS. Mass change in EQCM data shows that there is always a huge mass gain while potential scans through A2 in anodic region as shown in Figure 4.3-b or Figure 4.8-b. So we think that posnjakite is formed at A2. For posnjakite formation, the Cu_2O formation at C1 is very important as discussed before. It cannot directly be formed from Cu, Cu_2O should first be formed, then posnjakite can be formed at A2.[33, 38] We propose the mechanism of posnjakite formation in our study:

$$3Cu(OH)_2^{*}+Cu^{2+}+SO_4^{2-}+ H_2O \rightarrow Cu_4SO_4(OH)_6.H_2O \qquad (7)$$

* $Cu(OH)_2$ is formed at A2 through equation 4 and 5.

Posnjakite is usually formed in a natural Cu corrosion process-patination, which has been studied extensively.[33, 39-43] Copper is a common material applied not only in electronic parts and devices but also for artistic and architectural

applications. Researchers have artificially formed in laboratory condition to help understand the patination process in nature. Webster group studied copper pit grown in simulated potable water with some anions such as SO_4^{2-} and they got posnjakite.[39] Rosales group investigated patinas formed by means of electrochemical and analysis techniques on statuary alloy.[44] In our study, the mechanism is very similar to the Cu corrosion process in nature: [33,38,45] first the Cu_2O is formed in the atmosphere, then Cu_2O was oxidized to Cu^{2+} and OH^- concentration would increase due to ORR. If there is SO_2 or SO_3 in the air, it will fall down with rain, at last the posnjakite will be formed on the Cu surface. So we believe that posnjakite is formed in the following way: 1) Cu_2O is formed at C1 (-0.44V) in cathodic range shown as equation 1. 2) Cu^{2+} was formed when applied potential scanned to A2 shown as equation 4. At the same time ORR happened on the electrode causing the local pH to increase and lead that $Cu(OH)_2$ is formed at the surface; 3) Posnjakite is formed through chemical reaction between $Cu(OH)_2$ and Cu^{2+}/SO_4^{2-} shown as equation 7. A part of Cu^{2+} ions source is from the surface of electrode undergoing Cu_2O/Cu^{2+} oxidation as in equation 4, others are from the bulk solution through diffusion process. All the SO_4^{2-} anions are from bulk solution through diffusion process. The whole posnjakite formation process is illustrated in Figure 4.14. Intuitively, the mass gradually increases. Eventually, the posnjakite forming causes a big mass gain at A2. This also is in agreement with the observation in figure 4.4-c (after 1 CV on Ru) and Figure 4.4-d (after 3 CVs on Ru). Looking into the special patch, one can

see that some new particles in Figure 4.4-d are formed around the old particles in Figure 4.4-c. We believe the new particle formation is posnjakite formation. One also can see from the inserted picture in figure 4.4-d that some new particles formed around the old ones.

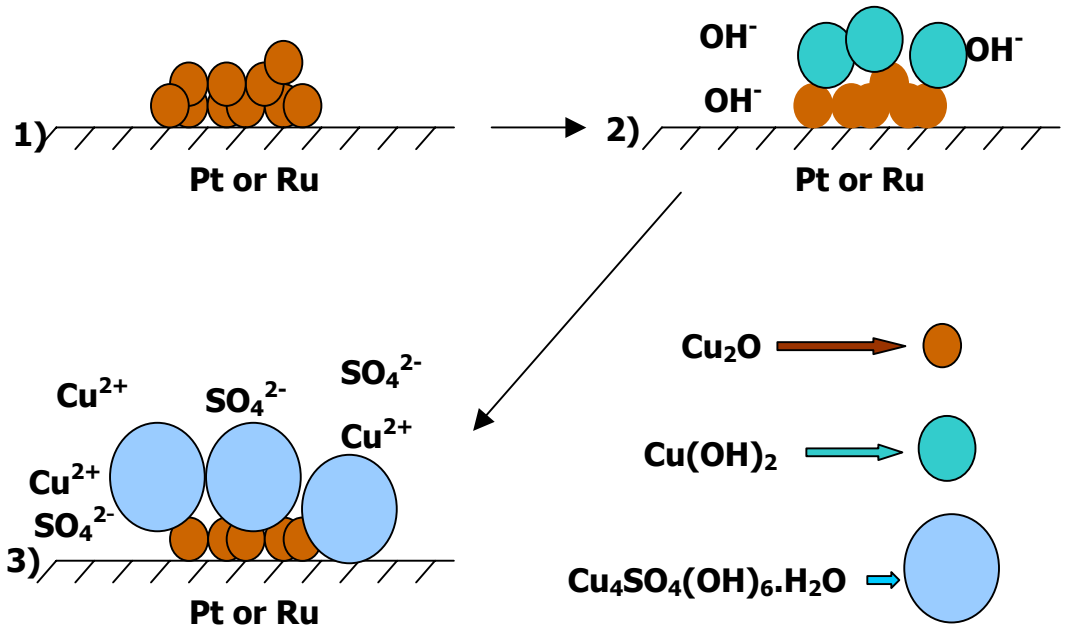

Figure 4.14: Process of posnjakite formation at A2.

In mass change of EQCM data as shown in Figure 4.3-b, a mass dumping was observed at –0.42V in cathodic region starting from 2nd CV, we think there are two possibilities to lead this dumping: (1) "avalanche" caused by depart of chemical species in posnjakite such as SO_4^{2-}, Cu^{2+}, OH^- group. (2) Reduction of posnjakite, it was discomposed around –0.42V, most of them dissolve in solution and cause big mass lose. In our study, we believe most likely it's the second situation. Malvault, J. Y et .al reported the posnjakite can be reduced in cathodic

region.[43] Because we also found there is a bigger C1 starting from 2nd CV as shown in Figure 4.3-a, so we believe there is a part of C1 which is contributed by posnjakite reduction starting from 2nd CV. At the same time, as a product of the reduction, Cu_2O also is formed through it. This is consistent with the change of baseline in EQCM with cycling shown in Figure 4.3-b: the 2rd baseline increased by 74% compared to 1st one, the 3rd one increased by 134% based on 2rd, the 4th one increased by 50% based on the 3rd one. Because when potential scanning through C1, the posnjankite could be reduced to Cu_2O and left on the electrode, so the baselines increase. This is also in agreement with the behavior of mass change at A2, the mass "jumping" at A2 increases with cycling: 1st is 1.41ug, 2nd is 1.80 ug, 3rd is 2.03 ug and 4th is 2.26 ug, that is because more Cu_2O is formed at C1 due to posnjakite reduction.

Since local pH will increase due to ORR, which triggers Cu_2O formation as mentioned above. Why is there no big mass "jumping" at C1 or A1, but only at A2 as shown in Figure 4.3-b or figure 4.8-b? We think that posnjakite formation probably requires a much high pH environment; local pH increase driven only by ORR is not enough. Since the equation 4 is a proton consuming reaction at A2, it will cause local pH further increase to achieve posnjakite formation.[36] So, when potential scanning reaches A2 (~ -0.2V), local pH reaches a higher point due to both ORR and the reaction shown as equation 4. Local pH is high enough for posnjakite formation at that time, and then a huge mass "jumping" is always observed at A2.

4.4.5 EQCM Mass Change Responses to CVs

The combination of CVs and *in situ* mass change in EQCM data supplies a good technique to understand the mechanism. To make it easy to understand the mechanism, we define:

$E_f = (M_a/M_t)* 100\%$

E_f - The efficiency of mass gain or loss.

M_t - Mass gain or loss calculated based on coulombic charge from CVs for the proposed Echem reaction as the *theoretical mass*.

M_a - Mass gotten directly from EQCM as the *actual mass* observed.

In 2mM $CuSO_4$ solution, M_t=0.0308ug, M_a=0.0301ug, the efficiency is 97.7% at A1. It matches very well with the reaction at A1 we proposed in equation 3. With the Cu^{2+} concentration increasing, the efficiency becomes smaller and smaller as shown in table 4.1. In 5mM $CuSO_4$ solution, E_f becomes 81.5%, 10mM $CuSO_4$ solution is 78.2%. What is the reason to cause this change? We believe

Table 4.1:Mass gain or loss at A1 and A2 peak in different Cu concentration solution.

	A1 peak			A2 peak		
	M_t/μg	M_a/μg*	E_f/%	M_t/μg	M_a/μg**	E_f/%
2mM $CuSO_4$	0.0308	0.0301	97.7	0.77	1.38	196.2
5mM $CuSO_4$	0.713	0.582	81.5	0.49	1.56	320.0
10mM $CuSO_4$	1.68	1.31	78.2	0.49	1.56	320.0

* Mass loss (dumping);** Mass gain(jumping).

this is because of following reactions at A1 in higher Cu^{2+} concentration solution:

$Cu + OH^- = CuOH + e^-$ (8); $4CuOH = 2Cu_2O + 2H_2O$ (9)

We think that in 5mM and 10mM $CuSO_4$ solution there are two reactions, Cu/Cu_2O or CuOH and Cu/Cu^{2+} at A1, instead of literature report, [31,32,46] only one reaction (Cu/Cu_2O or CuOH) happened on the surface of electrode. As shown in table 4.1, the efficiency at A1 in 2mM $CuSO_4$ solution is pretty high-97.7%, since all the calculation is based on the mechanism we proposed as equation 3, which infers the reaction at A1 does follow equation 3. With increasing the Cu^{2+} concentration, the efficiency becomes smaller and smaller, because parts of Cu become Cu_2O or CuOH at A1 through the equation 8, 9. The mass will not change much, because they will precipitate on the electrode. But our calculation was based on the Cu/Cu^{2+}, which will lead the change of theoretical mass to increase, and then causes the efficiency to decrease. Thus in higher Cu^{2+} ion pH 5 solution (5mM, 10 mM), there are multiple reactions existing on the surface of electrode at A1, shown as equation 3, equation 8 and 9. Gewirth[32] reported Cu_2O or CuOH without good adhesion with copper electrode surface was formed at A1 (Cu/Cu_2O or Cu(OH)) in 0.1M NaOH solution. In other words, the Cu_2O/CuOH is dissolved in local area. Our EQCM mass change vs applied potential spectrum does not agree with this point in the pH 5 $CuSO_4$ solution. If Cu was formed dissolvable Cu_2O/CuOH species shown as equation 10, the theoretical mass change-M_t should be much higher than the $M_{t,}$ which was calculated from our proposal (Cu/Cu^{2+}) shown as equation 11. Since 1mol electron can only dissolve 0.5 moles Cu for our proposal, but 1mol electron will dissolve 1 mole Cu following Gewirth conclusion in basic solution, so the E_f should be much higher

than 100%, but that is not the case in pH 5 solutions as shown in table 4.1. We believed that undissolved Cu_2O/CuOH is formed on the surface of Ru or Pt electrode in pH 5 solution.

$2Cu \rightarrow Cu_2O$ or 2CuOH(dissolvable) + $2e^-$ (10)

$Cu \rightarrow Cu^{2+}$(dissolvable) + $2e^-$ (11)

Thus, we believe that most of Cu was changed to dissolvable species (Cu^{2+}) in 2mM $CuSO_4$ pH 5 solution and only very small part of Cu was changed to undissolved species (Cu_2O/CuOH) on the electrode surface. With increasing the Cu^{2+} ion of pH 5 solutions, undissolved Cu_2O/CuOH formation will increase. We suggest the difference between literature and our study is caused by pH difference of the solution. Because literature reported that there are two steps in oxidizing Cu to Cu^{2+}: [47]

Step 1: $Cu \rightarrow Cu^+$ (12)

Step 2: $Cu^+ \rightarrow Cu^{2+}$ (13)

Cu^{2+} ions formed by equation 13 are easy to dissolve and can be removed from the local area by diffusion process in 2mM $CuSO_4$ pH 5 acidic solutions. In basic solution, there are a lot of OH^- anions available in the solution; it will follow different mechanism as the literature reported. But even in ph 5 acid solutions, if the Cu^{2*} concentration is too high; more Cu will be formed at cathodic range. When applied potential scans through A1, there is much more Cu^{2+} ions which will be formed in the local area. In 2mM $CuSO_4$ solution, the Cu^{2+} can smoothly diffuse from local area into bulk and let Cu^{2+} continually to be formed at A1, but

for 5mM and 10mM $CuSO_4$, the speed of Cu^{2+} ion diffusion is not fast enough to remove Cu^{2+} formed by equation 13. Cu^{2+} concentration will keep increasing in local area. In this case, Cu^{+} will be thermodynamically favored.

As for mass change of EQCM data at A2, the mass gain of posnjakite is based on the equation 6, and the charge calculation is based on equation 4. In three solutions: 2mM, 5mM and 10mM $CuSO_4$ solution, the efficiency of posnjakite formation is higher than 100%. This is consistent with the proposal mentioned above. Part of deposited Cu from C2 will be oxidized to Cu^{2+} at A1; so Cu^{2+} ions are abundant in the local area. When scanning to A2, it will thermodynamically favor to form posnjakite precipitate. Actually, the efficiency of posnjakite formation in 2mM CuSO4 is much lower than that in 5mM or 10mM $CuSO_4$ solution, which means Cu^{2+} formed at A1 will keep increasing with Cu^{2+} ion concentration increasing due to the equation 3. Comparing the efficiency of posnjakite formation between 2 mM and 5mM or 10mM $CuSO_4$ solution, we observed the former is lower than the latter. When Cu^{2+} concentration reaches 5mM and beyond, the efficiency of posnjakite formation reaches maximum at 320%, as shown in table 4.1. Probably it's because of chemical transfer limitation. To form posnjakite, other chemical species, such as SO_4^{2-}, should be supplied, not only Cu^{2+}. SO_4^{2-} should be transferred to the local area from bulk solution by diffusion process. When the speed of SO_4^{2-} diffusion cannot keep up with the speed of posnjakite formation, the maximum efficiency will be reached, no matter how many Cu^{2+} ions available in the local area. Another possible reason is

the OH^- anions from ORR are also limited. This proposal is in agreement with the data shown in Figure 4.15. Mass gains at A2 in the 1st CV in 2mM 5mM and 10mM pH 5 $CuSO_4$ solutions are almost same.

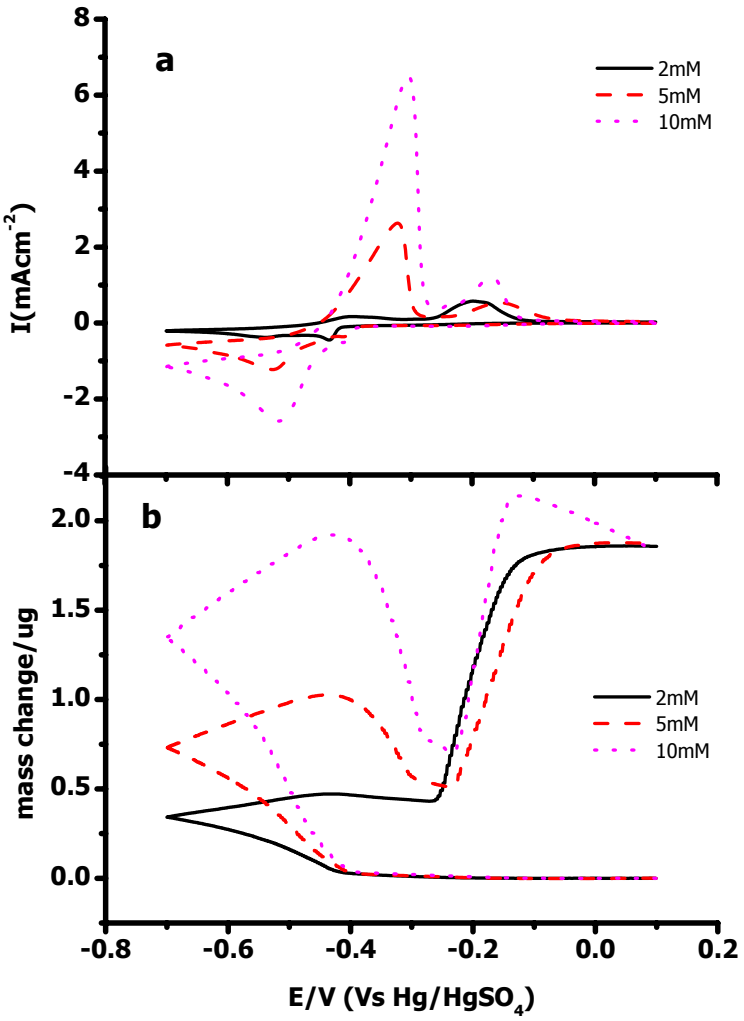

Figure 4.15: The 1st CV with mass change (EQCM) spectrum in 2mM, 5mM and 10mM Cu SO_4/0.1M KCl pH 5 solution.

As mentioned previously, the C1 directly corresponds to A2, the Table 4.2 shows their charge relationship. In each of the multiple CVs, the charge of A2 peak is always bigger than the charge of C1 peak. This provided another

Table 4.2: Charge of C1 and A2 for each cycle in multiple CVs on Pt in 2mM $CuSO_4$/0.1M K_2SO_4 (pH5)

	Charge at C1/mC	Charge at A2/mC
1st scan	0.10	0.43
2nd scan	0.63	0.78
3rd scan	0.71	1.0
4th scan	0.76	1.2

evidence of the above-mentioned proposed mechanism. The charge consumed at A2 comes from both the Cu_2O formed at A1 and Cu_2O formed at C1. The ORR role in our study was confirmed by CV-EQCM combination shown as figure 4.8 and table 4.3. With the Ar purging, the charge measured at A1 in CV increases,

Table 4 3: Charge and mass change at A1 and A2 in Ar purging experiment – 4 CVs in 2mM $CuSO_4$/0.1M K_2SO_4 (pH5) with Ar purging.

	A1		A2	
	Charge change/mC	Mass change/μg*	Charge change/mC	Mass change/μg**
1st CV	0.59	0.14	0.105	0.50
2nd CV	0.65	0.16	0.039	0.46
3rd CV	0.77	0.2	0.017	0.15
4th CV	0.95	0.25	0	0

* Mass loss (dumping);** Mass gain(jumping).

which infers Cu deposition is favored in cathodic range where pH is kept in acidic range because ORR became very small, This is in agreement with the observation at cathodic range: C1(Cu^{2+}/Cu_2O) becomes smaller and visually

disappears at last, but C2(Cu^{2+}/Cu) become bigger and bigger with Ar purging. Charge of A2 became smaller and smaller, and eventually, it becomes 0. On the other hand, the Cu_2O formation is limited with Ar purging in cathodic range. This is consistent with the mass change in EQCM data. Mass change at A2 becomes smaller and smaller and becomes 0 gram at last.

4.5 Summary

In this chapter, we explored the Ru's electrochemical behavior in different pH solution systematically, and found there is an obvious difference between low pH($\leq$ 3) and high pH ($\geq$4) solution. We studied the Pt and Ru Echem behavior by CV only in 2mM $CuSO_4$ +0.1 K_2SO_4 pH 5 solutions and get apparent different CV plots compared to pH 0 solution. A mechanism is proposed with the help of XPS, SEM, XRD and combination of EQCM and CV. The *in-situ* EQCM combined with CV is a powerful tool for explanation and confirmation of the mechanism.

In 2mM $CuSO_4$ +0.1 K_2SO_4 pH 5 solution on Pt or Ru electrode, the C1 is Cu_2O formation (Cu^{2+}/Cu_2O), it is triggered by local pH increase, and ORR causes local pH to increase. Cu metal is formed at C2. In anodic region, Cu is oxidized (Cu/Cu^{2+}) at A1, A2 peak is Cu_2O oxidation (Cu_2O/$Cu(OH)_2$). Posnjakite was observed on the electrode. It is formed by the following reaction.

$3Cu(OH)_2+Cu^{2+}+SO_4^{2-}+ H_2O \rightarrow Cu_4SO_4(OH)_6.H_2O$

4.6 References

1) Jay A. Switzer, Chen-jen Huang, Ling-yuang Huang, Eric R. Switzer, Daniel R. Kammler, Teresa D. Golden and Eric. W. Bohannan. *J. Am. Chem. Soc.*, **120**, 3530 (**1998**).

2) Ling-yuang Huang, Eric. W. Bohannan, Chen-jen Huang, and Jay A. Switzer. Israel *Journal of Chemistry,* **37**, 293 (**1997**).

3) Run Liu. Fumiyasu Oba, Eric. W. Bohannan, Frank Ernst and Jay A. Switzer. *Chem. Mater*. **15**, 4882 (**2003**).

4) Run Liu, Eric. W. Bohannan and Jay A. Switzer. *Applied Physics Letters*. **83** (10), 1944 (**2003**).

5) Jay A. Switzer, Hiten M. Kothari and Eric. W. Bohannan. *J. Phys. Chem. B.* **106**, 16 (**2002**).

6) S. Leopold, I. U. Schuchert, J. Lu, M. E. Toimil Molares, M. Herranen and J. -O. Carlsson, *Electrochimica Acta,* **47**(27), 4393 (**2002**).

7) D. K. Zhang, Y. C. Liu, Y. L. Liu and H. Yang, *Physical B: Condensed Matter,* **351**(1-2), 178 (**2004**).

8) International Technology Roadmap for Semiconductor -2002 Update, Semiconductor Industry Association (**2002**), pp. 74-75; see http://public.itrs.net/

9) You-Lin Wu, Yi-Cheng Hwang, *Thin Solid Film,* **461**, 294 (**2004**).

10) W.C. Gau, T.C. Chang, Y.S. Lin, L.c. Hu, L. J. Chen, C.Y. Chang, C.L.Cheng *J. Vac. Sci. Technol., A,* **18** (2), 467 (**2000**).

11) S. Hartinger and K. Doblhofer, *Journal of electroanalytical Chemistry*, **380**, 185 (**1995**).

12) M. H. Holzle, C. W. Apsel, T. Will and D. M. Kolb, *Electrochem. Soc.* **142**(11), 3741 (**1995**).

13) O. Chyan, T. N. Arunagiri and T. Ponnuswamy, *J. Electrochem. Soc.,* **150**, C347 (**2003**).

14) Y. Zhang, L. Long, T. N. Arunagiri, O. Ojeda, S. Flores, O. Chyan, R. M. Wallace, *Electrochem. Solid-State Lett.* **7** (9), C107 (**2004**).

15) Saurbrey, G.Z., Z. *Phys.* **155**, 206 (**1959**).

16) Hepel, M., *Electrode-Solution Interface Studied with Electrochemical Quartz Crystal Nanobalance*, in *Interfacial Electrochemistry: Theory, Experiment and Application.*, A. Wieckowski, Editor. Marcel Dekker: Postdam. p. 599-629 (**1999**).

17) Lu, C., *Applications of Piezoelectric Quartz Crystal Microbalances*, in *Methods and Phenomena: Their application in Science and Technology.*, C. Lu; and A.W. Czanderna, Editors., Elsevier Science: Amsterdam. p. 393 (**1984**).

18) http://webmineral.com/data/psnjakite

19) Jaeyoung Lee and Yonggsug Tak, *Electrochemical and Solid- State letter*. **2**(11), 559 (**1999**).

20) Masamitsu Watanabe, Masato Tomita and Toshino, *J. Electrchem. Soc.*, **148** (12), B522 (**2001**).

21) K. P Pitzgerald, J. Nairn and A. Atrens, *Corrosion Science*, **40** (12), 2029 (**1998**).

22) A.I. Danilov , E.B. Molodkina , Yu.M. Polukarov , V. Climent ,J.M. Feliu *Electrochimica Acta* , **46**, 3137 (**2001**).

23) Handbook of X-ray photoelectron spectroscopy, by CD Wagner

24) Wolfgong Kautek and Joseph G. Gordon 11, *J. Electrochem. Soc*. Vol. **137** (9), 2672 (**1990**).

25) N. S. Mclntyre and M. G. Cook, *Analytical chemistry*, **47** (13) 2008 (**1975**).

26) C. A. N, Fernando, P. H. C. de Sila, S. K. Wethasinha, L. M. Dharmadasa, T. Delsol, M. C. Simmonds, *Renewable Energy,* **26**, 512 (**2002**).

27) Kavita Borgohain, Norio Murase, Shailaja Mahamunia) *J. Appl. Phys*., **92** (3), 1292 (**2002**).

28) Haixia Dai,Corrine K. Thai,Mehmet Sarikaya, Franc¸ois Baneyx,and Daniel T. Schwartz, *Langmuir,* **20** (8), 3483 (**2004**).

29) Zhongyuan Dang, Jingfang Gu and Ling Yu, *Applied Catalysis*. **63**, 256 (**1990**).

30) F. King, M.J. Quinn, C.D. Like, *Journal of electroanalytical Chemistry,* **385**, 45 (**1995**).

31) A. C. Cascalheira and L.M. Abrantes, *Electroimica Acta,* **49**, 5023 (**2004**).

32) Myungchan Kang and Andrew A. Gewirth, *J. Phys. Chem.,* B, **106**. 12211 (**2002**).

33) F. Noil, P. Misaelides, A. Hatzdimitriou, E. Pavlidou and M. Kokkorris, *J. Mater. Chem.* **13**, 114 (**2003**).

34) J.O. Park, C.H. Paid, Y.H. Huang, and R.C. Alkire, *Journal of the electrochemiscal society*, **146** (2), 517 (**1999**).

35) J. O. Zerbino, M.F.L. DE. Mele, *Journal of Applied Electrochemistry,* **27**, 335 (**1997**).

36) Jay A. Switzer, Chen-jen Huang, Ling-yuang Huang, F. Scott Miller, Yanchun Zhou, Eric R. Raub, Mark G. Shumsky and Eric. W. Bohannan. *J. Mater. Res*, **13** (4), 911 (**1998**).

37) Y.C Zhou and Jay A. Switzer, *Mat. Res. Innovat*, **2**, 22 (**1998**).

38) Antonio R. Mendoza, Francisco Corvo, Ariel Gomez and Jorge Gomez, *Corrosion Science*, **46**, 1189 (**2004**).

39) A.G. Christy, A. Lowe, V. Otieno, V. Otieno-Alego, M. Stoll and R.D. Webster. *Journal of Applied Electrochemistry*, **34**, 225 (**2004**).

40) L. Veleva. P. Quintana, R. Ramanaluskas, R. Pomes and Maldonado, *Electrimica, Acta*, **41** (10), 1641 (**1996**).

41) Pollard, A. M. and Thomas, R.G. *Mineralogical Magazine,* **56**, 359 (**1992**).

42) Malvault, J. Y and Lopitaux, *Journal of Applied Electrochemistry*, **25**, 841 (**1995**).

43) R. Schlesinger, H. Klewe-Nebenius and M. Bruns, *Surface and Interface Analysis,* **30**, 135 (**2000**).

44) Gabriela P. CiCileo, Miguel A. Grepo, Blanca M. Rosales, *Corrosion Science*, **46**, 929 (**2004**).

45) S. Jouen, M. Jean, B. Hannoyer, *Surf. Interface Anal*. **30**, 145 (**2000**).

46) Z. Mekhalif, F. Sinapi, F. Laffineur, J. Delhalle, *Journal of electron spectroscopy and related phenomenon,* **121**, 149 (**2001**).

47) J. B. Matos, L. P. Pereira, S.M.L Agostinho, O.E. Barcia, G.G.O Cordeiro, E. D'Elia, *Journal of Electroanalytical Chemistry*, **570** (1), 91 (**2004**).

Chapter 5

Conclusions

Conclusions, which will be drawn from the results reported in the previous chapters (chapter 2, chapter 3 and chapter 4), shall be presented in the following sections. Perspective of the research and some future work will be presented.

5.1 Conclusion from Chapter 2

Cu UPD on the RuO_x formed electrochemically was first observed in 2mM $CuSO_4$. It will be affected by pH of solution, Cl^- anion. With increasing the pH value of the solution, we got completely different result. We think the mechanism of electrode reaction in low pH (< 3) bath is different than in high pH (> 4) bath. Cl^- will affect the Cu UPD and bulk Cu deposition, Cu UPD will appear earlier (more positive potential) in the solution with Cl^- than in the solution without Cl-, and the bulk Cu deposition was inhabited by Cl^-, because the adsorbed chloride is neutral on electrode surface, not like SO_{4-}^{2-} which has charge. So when de-adsorpting Cl to Cl^-, it will consume charge and compete with the reducing reaction for Cu reduction in cathodic range. That makes Cu deposition decreases with increasing Cl^- concentration. Considerable different results were obtained on Echem Ru oxide and thermal Ru oxide. Cu deposition is thermodynamically favored on Ru oxide formed by Echem. All the results are beneficial to guide IC industry to prepare their Cu metal interconnect fabrication.

More investigation of other anions (such as Br^-, I^- anions) effect on RuO_x will be important.

The observation of Cu UPD on Ru and its conductive oxide surfaces has important implications in the Ru-based Cu diffusion barrier application. Previously, we have demonstrated that a 20 nm Ru thin film functions well as a Cu-diffusion barrier after 450 ^oC annealing. However, for the future 45-65 nm integrated circuits devices, the thickness of a functional diffusion barrier is limited to merely 5 nm. In such a ultra-thin non-epitaxial metal film, where grain boundaries and dislocations are abundant and will provide the least energy resistant paths for Cu inter-diffusion. Conceivably, the amorphous conductive ruthenium oxide can be delivered electrochemically to plug the grain boundary diffusion passageways prior to Cu electroplating for maximizing the Ru-based barrier performance. Our current data suggests that both Ru and its conductive oxide can easily receive direct Cu plating. More importantly, strong binding interaction, manifesting by the observed Cu UPD process, exists between Cu and Ru as well as its conductive ruthenium oxide. Our separate scribe and peel tests confirm that stronger interfacial binding does promote excellent Cu adhesion, and that is of critical importance in order to withstand highly demanding chemical-mechanical planarization process during integrated circuits fabrication. Therefore, ultrathin film composed of Ru and its conductive oxides is a promising candidate as a directly platable Cu diffusion barrier for the future metal interconnect application.

5.2 Conclusion from Chapter 3

The results are very promising for the 5nm Ru to be used as an effective Cu diffusion barrier on Si substrate. Our data clearly shows that 5nm Ru is a promising Cu diffusion barrier; because it can successfully block Cu diffusion at 300 ^{o}C anneal process for 10min. The high-resolution TEM combined with RBS data establish the interfacial stability between Cu/(5 nm Ru)/Si after annealed at 300 ^{o}C. High-resolution EELS analyses showing no oxygen reveals an interlayer silicidation process that is attributed to the final break down of 5nm Ru barrier layer. The data suggest that Ru thin film is a good candidate as Cu diffusion barrier for the advanced integrated circuits application.

TEM reveals a less-dense packing morphology of ECD Cu as compared to PVD Cu. Both PVD and ECD Cu/(5 nm Ru)/Si structures retain their interfacial integrity after vacuum annealing at 300 ^{o}C. XPS analyses, after etching removal of Cu overlayer, show that minute ECD Cu could penetrate further into Ru thin film matrix as comparing to PVD Cu. Since electrochemically-plating Cu is cheap and mild for application in IC industry, so the study to improve ECD Cu density will be helpful to ECD Cu plating on 5nm Ru thin film.

As mentioned in chapter 2, since the Ru oxide formed electrochemically can get UPD Cu with stronger bond compared to Ru surface, most important, it can be formed formally. That is very important for application in next generation microelectronics microstructure with high aspect ratio feature. So the future work,

Ru thin film with a monolayer Ru oxide on the top as Cu diffusion barrier will be carried out.

Also, all our Cu diffusion study was performed on the Cu/Ru/Si stack. Si(100) is the substrate. So in the future, similar study on all kinds of ILD substrate (Cu/Ru/ILD) will be of interest to microelectronic industry.

5.4 Conclusion from Chapter 4

We found complete different behavior of Ru electrode in pH 5 CuSO4 solutions compared to the pH 0 solution. The key factor is ORR, which greatly affects the pH value of local area around electrode in pH5 solution. Interestingly, posnjakite can be formed on Ru and Pt electrode in pH 5 Cu bath, and it can be controlled by controlling the O_2 concentration and the applied potential. The mechanism of the reaction happened on Ru or Pt electrode surface is well understood with the help of XPS, SEM, XRD and combination of EQCM and CV.

In 2mM $CuSO_4$ +0.1 K_2SO_4 pH 5 solution on Pt or Ru electrode, the C1 is Cu_2O formation (Cu^{2+}/Cu_2O), which is triggered by local pH increase, and ORR causes local pH increase. Cu metal is formed at C2, In the anodic region, Cu get oxide (Cu/Cu^{2+}) at A1, A2 peak is Cu_2O oxidation ($Cu_2O/Cu(OH)_2$). Posnjakite was observed on the electrode, it formed by the following reaction.

$$3Cu(OH)_2+Cu^{2+}+SO_4^{2-}+ 2H_2O \rightarrow Cu_4SO_4(OH)_6.2H_2O$$

This study has a potential application in artificial patina formation by electrochemical method in making statuary for artist. The ratio of Cu_2O (red color) to posnjakite (blue or green) can be electrochemically controlled. Since

ORR is the key factor to cause all these happening, thus investigation of protecting Ru or Pt surface using anion (such as I^-) will be interesting. Actually. I^- effect on patina formation is ongoing right now in our group.

This study gives us a basic understanding of Ru electrode behavior in high pH acid solution (pH 5). We know the ORR is a critical issue; this study is a good direction for IC industry in the future, avoiding O_2 involvement is very important for Cu plating. Also this study opens a new window for Cu plating. Is it possible to plate Cu in high pH (~5) acid bath, or even at around ph 7? That will make the Cu plating solution milder. Industry does not need to use equipment made of materials with high resistant to corrosion. So manufacturing cost will be reduced. To achieve this aim or to answer the question above, more detail study should be conducted. First of all, O_2 concentration should be well controlled, then morphology, chemical contamination and crystal structure should be studied. SEM, XPS, XRD and TEM will be used.

REFERENCE LIST

1) http://www.ti.com/corp/docs/kilbyctr/kilby.shtml

2) S. P. Murarrka, Mater. *Sci. Eng. R,* **19**, 87 (**1997**).

3) Shacham-Diamand, *J. Electron. Mater*. **30**, 336 (**2001**)

4) International Technology Roadmap for Semiconductor -2002 Update, Semiconductor Industry Association, pp. 74-75; see *http://public.itrs.net/* (**2002**).

5) Ishita Goswami and Ravi Laxman, ATMI, San Jose, *Semiconductor International,* 5, (**2004**).

6) Vandenbroucke, D.A., R.L.V. Meirhaeghe, and F. Cardon, *J. Phys. D: Appl. Phys.,* **18**, 731 (**1985**).

7) R.J. H. Clark, *The Chemistry of Ruthenium*, , New York: Elsevier, p12, **(1984**).

8) H. S. Momose, M. Ono, T. Yoshitomi, T. Ohguro, S. Nakamura, M. Saito, and Hiroshi Iwai, "Tunneling Gate Oxide Approach to Ultra-High Current Drive in Small-Geometry MOSFETs," *IEDM Tech. Digest*, p. 238 (**1994**).

9) Zhong, Huicai *Ru-based Gate electrodes for Advanced Dual-Metal Gate CMOS Devices*, a dissertation to the graduate Faculty of North Carolina State University, (**2001**).

10) T. S. Kalkur and Y. C. Lu, *Thin Solid Films*, **205**, 266 (**1991**).

11) C. G. Parker, " Device Quality Remote Plasma-Enhanced Chemical Vapor Deposited (RPECVD) Gate Dielectrics for MOS Applications", a dissertation submitted to the Graduate Faculty of North Carolina State University, **1998.**

12) B. E. Conway, *Electrochemical Supercapacitor*s, Kluwer-Plenum, New York (**1999**).

13) G. Lucovsky, H. Yang, H. Niimi, J. W. Keister, J. E. Rowe, M. F. Thorpe, and J. C. Phillips, "Intrinsic limitations on device performance and reliability from bond constraint induced transition regions at interfaces if stacked dielectrics", presented at International Conference on Silicon Dielectric Interfaces, Raleigh, NC, Feb, (**2000**).

14) Y.T. Kim, C.W. Lee, and S.K. KwakAppl. *Phys. Lett*. **67** (6), 807 (**1995**).

15) A.S. Arico, G. Monforte, E. Modica, P.L. Antonucci, V. Antonucci, *Electrochemistry Communications,* **2**, 466 (**2000**).

16) J.P. Popic, M.L. Avramov-Ivic, N.B. Vukovic, *Journal of Electroanalytical Chemistry,* **421***,* 105 (**1997**).

17) N. Matsui, K. Anzai, N. Akamatsu, K. Nakagawa, N. Ikenaga, T. Suzuki, *Applied Catalysis A.*, **179**, 247 (**1999**).

18) L. Zang, H. Kirsch, *Angew. Chem. Int. Ed.* **39**, 3921 (**2000**).

19) J.M Walls, Methods of Surface analysis, Printed In Great Britain at the University Press, Cambridge, (**1989**).

20) Jone F. Watts and John Wolstenholme, *An introduction to surface analysis by XPS and AES*. New York: J. Wiley (**2003**).

21) Ebel, M.F., Absolute calibration of an X-Ray photoelectron Spectrometer, *Journal of Electron Spectroscopy and Related Phenomena*, **8**, 213 (**1976**)

22) Vickerman, J. C., Ed. *Surface Analysis - The Principal Techniques*; John Wiley & Sons: New York, (**1997**).

23) Wagner, C. D.; Riggs, W. M.; Davis, L. E.; Moulder, J. F. *Handbook of X-ray Photoelectron Spectroscopy*; Physical Electronics: Eden Prarie, MN, (**1995**).

24) Eric Lifshin, *X-ray Characterization of Materials*, New York (**1999**).

25) Klug, H. P., Alexander, L. E. *X-ray Diffraction Procedures: For Polycrystalline and Amorphous Materials*; Second ed.; Wiler-Interscience: New York, (**1974**).

26) James, R. W. *X-ray Crystallography:* Fifth ed.; Butler and Tanner LTD.: London, (**1962**).

27) Ludwig Reimer, *Transmission Electron Microscopy,* third edition, New York: Springer-Verlag, (**1993**).

28) Andreas Rosenauer, *Transmission electron Microscopy of Semiconductor Nanostructures,* New York: Springer (**2002**).

29) R. Kalvoda and Roger Parsons, *Electrochemistry in Research and Development*, New York, (**1985**).

30) Larry R. Faulkner, Journal of Chemical Education, 60, 4, p262-4 (**1983**).

International Technology Roadmap for Semiconductors, http://public.itrs.net/Reports.htm; SEMATECH Inc., (**2003**).

31) Back to the Future: Copper Comes of Age, *http://domino.research.ibm.com/comm/wwwr_thinkresearch.nsf/pages/copper397.html;* IBM Corporation: New York, (**1997).**

32) A. Jain, K. M. Chi, T. T. Kod M. J. Hampden-Smith, *J. Electrochem. Soc.,* **140**, 1434 (**1993**).

33) Kuzume, Akiyoshi; Herrero, Enrique; Feliu, Juan M.; Nichols, Richard J.; Schiffrin, David J. Centre for Nanoscale Science, Department of Chemistry, the University of Liverpool, Liverpool, UK. *Journal of Electroanalytical Chemistry,* **570** (2), 157 (**2004**) .

34) Simkunaite, Dijana; Ivaskevic, Emilija; Jasulaitiene, Vitalija; Kalinicenko, Aleksandras; Valsiunas, Ignas; Steponavicius, Antanas. Institute of Chemistry, Vilnius, *Lithuania. Chemija* , **15** (1), 12-21 (**2004**).

35) Martinez-Ruiz, Alejandro; Palomar-Pardave, Manuel; Valenzuela-Benavides, J.; Farias, Mario H.; Batina, Nikola. Facultad de Ciencias, Universidad Autonoma de Baja California, Ensenada, Mex. *Journal of Physical Chemistry* B, **107** (42), 11660 (**2003**).

36) Zei, M. S. Fritz-Haber Inst., Max-Planck-Gesellschaft, Berlin, Germany. *Zeitschrift fuer Physikalische Chemie* (Munich), **208** (1/2), 77 (**1999**).

37) S. Trasatti, G. Lodi (Eds*.), Electrodes of ConductiveMetallic Oxides*, Part A and Part B, Elsevier, Amsterdam,(**1980**) and (**1981).**

38) S. Trasatti, in: H. Wendt (Ed.), *Electrochemical Hydrogen Technologies*, Elsevier, Amsterdam, **104**, 1(**1990**).

39) H. Over, *Applied Physics A*, **75**, 37 (**2002**).

40) W.F. Lin, J.M. Jin, P.A. Christensen, K. Scott, *Electrochimica Acta* , **48**, 3815 (**2003**).

41) Rao, C.N.R.; Raveau, B.: "*Transition Metal Oxides Structure, Properties, and Synthesis of Ceramic Oxides*", p 229-254, 2nd ed.; Wiley –VCH: New York.

42) P.C.S. Hayfield, *Plat. Met. Rev*. 42 (1998) 27; 42 (**1998**) 46; 42 (**1998**) 116.

43) L. Krusin-Elbaum, M. Wittmer, *J. Electrochem. Soc.***135**, 2610 (**1988**).

44) T. Maeder, P. Muralt, L. Sagalowicz, M. Setter, *J. Electrochem. Soc.* **146,** 3393 (**1999**).

45) E. Kolawa, F.C.T. So, E.T. Pan, M.A. Nicolet, *Appl.Phys.Lett.* 50, 854 (**1987)**.

46) N.C. Van Huong, M.J. Gonzalez-Tejera, *J. Electroanal. Chem.* **244**, 249 (**1988**).

47) M.A. Quiroz, Y. Meas, *J. Electroanal. Chem.* **157**, 165 (**1983**).

48) P.M.A. Sherwood, *Surf. Sci.*, **101**, 619 (**1980**).

49) K. Christmann, G. Ertl, H. Shimizu, *J. Catal.* **61**, 397 (**1980**).

50) D.M. Kolb, M. Przasnyski, H.. Gerischer, *Electroanal.Chem.and Interfac. Electrochem.* **54**, 25 (**1974**).

51) E.M. Stuve, J.W. Rogers Jr., D. Ingersoll, D.W. Goodman, M.L. Thomas, *Chem. Phys. Letters.* **149**, 557 (**1988**).

52) K.E. Swider, C.I. Merzbacher, P.L. Hagans, D.R. Rolison, *Chem, Mater.* **9**, 1248 (**1997**).

53) D.A. McKeown, P.L. Hagans, L.P.L. Carette, A.E. Russell, K.E. Swider, D.R. Rolison, *J. Phys. Chem. B*, **103**, 4825 (**1999**).

54) G.A. Somorjai, *"Principles of Surface Chemistry"*, Prentice Hall: Englewood Cliffs, NJ, (**1972**).

55) A. J. Hartmann, M. Neilson, M. R. N. Lamb, K. Watanabe, and J. F. Scott, *Appl. Phys. A: Mater. Sci. Process.,* **70**, 239 (**2000**).

56) Zhichao Shi, Shujie Wu and Jack Licek Lipkowski, *Electrocjimica Acta*. **40** (1) 915 (**1995**).

57) D. M Kolb, Z. *Phys. Chem*. **154**, 179 (**1987**).

58) W. Dmowski, T. Egami, K.E. Swider-Lyons, C.T. Love, D.R. Rolison, *J. Phys. Chem. B.* **106**, 12677 (**2002**).

59) Duan-Ming Tan and Kin Shing Chan, *Tetrahedron Letters,* **46**(3), 503 (**2005**).

60) Ricardo Martínez, Gabriel J. Brand, Diego J. Ramón and Miguel Yus *Tetrahedron Letters,* **46** (21), 3683 (**2005**).

61) N.A. Gjostein, *"Diffusion"*; American Society for Metals; Metals Park, Ohio, (**1973**).

62) Singer, P. In *Semiconductor International*, **2004.**

63) Peters, L. In *Semiconductor International*, **2003.**

64) Y. Shacham-Diamand, J. Electron. Mater. **30**, 336 (**2001**).

65) K. M. Takahashi, *J. Electrochem. Sco*., **147**, 1414 (**2000**)

66) T. B. Massalski, *Binary Phase Alloy Diagrams*, 2nd ed., Editor, p. 1467, Materials Information Society, (**1990**).

67) M. W. Lane, C. E. Murray, F. R. McFeely, P. M. Vereechen, and R. Rosenberg. *Appl. Phys. Lett.* **83**, 2330 (**2003**).

68) O. Chyan, T. N. Arunagiri and T. Ponnuswamy, *J. Electrochem. Soc.,* **150**,

C347 (**2003**).

69) R. Chan, T. N. Arunagiri, Y. Zhang, O. Chyan, R. M. Wallace, M. J. Kim, T.Q. Hurd, *Electrochem. Solid-State Lett.,* **7**, G154 (**2004**).

70) Y. Zhang, L. Long, T. N. Arunagiri, O. Ojeda, S. Flores, O. Chyan, R. M. Wallace, *Electrochem. Solid-State Lett.,* **7** (9), C107 (**2004**).

71) D. Josell, D. Wheeler, C. Witt and T. P. Moffat, *Electrochem. Solid-State Lett.,* **6**, C143 (**2003**).

72) Q. Wang, J. G. Ekerdt, D. Gay, Y. M. Sun, J. M. White, *Appl. Phys. Lett.* **84**, 1380 (**2004**).

73) H. Kim, *J. Vac. Sci. Technol*. B, **21** (6), 2231 (**2003).**

74) Arunagiri, T. N.; Zhang, Y.; Chyan, O.; El-Bouanani, M.; Kim, M. J.; Wu, C. T.; Chen, L.-C.; Chen, K.-H. *Appl. Phys. Lett.* **86** (8), 083104-1 (**2005).**

75) Y. Matsui, Y. Nakamura, Y. Shimamoto, M. Hiratani, *Thin Solid Films*, **437**, 51 (**2003**).

76) E.V. Jelenkovic, K.Y. Tong, W.Y. Cheung, S. P. Wong, *Semicond. Sci. Technol*. **18**, 454 (**2003**).

77) S. J. Morgan, R. H. Williams, J. M. Mooney, *Appl. Surf. Sci.*, **56-58**, 493 (**1992**).

78) David R. and H. P. R. Frederikse, CRC Handbook of Chemistry and Physics, CRC press, 77th Ed. New York, (**1996**).

79) J.S. Kwak, H.K. Baik, J.H. Kim, S.M. Lee, *Appl. Phys. Lett.,* **71**, 2451 (**1997**).

80) Qu, X. P.; Lu, H.; Peng, T.; Ru, G. P.; Li, B. Z. *Thin Solid Films*, **462-463**, 67 (**2004**).

81) Sarkar, D. K.; Bera, S.; Narasimhan, S. V.; Chowdhury, S.; Gupta, A.; Nair, K. G. M. *Solid State Comm.,* **107**, 413 (**1998**).

82) Shin, D. W.; Wang, S. X.; Marshall, A. F.; Kimura, W.; Dong, C.; Augustsson, A.; Guo, *J. Thin Solid Films*, **473**, 267 (**2005**).

83) Cros, A.; Aboelfotoh, M. O.; Tu, K. N. *J. Appl. Phys.*, **67**, 3328 (**1990**).

84) C. A. N, Fernando, P. H. C. de Sila, S. K. Wethasinha, L. M. Dharmadasa, T. Delsol, M. C. Simmonds, *Renewable Energy* **26**, 512 (**2002**).

85) N. S. Mclntyre and M. G. Cook, *Analytical chemistry*, **47** (13), 2008 (**1975**).

86) Llopis, J. F.; Tordesillas, I. M. In *Encyclopedia of Electrochemistry of the Elements*; Bard, A. J., Ed.; Marcel Dekker Inc.: New York, Vol. VI, pp 278-295 (**1976**).

87) N. A. Gjostein, *Diffusio*n, *American Society for Metals*, Metals Park, OH (**1973**).

88) M.-A. Nicolet, *Thin Solid Films,* **52**, 415 (**1978**)

89) E. Kolawa, F. C. T. So, E. T.-S. Pan, and M.-A. Nicolet, *Appl. Phys. Lett.,* **50**, 854 (**1987**).

90) International Technology Roadmap for Semiconductor, Semiconductor Industry Association, see http://public.itrs.net/. (**2001**).

91) M. Ritala and M. Leskela, *Nanotechnology* **10**,19 (**1999**).

92) M. Leskela¨ and M. Ritala, *Thin Solid Films,* **409**, 138 (**2002**).

93) M. W. Lane, C. E. Murray, F. R. McFeely, P. M. Vereecken, and R. Rosenbaum, *Appl. Phys. Lett*. **83**, 2330 (**2003**).

94) Jay A. Switzer, Chen-jen Huang, Ling-yuang Huang, Eric R. Switzer, Daniel R. Kammler, Teresa D. Golden and Eric. W. Bohannan. *J. Am. Chem. Soc*. **120**, 3530 (**1998**).

95) Ling-yuang Huang, Eric. W. Bohannan, Chen-jen Huang, and Jay A. Switzer. *Israel Journal of Chemistry*, **37**, 293 (**1997**)

96) Run Liu. Fumiyasu Oba, Eric. W. Bohannan, Frank Ernst and Jay A. Switzer. *Chem. Mater*, **15**, 4882 (**2003**).

97) Run Liu, Eric. W. Bohannan and Jay A. Switzer. *Applied Physics Letters*. **83** (10), 1944 (**2003**).

98) Jay A. Switzer, Hiten M. Kothari and Eric. W. Bohannan. *J. Phys. Chem. B.* **106** (16) 4027 (**2002**).

99) S. Leopold, I. U. Schuchert, J. Lu, M. E. Toimil Molares, M. Herranen and J. –

100) O. Carlsson, *Electrochimica Acta,* **47** (27), 4393 (**2002**).

101) D. K. Zhang, Y. C. Liu, Y. L. Liu and H. Yang, *Physica B: Condensed Matter,* **351** (1-2), *178* (**2004**).

102) You-Lin Wu, Yi-Cheng Hwang, *Thin Solid Film,* **461**, 294 (**2004**).

103) W.C. Gau, T.C. Chang, Y.S. Lin, L.c. Hu, L. J. Chen, C.Y. Chang, C.L.Cheng *J. Vac. Sci. Technol. A,* **18** (2) (**2000**).

104) S. Hartinger and K. Doblhofer, *Journal of electoanalytical Chamistry*, **380**,185 (**1995**).

105) M. H. Holzle, C. W. Apsel, T. Will and D. M. Kolb, *Electrochem. Soc.* Vol. **142** (11), 3741 (**1995**).

106) Saurbrey, G.Z., Z. *Phys*, **155**, 206 (**1959**).

107) Hepel, M., *Electrode-Solution Interface Studied with Electrochemical Quartz Crystal Nanobalance*, in *Interfacial Electrochemistry: Theory, Experiment and Application.*, A. Wieckowski, Editor. Marcel Dekker: Postdam. p. 599-629 (**1999**).

108) Lu, C., *Applications of Piezoelectric Quartz Crystal Microbalances*, in *Methods and Phenomena: Their application in Science and Technology.*, C. Lu; and A.W. Czanderna, Editors. Elsevier Science: Amsterdam. p. 393 (**1984**).

109) *http://webmineral.com/data/psnjakite*

110) Aeyoung Lee and Yonggsug Tak*, Electrochemical and Solid- State letter*, **2** (11) 559 (**1999**).

111) Masamitsu Watanabe, Masato Tomita and Toshino, *J. Electrchem. Soc.,* **148** (12) B522 (**2001**).

112) K. P Pitzgerald, J. Nairn and A. Atrens, *Corrosion Science*, **40** (12) 2029 (**1998**).

113) A.I. Danilov , E.B. Molodkina , Yu.M. Polukarov , V. Climent ,J.M. Feliu *Electrochimica Acta,* **46**, 3137 (**2001**).

114) CD Wagner, *Handbook of X-ray photoelectron spectroscopy*, Perkin Elmer Corporation, Eden Prairie.

115) Wolfgong Kautek and Joseph G. Gordon 11, *J. Electrochem. Soc*. Vol. **137** (9), 2672 (**1990**).

116) N. S. Mclntyre and M. G. Cook, *Analytical chemistry*, **47** (13), 2008 (**1975**).

117) C. A. N, Fernando, P. H. C. de Sila, S. K. Wethasinha, L. M. Dharmadasa, T. Delsol, M. C. Simmonds, *Renewable Energy,* **26**, 512 (**2002**).

118) Kavita Borgohain, Norio Murase, Shailaja Mahamunia) *J. Appl. Phys.,* **92** (3) (**2002**).

119) Haixia Dai,Corrine K. Thai,Mehmet Sarikaya, Franc¸ois Baneyx,and Daniel T. Schwartz, *Langmuir,* **20** (8), (**2004**).

120) Zhongyuan Dang, Jingfang Gu and Ling Yu, *Applied Catalysis*. **63**, 256 (**1990**).

121) F. King, M.J. Quinn, C.D. Like, *Journal of electroanalytical Chemistry* **385**, 45 (**1995**).

122) A. C. Cascalheira and L.M. Abrantes, *Electroimica Acta* , **49**, 5023 (**2004**).

123) Myungchan Kang and Andrew A. Gewirth, *J. Phys. Chem*., B, **106**, 12211- (**2002**).

124) F. Noil, P. Misaelides, A. Hatzdimitriou, E. Pavlidou and M. Kokkorris, *J. Mater. Chem.* **13**, 114 (**2003**).

125) J.O. Park, C.H. Paid, Y.H. Huang, and R.C. Alkire, *Journal of the electrochemiscal society,* **146** (2), 517 (**1999**).

126) J. O. Zerbino, M.F.L. DE. Mele, *Journal of Applied electrochemistry*, **27**, 335 (**1997**).

127) Jay A. Switzer, Chen-jen Huang, Ling-yuang Huang, F. Scott Miller, Yanchun Zhou, Eric R. Raub, Mark G. Shumsky and Eric. W. Bohannan. *J. Mater. Res*, **13** (4), 911 (**1998**).

128) Y.C Zhou and Jay A. Switzer *Mat. Res. Innovat*, **2**, 22 (**1998**).

129) Antonio R. Mendoza, Francisco Corvo, Ariel Gomez and Jorge Gomez, *Corrosion Science,* **46**, 1189 (**2004**).

130) A.G. Christy, A. Lowe, V. Otieno, V. Otieno-Alego, M. Stoll and R.D. Webster. *Journal of Applied Electrochemistry,* **34**, 225 (**2004**).

131) L. Veleva. P. Quintana, R. Ramanaluskas, R. Pomes and Maldonado, *Electrimica, Acta*, **41** (10) 1641 (**1996**).

132) Pollard, A. M. and Thomas, R.G. *Mineralogical Magazine,* **56**, 359 (**1992**).

133) Malvault, J. Y and Lopitaux, *Journal of Applied Electrochemistry,* **25**, 841 (**1995**).

134) R. Schlesinger, H. Klewe-Nebenius and M. Bruns *Surface and Interface Analysis,* **30***,* 135 (**2000**).

135) Gabriela P. CiCileo, Miguel A. Grepo, Blanca M. Rosales, *Corrosion Science,* **46**, 929 (**2004**).

136) S. Jouen, M. Jean, B. Hannoyer, Surf. *Interface Anal*. **30**, 145 (**2000**).

137) Mekhalif, F. Sinapi, F. Laffineur, J. Delhalle, *Journal of electron*

spectroscopy and related phenomenon, **121**, 149 (**2001**).

138) J. B. Matos, L. P. Pereira, S.M.L Agostinho, O.E. Barcia, G.G.O Cordeiro, E. D'Elia, *Journal of Electroanalytical Chemistry*, **570** (1), 91 (**2004**).